The Development and Performance of the First BICEP Array Receiver at 30/40 GHz for Measuring the Polarized Synchrotron Foreground

Thesis by
Cheng Zhang (张程)

In Partial Fulfillment of the Requirements for the
Degree of
Doctor of Philosophy

CALIFORNIA INSTITUTE OF TECHNOLOGY
Pasadena, California

2023
Defended June 10th 2022

Cheng Zhang (张程)
ORCID: 0000-0001-8288-5823

ACKNOWLEDGEMENTS

I want to first thank my advisor Jamie Bock, who himself is a respected physicist and astronomer, for his patience, support, and inspiring leadership, which led me into the wonderland of cosmology and helped me through my graduate school.

I also want to thank Bryan Steinbach, who has been a great mentor to me for providing the just-right-amount of instructions and encouraging me to grow into an independent researcher. I'm grateful to have Brandon Hensley, Lorenzo Moncelsi, Alessandro Schillaci, Roger O'Brient, Howard Hui, Ritoban Basu Thakur, Sinan Kefeli, Jon Hunacek, Ahmed Soliman, Silvia Zhang, Hien Nguyen, Albert Wandui, Lorenzo Minutolo and the rest of ObsCos group to work with and learn from through the years. Without any of you my six years life at Caltech will not be as enjoyable or rewarding.

I feel lucky to be a member of the BICEP/*Keck* Collaboration which has so many outstanding scientists and extraordinary, motivated students. My memories of the annually collaboration meetings and deployments with you people are the best part of my graduate school. Special thanks to our PIs, Jamie Bock, John Kovac, Clem Pryke, and Chao-Lin Kuo, whose leadership keeps the project running.

Being far from home, my life in the past few years were brightened by my friends. It's hard to list out all the names, but I do want to convey my special thanks to Zhichao Shen (沈智超), Zhe Jia (贾哲), and Jingyi Fang (方静一) for being like my family in LA. I also want to shout out to the Science Sauna Group at the South Pole. Pole is a magic place where a few months can feel like a life time. I'm thankful for meeting all the open-minded free spirits there. Thank you Aman Chokshi for providing me all those awesome pole photos to put into my talks and impress people.

I want to thank my husband Ziwei Li (李子维) for the unconditional support and love and for giving me the freedom and courage to explore my potentials. Thank you for being my family and the best friend I could ever ask for.

Finally, thank you to my parents Bing Cheng (程冰) and Haitao Zhang (张海涛), and my grand parents Ruochun Wang (王若春) and Yujun Cheng (程煜均). Miss you all.

ABSTRACT

The existence of the CMB marks a big success of the lambda cold dark matter (ΛCDM) standard model, which describes the universe's evolution with six free parameters. The inflationary theory was added to the picture in the '80s to explain the initial conditions of the universe. Scalar perturbations from inflation seeded the formation of the large-scale structure and produced the curl-free E-mode polarization pattern in the CMB. On the other hand, tensor fluctuations sourced primordial gravitational waves (PGW), which could leave unique imprints in the CMB polarization: the gradient-free B-mode pattern. The amplitude of B modes is directly related to the tensor-to-scalar ratio r of the primordial fluctuations, which indicates the energy scale of inflation. The detection of the primordial B modes will be strong supporting evidence of inflation and give us opportunities to study physics at energy scales far beyond what can ever be accessed in laboratory experiments on the Earth.

Currently, the main challenge for the B-mode experiments is to separate the primordial B modes from those sourced by matter between us and the last scattering surface: the galactic foregrounds and the gravitational lensing effect. The two most important foregrounds are thermal dust and synchrotron, which have very different spectral properties from the CMB. Thus the key to foreground cleaning is the high sensitivity data at multiple frequency bands and the accurate modeling of the foregrounds in data analyses and simulations. In this dissertation, I present my work on ISM and dust property studies which enriched our understanding of the foregrounds.

The BICEP/*Keck* (BK) experiments build a series of polarization-sensitive microwave telescopes targeting degree-scale B-modes from the early universe. The latest publication from the collaboration with data taken through 2018 reported tensor-to-scalar ratio $r_{0.05} < 0.036$ at 95% C.L., providing the tightest constraint on the primordial tensor mode.

BICEP Array is the latest generation of the series experiments. The final configuration of the BICEP Array has four BICEP3-class receivers spanning six frequency bands, aiming to achieve $\sigma(r) \lesssim 0.003$. The first receiver of the BICEP Array is at 30 and 40 GHz, constraining the synchrotron foregrounds. In this dissertation, I cover the development of this new receiver focusing on the design and performance of the detectors. I report on the characterizing and diagnosing tests for the receiver during its first few observing seasons.

PUBLISHED CONTENT AND CONTRIBUTIONS

Hensley, Brandon S., Cheng Zhang, and James J. Bock (2019). "An Imprint of the Galactic Magnetic Field in the Diffuse Unpolarized Dust Emission". In: *The Astrophysical Journal* 887.2, p. 159. DOI: 10.3847/1538-4357/ab5183.

C.Z. collaborated with Brandon Hensley on ISM galactic dust emission modelling and analysis. She made all the plots in the paper and participated in part of the manuscript writing.

TABLE OF CONTENTS

LIST OF ILLUSTRATIONS

LIST OF TABLES

Chapter 1

COSMOLOGICAL MOTIVATION

1.1 The Standard Model of Cosmology

The cosmological principle assumes a homogeneous and isotropic universe at the very large spatial scale. In describing the geometry of the universe, it leads to the Friedmann-Lemaître-Robertson-Walker (FLRW) metric

$$\mathrm{d}s^2 = -c^2\mathrm{d}t^2 + a(t)^2\left(\frac{\mathrm{d}r^2}{1-kr^2} + r^2\mathrm{d}\theta^2 + r^2 sin^2\theta\mathrm{d}\phi^2\right) , \tag{1.1}$$

assuming that the spatial components of the metric are time-dependent. The time dependency is represented by the scale factor $a(t)$ whose present value is set to 1. k takes values of 0, 1, or -1, corresponding to a flat, close, or open universe. These are the only three cases in which the universe can have a universal curvature radius.

With the general form of the global metric in Eq. 1.1, assuming a homogeneous and isotropic stress-energy tensor, we get the Friedmann equations from the Einstein's field equations of general relativity

$$H^2 \equiv \left(\frac{\dot{a}}{a}\right)^2 = \frac{8\pi G}{3}\rho - \frac{k}{a^2} + \frac{\Lambda}{3} , \tag{1.2}$$

$$\frac{\ddot{a}}{a} = \frac{\Lambda}{3} - \frac{4\pi G}{3}(\rho + 3p) . \tag{1.3}$$

The $H \equiv \dot{a}/a$ represents the time-dependent expansion rate, whose current value H_0 is the Hubble constant. G is the Newtonian gravitational constant, ρ is the energy density, and Λ is the cosmological constant. Eq. 1.2 and 1.3 determine the evolution of the scale factor $a(t)$. But to get the solution, we need knowledge of the energy density.

In the ΛCDM (Lambda cold dark matter) standard model, the universe contains three major components: matter, radiation, and dark energy. In an expanding universe, the energy density of each kind of component evolves following the rule set by its equation of state (EOS)

$$p = w\rho \ , \tag{1.4}$$

which leads to

$$\rho \propto a^{-3(w+1)} \ . \tag{1.5}$$

The dark energy, or the cosmological constant Λ, has $w = -1$ and a constant energy density. For both baryon and dark matter, $w = 0$, and the energy density is proportional to the number density, $\rho_M \propto a^{-3}$. Radiation and other relativistic particles like neutrino have $w = 1/3$ and $\rho_r \propto a^{-4}$. The energy density of radiation reduces faster during the cosmic expansion because the wavelength gets stretched.

The evolution of the comoving Hubble radius during a period when the universe was dominated by a specific component is

$$(aH)^{-1} = H_0^{-1} a^{-\frac{1}{2}(1+3w)} \propto \begin{cases} a & \text{radiation-dominated} \\ a^{1/2} & \text{matter-dominated} \\ a^{-1} & \text{cosmological constant-dominated} \end{cases} \tag{1.6}$$

The early universe was dominated by radiation before $z_{eq} = 3600$. After that, the universe was matter-dominated until recent around $z = 0.4$, when the dark energy started taking over.

In Eq. 1.2, by setting $\Lambda = 0$, we can solve for the critical density which gives a flat universe ($k = 0$)

$$\rho_{crit} = \frac{3H^2}{8\pi G} \ . \tag{1.7}$$

The density parameter of each component is defined as

$$\Omega_i \equiv \rho_i / \rho_{crit} \ . \tag{1.8}$$

The first Friedmann equation can be rewritten with the present density parameters

$$H^2 = H_0^2 \left(\Omega_{0,r} a^4 + \Omega_{0,M} a^3 + \Omega_{0,k} a^2 + \Omega_{0,\Lambda} \right) \ , \tag{1.9}$$

where the subscript 0 means the present value, Ω_k is the fictitious curvature density parameter, $\Omega_{0,k} = 1 - (\Omega_{0,r} + \Omega_{0,M} + \Omega_{0,\Lambda})$. If the total energy density is equal to the critical density, $\Omega_k = 0$, $k = 0$, the universe is flat. An over-dense universe is closed, with $\Omega_k < 0$, $k = 1$. An under-dense universe is open, with $\Omega_k > 0$, $k = -1$.

In the case of all three geometries, though the universe will end in different ways, it will always have an expanding era. The observation done by Edwin Hubble in 1929 (Hubble, 1929) showed that our universe is expanding. A hot and dense early universe was then concluded by pushing the time backward from now to the past. In the more popular term, the universe started with a Big Bang. Many observations to date strongly endorsed the Big Band theory and the ΛCDM model, including the discovery of the Cosmic Microwave Background (CMB) and its anisotropies.

1.2 The Cosmic Microwave Background

In an expanding universe, the number density of particles goes as

$$n \propto a^{-3} \, . \tag{1.10}$$

The photon's wavelength gets stretched following the rule $\lambda \propto a$ or in frequency $\nu \propto a^{-1}$. By definition, the relationship between the scale factor and redshift is $a^{-1} = 1 + z$. The radiation temperature scales as

$$T = T_0 a^{-1} = T_0(1 + z) \, , \tag{1.11}$$

where $T_0 = 2.72548 \pm 0.00057$K (Fixsen, 2009) is the current temperature of the universe.

Eq.1.10 and 1.11 show that in the early time, when a was small, and z was large, the universe was hot and dense, and it was cooling down during the expansion. During the first few hundred thousand years, the energy of the radiation was too high for any neutral hydrogen to form.

Three main processes dominated the interaction between particles in the early universe plasma: Compton scattering, double Compton scattering, and Bremsstrahlung. Before the decoupling of photons, the scattering rates of all three processes were higher than the expanding rate, and the particles were in equilibrium.

The reaction $e + p \leftrightarrow \mathrm{H} + \gamma$ can be described by the Saha equation before dropping to far from equilibrium . The free electron fraction $X_\mathrm{e} \equiv \frac{n_e}{n_e+n_\mathrm{H}} = \frac{n_p}{n_p+n_\mathrm{H}}$ can be calculated by

$$\frac{X_e^2}{1-X_e} = \frac{1}{n_e + n_\mathrm{H}} \left[\left(\frac{m_e T}{2\pi} \right)^{3/2} e^{-\epsilon_0/T} \right] , \tag{1.12}$$

where ϵ_0 is the ionization energy of hydrogen, 13.6 eV. This result approximates the accurate solution of the Boltzmann equation quite nicely, see Figure 3.4 in (Dodelson, 2003b). Eq.1.12 shows that the universe remained highly ionized (X_e close to 1) until T dropped far below ϵ_0. Recombination occurred at T around 0.3 eV or 3000 K, z around 1100, which was approximately 300,000 years after the Big Bang.

During recombination, X_e dropped quickly from close to 1 to 10^{-3}. The Thompson scattering rate $n_e \sigma_T$ also decreased as fewer free electrons were in the universe. Photon decoupled when the scattering rate fell below the Hubble rate H. This happened during the recombination. The decoupled photons then free streamed through the spacetime and reach us today, providing a snapshot of the early universe. Their wavelength got stretched into the microwave band by the cosmic expansion, thus called the Cosmic Microwave Background (CMB).

The CMB was first measured by Arno A. Penzias and Robert W. Wilson in 1965 as isotropic radiation at 3.5 K (Penzias and Wilson, 1965). The frequency spectrum measured by COBE FIRAS instrument agreed with a blackbody spectrum to high accuracy as shown in Figure 1.1 (Mather et al., 1994), with a temperature $T_0 = 2.72548 \pm 0.00057$K (Fixsen, 2009). These observations strongly support the Big Bang theory as no alternate theory can predict such an equilibrium background radiation.

In 1960-70s, inhomogeneities required by large scale structure formation were discussed (Harrison, 1970) (Peebles and Yu, 1970) (Zeldovich, 1972). Anisotropies were predicted in CMB at a level $\Delta T/T = 10^{-5}$ (Sunyaev, 1978) and first observed by the COBE satellite (Smoot et al., 1992). The measurements of the angular power spectrum of the CMB anisotropies in the following decades enabled precise cosmology and played a critical role in establishing the ΛCMD standard model and the study of inflation.

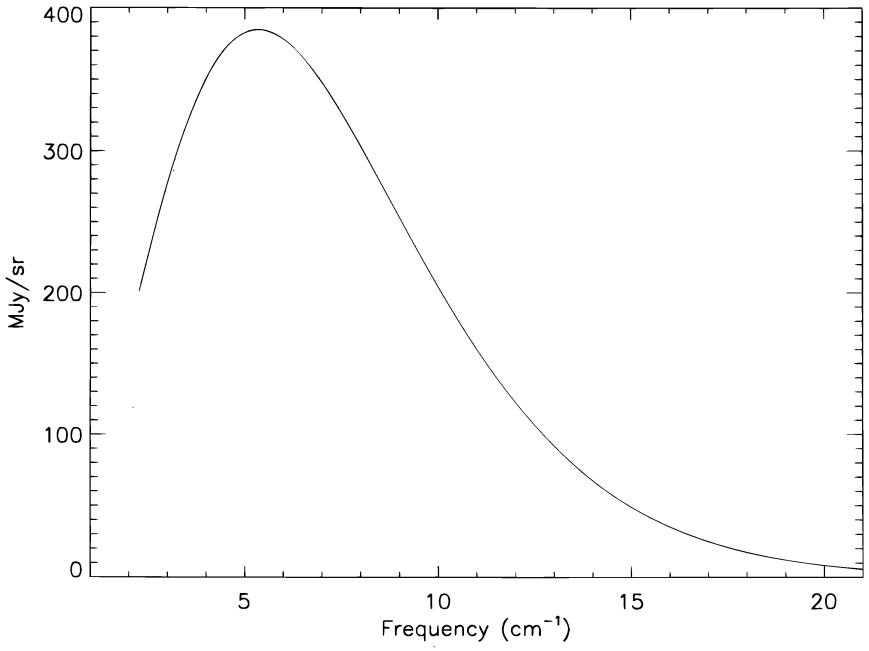

Figure 1.1: Uniform spectrum measured by FIRAS and fit to Planck blackbody. Uncertainties are a small fraction of the line thickness. (Fixsen et al., 1996)

1.3 Inflation

The inflationary theory describes that the universe expanded exponentially during a fraction of the first second right after the Big Bang. It was first proposed by Alan Guth in his investigation of the lack of magnetic monopoles in the universe. He found that a false vacuum with positive energy can cause the space to expand exponentially. This exponential expansion can provide explanations for some long-standing cosmic problems.

Magnetic-Monopole Problem

The Grand United Theories predict that magnetic monopoles can be produced at high temperatures. The particle is stable and heavy. They should have persisted to the present day and become the primary constituent of the universe. However, this contradicts the null results of all the experimental search efforts to date. The inflation that happened after the production of magnetic monopoles could have dramatically reduced its density, making it very hard to be detected in laboratory experiments.

Horizon Problem

The maximum distance light can travel between time 0 and t is

$$\tau \equiv \int_0^t \frac{\mathrm{d}t'}{a(t')} = \int_0^a \frac{\mathrm{d}a'}{Ha'^2} = \int_0^a \frac{\mathrm{dln}a'}{Ha'} \,. \tag{1.13}$$

τ is the particle horizon at time t, which sets the boundary of a causally connected region. Because the particle horizon can be calculated as an integral of the comoving Hubble radius, its dependency on the scale factor is similar to Eq. 1.6 if we consider the universe to be dominated by a single component.

$$\tau \propto \begin{cases} a & \text{radiation-dominated} \\ a^{1/2} & \text{matter-dominated} \\ a^{-1} & \text{cosmological constant-dominated} \end{cases} \tag{1.14}$$

Before the fairly recent dark energy era, the particle horizon was growing as the universe was expanding, which means its size in the early universe, e.g., at recombination, was much smaller than today. The regions of the universe that were causally connected at the last scattering are only about 2 deg angular scale on today's CMB sky. Sky patches separated by an angle larger than this were outside each other's horizon. No known physics could interact between them.

However, the observable universe appears to be highly uniform. The measured temperature of CMB is almost the same in all directions, with very small anisotropies at 1/100,000 level, which suggests that the early universe was in equilibrium. The standard Big Bang model does not explain the homogeneity except simply assumes that the whole universe was set to the same temperature from the beginning. We sometimes refer to the beyond-horizon equilibrium as the horizon problem.

One plausible solution to the horizon problem is letting the Hubble radius be large at the beginning and shrink later. A large Hubble radius in the early universe can contribute to the integral in Eq. 1.14 and result in a large enough particle horizon at recombination.

The shrinking Hubble radius is described by

$$\frac{\mathrm{d}(aH)^{-1}}{\mathrm{d}t} < 0 \,, \tag{1.15}$$

which is equivalent to $\ddot{a} > 0$, an accelerated expansion. The tremendous expansion during inflation indicates that the physical size of the universe was much smaller than expected by the standard model at the beginning of inflation. Thus the thermal

equilibrium could be established between different parts of the universe before they were pushed out of each other's horizons.

With the second Friedmann Equation 1.3, an accelerating expansion requires a negative pressure

$$p < -\frac{1}{3}\rho \ . \tag{1.16}$$

Flatness Problem

Eq. 1.2 can be written with the density parameter as

$$1 - \Omega = -\frac{k}{(aH)^2} \ . \tag{1.17}$$

Since the comoving Hubble radius has been increasing in the standard model, if Ω were not 1 in the early universe, the deviation would have grown rapidly with time. An $\Omega \sim 1$ today requires the value in the early universe to be fine-tuned. For example, the flatness required at the Big Bang Nucleosynthesis has to be

$$|1 - \Omega(a_{\mathrm{BBN}})| \leq O(10^{-16}) \ . \tag{1.18}$$

Like in the horizon problem, a shrinking Hubble radius can resolve the "fine-tune" problem. In Eq. 1.17, during an accelerated expansion, $1/(aH)$ decreases, and $|1 - \Omega|$ is dragged toward zero.

The flatness measured by Planck plus BAO is $\Omega_k = 0.0007 \pm 0.0037$ (Akrami et al., 2020), which matches the prediction of the inflation.

Primordial Perturbations

The quantum fluctuations in the inflation field are stretched during the exponential expansion and become seeds of the formation of large-scale structures later. In the simplest case, a single scalar field ϕ can fulfill the negative pressure requirement and drive the inflation. Since the fluctuations are very small compared to the homogeneous background, we can use linear approximation

$$\phi(t, \mathbf{x}) = \bar{\phi}(t) + \delta\phi(t, \mathbf{x}) \ . \tag{1.19}$$

Perturbations in the metric tensor

$$g_{\mu\nu}(t, \mathbf{x}) = \bar{g}_{\mu\nu}(t) + \delta g_{\mu\nu}(t, \mathbf{x}) \ . \tag{1.20}$$

Metric perturbations can be decomposed into three components: Scalar, Vector, and Tensor perturbations. We can write the scalar perturbations as

$$g_{00} = -(1 + 2\Psi) \ , \tag{1.21}$$

$$g_{0i} = 0 \ , \tag{1.22}$$

$$g_{ij} = a^2 \delta_{ij}(1 + 2\Phi) \ . \tag{1.23}$$

Tensor perturbations have two polarizations, $h = h_+ = h_\times$.

$$g_{ij} = a^2 \begin{pmatrix} 1 + h_+ & h_\times & 0 \\ h_\times & 1 - h_+ & 0 \\ 0 & 0 & 1 \end{pmatrix} . \tag{1.24}$$

Inflation does not create vector perturbations. Even if it does, the vector components will soon decay with the universe's expansion.

The linear approximation allows all the modes to evolve independently in Fourier space. Because of the isotropy, we can label the modes with their wave number's amplitude $k = |\mathbf{k}|$. The comoving wavelength is unchanged during the inflation, but the comoving Hubble radius shrinks. We say a mode exits horizon when

$$k < aH \ . \tag{1.25}$$

While it is outside the horizon, the mode stops evolving and remains frozen. After the inflation, the comoving Hubble radius slowly grows back up. The modes will eventually re-enter the horizon and start to evolve again. As the modes with the same wavelength enter the horizon simultaneously, they are naturally aligned in phase. The coherence of the perturbation modes is a key prediction of inflation, which beautifully explains the peak-and-trough patterns in the CMB power spectrum (Dodelson, 2003a).

The perturbations can be described by a probability distribution with variance given by the power spectrum evaluated at the horizon crossing.

$$P_s(k) = \frac{H^2}{2k^3}\frac{H^2}{\dot{\phi}^2}\bigg|_{k=aH} , \tag{1.26}$$

$$P_t(k) \equiv 2P_h(k) = \frac{4}{k^3}\frac{H^2}{M_{pl}^2}\bigg|_{k=aH} . \tag{1.27}$$

We can define Δ_s^2, Δ_t^2 with

$$\Delta^2 \equiv \frac{k^2}{2\pi^2}P(k) . \tag{1.28}$$

Δ^2s are close to scale-invariant. The slight scale-dependency comes from the time-dependency of H, especially when it is close to the end of the inflation. The scale index of the scalar perturbations is defined as

$$n_s - 1 \equiv \frac{\mathrm{d}\ln\Delta_s^2}{\mathrm{d}k} . \tag{1.29}$$

$n_s = 1$ means perfect scale invariance. Planck CMB temperature and polarization auto/cross spectra measured $n_s = 0.9649 \pm 0.0042$ (95% CL) (Akrami et al., 2020).

The definition of the tensor scale index is

$$n_t \equiv \frac{\mathrm{d}\ln\Delta_t^2}{\mathrm{d}k} . \tag{1.30}$$

The primordial perturbations are usually parameterized with the tensor-to-scalar ratio r, which is proportional to the energy scale of the inflation field

$$r \equiv \frac{\Delta_t^2}{\Delta_s^2} \propto V . \tag{1.31}$$

The simplest inflation model assuming a single slow-rolling scalar inflation field predicts that the primordial perturbations are gaussian and adiabatic. If the perturbations are gaussian, the power spectrum includes all the statistical information. There is not yet detection of non-gaussianity, and the CMB measurements to date suggest the perturbation to be highly adiabatic. However, the slow-roll model is not necessarily the case of how inflation happens. As discussed below, the observations of the CMB polarization anisotropies have ruled out this simplest model at a high confidence level (P. A. R. Ade, Z. Ahmed, Amiri, et al., 2021).

1.4 The Temperature Anisotropies of the Cosmic Microwave Background

As discussed in Chapter 1.2, the recombination happened rapidly enough that CMB photons originated from a sharply defined surface called the last scattering surface. The properties of the early universe plasma are encoded into the CMB photons through the Thomson scattering at the last scattering. The anisotropies in the CMB temperature can be written as

$$\Theta(\hat{n}) \equiv \frac{\Delta T(\hat{n})}{T_0} = \sum_{lm} a_{lm} Y_{lm}(\hat{n}) \ , \tag{1.32}$$

$$a_{lm} = \int \mathrm{d}\Omega Y^*_{lm}(\hat{n})\Theta(\hat{n}) \ . \tag{1.33}$$

Considering the isotropic nature of the universe, the angular power spectrum is

$$C_l^{TT} = \frac{1}{2l+1} \sum_m \langle a^*_{lm} a_{lm} \rangle \ . \tag{1.34}$$

The angular power spectrum is related to the initial condition through

$$C_l^{TT} = \frac{2}{\pi} \int k^2 \mathrm{d}k P_s(k) \Delta_{T,l}(k) \Delta_{T,l}(k) \ . \tag{1.35}$$

$\Delta_{T,l}(k)$ is the temperature transfer function that accounts for the evolution of a mode from horizon re-entry to the recombination and the geometric projection to the CMB sphere.

The density perturbations evolve in acoustic oscillations after the horizon re-entry. The gravity of overdensities compresses the plasma fluid while the radiation pressure provides the repulsive force. For more details, see (Hu and Dodelson, 2002). The oscillation happens faster for the modes with shorter wavelengths or larger k. The phases of the modes at the recombination are modulated by their wavelengths. The modes that happen to reach maximum when the photons are released give rise to the peaks in the CMB angular power spectrum, while those just reach their minimum account for the troughs.

The locations and amplitudes of the peaks in the CMB angular power spectrum shown in Figure 1.4. contain a great amount of cosmic information. The existence of the peaks confirmed that the perturbations are coherent, just as expected by the

inflationary theory. Otherwise, the random phases of modes at the same scale will cancel out.

At very large scales, the perturbation modes have not entered the horizon at the time of recombination. The power spectrum in those modes is

$$l(l+1)C_l^{TT} \propto l^{n_s-1} \ . \tag{1.36}$$

Define

$$D_l \equiv \frac{l(l+1)}{2\pi} C_l \ , \tag{1.37}$$

D_l^{TT} is scale-independent at superhorizon scales if $n_s = 1$ except for a rise at very low l due to the integrated Sachs-Wolfe effect arising from the late-time evolution of the gravitational potential in dark energy dominated universe. That is why the angular power spectrum is usually plotted for D_l.

Cosmic Variance

Eq. 1.34 defines the angular power spectrum. In the real world, we only have one observable universe. The power spectrum can be estimated with the observables a_{lm}

$$\hat{C}_l = \frac{1}{2l+1} \sum_m a_{lm}^* a_{lm} \ . \tag{1.38}$$

There is a natural uncertainty in this estimation which scales as the inverse of the square root of the number of possible samples

$$\frac{\Delta C_l}{C_l} = \sqrt{\frac{2}{2l+1}} \ . \tag{1.39}$$

The cosmic variance limits the constraining power of the temperature anisotropies on inflation, as the relevant information is mainly encoded at large scales (small l).

1.5 The Polarization Anisotropies of the Cosmic Microwave Background

Thomson scattering can generate polarization in CMB at the last scattering surface if the incoming radiation field has quadrupole components. The polarization anisotropies can be written as

$$(Q + iU)(\hat{n}) = \sum_{lm} a_{\pm 2,lm\,\pm 2}Y_{lm}(\hat{n}) \ . \tag{1.40}$$

${}_{\pm 2}Y_{lm}$ are spin-2 or tensor-spherical harmonics. The spin-2 Q and U are equivalent to the spin-0 or scalar fields E and B

$$a_{E,lm} \equiv -\frac{1}{2}(a_{2,lm} + a_{-2,lm}) \ , \tag{1.41}$$

$$a_{B,lm} \equiv -\frac{1}{2i}(a_{2,lm} - a_{-2,lm}) \ . \tag{1.42}$$

Thus

$$E(\hat{n}) = \sum_{lm} a_{E,lm}Y_{lm}(\hat{n}) \ , \tag{1.43}$$

$$B(\hat{n}) = \sum_{lm} a_{B,lm}Y_{lm}(\hat{n}) \ . \tag{1.44}$$

In the Fourier space, with the flat-sky approximation,

$$\begin{pmatrix} \tilde{E}(l) \\ \tilde{B}(l) \end{pmatrix} = \frac{1}{\sqrt{2}} \begin{pmatrix} \cos 2\varphi_l & \sin 2\varphi_l \\ -\sin 2\varphi_l & \cos 2\varphi_l \end{pmatrix} \begin{pmatrix} \tilde{Q}(l) \\ \tilde{U}(l) \end{pmatrix} \ . \tag{1.45}$$

The full-sky solution is more complicated and can be found in (Kamionkowski and Kovetz, 2016).

Consider a plane wave traveling along direction $\mathbf{z}$. E-mode polarization vectors are either perpendicular to or parallel with the direction of propagation $\mathbf{z}$, while B-mode vectors have a 45° angle against $\mathbf{z}$. See Figure 1.2a and 1.2b. E and B maps are coadded plane waves of all different wavelengths and directions. The resulted E map has polarization vectors radial around cold spots and tangential around hot spots. Thus E-mode is described as curl-free. E-modes remain unchanged under parity transformations. B map has polarization vectors with vorticity around any point, so B-mode is called divergence-free or curl mode. B-modes will flip sign under parity transformations.

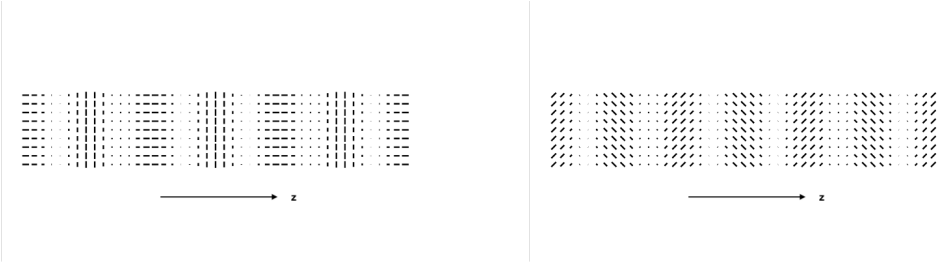

(a) E (b) B

Figure 1.2: Plane wave E and B modes travelling along direction **z**.

Because E and B are spin-0 fields, their power spectra take the same form as T in Eq.1.34. We can generalize the formula to include all possible auto and cross spectra

$$C_l^{XY} \equiv \frac{1}{2l+1} \sum_m \langle a_{lm}^{*X} a_{lm}^{Y} \rangle, \ X, Y = T, E, B \ . \tag{1.46}$$

The connection to the primordial power spectrum is

$$C_l^{XY} = \frac{2}{\pi} \int k^2 \mathrm{d}k P(k) \Delta_{X,l}(k) \Delta_{Y,l}(k) \ . \tag{1.47}$$

As proved by (Kamionkowski, Kosowsky, and Stebbins, 1997) and (Zaldarriaga and Seljak, 1997), scalar perturbations can generate T and E anisotropies in the CMB, but not B, while tensor perturbation can generate T, E, and B. The fact that B-mode polarization can only be generated by tensor perturbations makes it a unique tool for studying inflation.

By measuring B-mode in the CMB, we can constrain the ratio between the primordial tensor and scalar perturbations, r. The current upper limit is from (P. A. R. Ade, Z. Ahmed, Amiri, et al., 2021) $r < 0.036$ (95%CL). Constraints on r is usually plotted together with constraints on n_s in a 2D contour plot, as shown in Figure 1.3. Narrowing down the possible range of these parameters enables us to distinguish between different inflation models. With the latest r result, many once-popular models have already been ruled out at high confidence levels, including many among the single-field slow-roll model.

The amplitude of the polarization anisotropies are much smaller than the temperature. As shown in Figure.1.4, the highest peak of the EE spectrum is almost $1,000$

times lower than that of the TT spectrum. BB amplitude relates to the tensor-to-scalar ratio r. The current best constraint on r is $r_{0.05} < 0.36$, (95% CL), with $\sigma(r) = 0.009$ (P. A. R. Ade, Z. Ahmed, Amiri, et al., 2021). The expected BB spectrum at $r = 0.01$ is shown in Figure. 1.4. The BB peak at $l \approx 100$ is about 5 orders of magnitude smaller than EE and below the lensing signal.

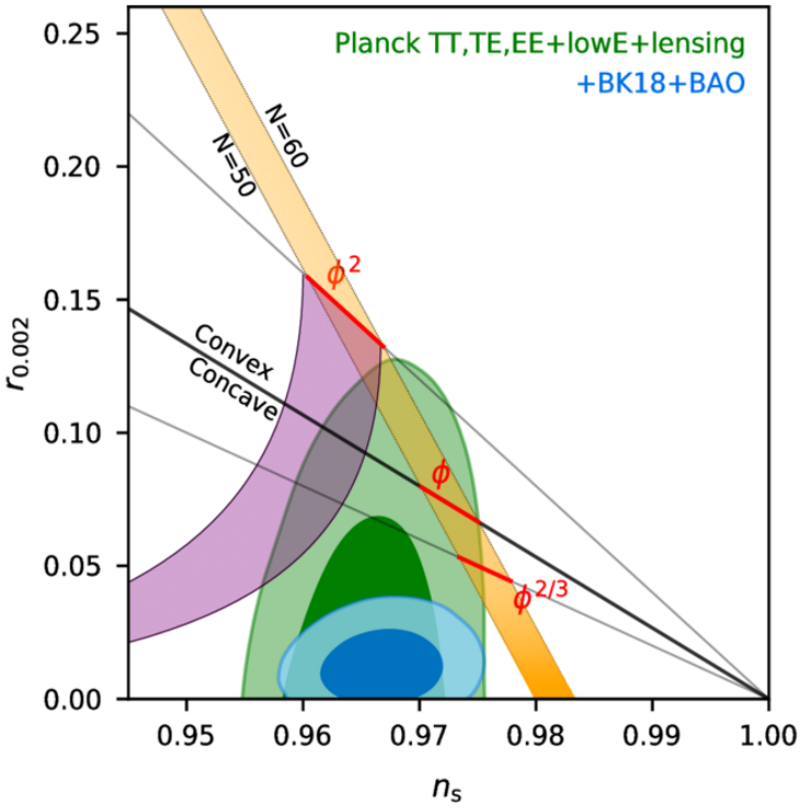

Figure 1.3: Constraints in the r vs. n_s plane for the Planck 2018 baseline analysis (Aghanim, Akrami, Ashdown, et al., 2020), and when also adding BICEP/*Keck* data through the end of the 2018 season plus BAO data to improve the constraint on n_s. The constraint on r tightens from $r_{0.05} < 0.11$ to $r_{0.05} < 0.035$. Some single-field models with polynomial potentials are plotted as black lines with 50 and 60 e-fold boundaries marked out. The natural inflation is shown as the purple band. All these once-popular models are now lying outside the 2σ contour with BK18 data.

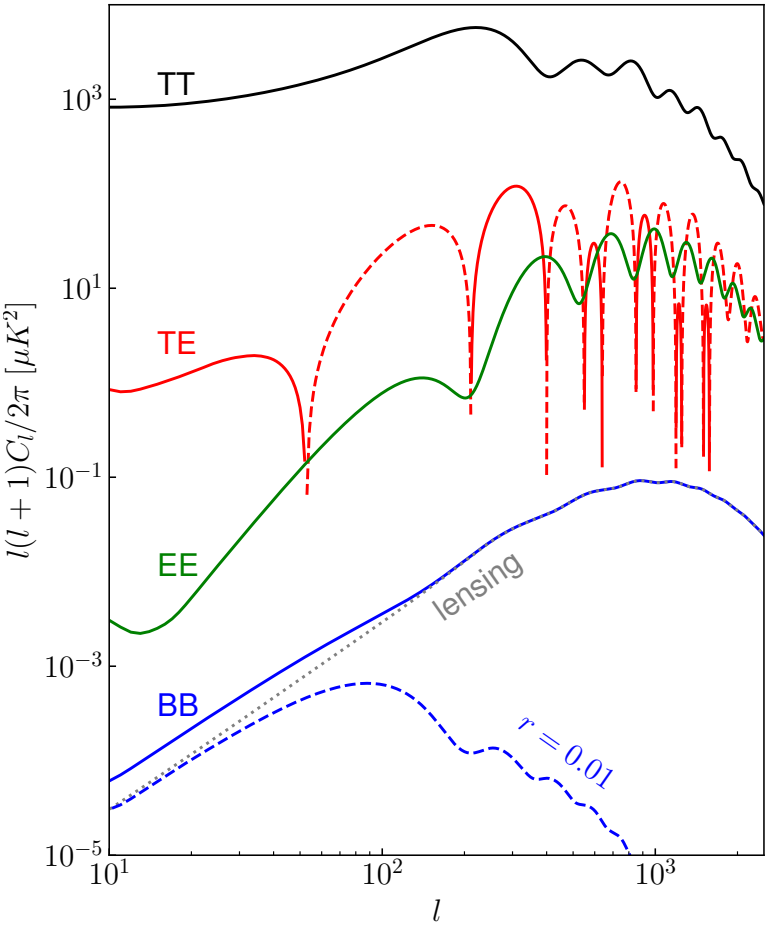

Figure 1.4: Angular Power Spectrum of CMB Temperature and Polarization anisotropies in the ΛCDM model as produced by CAMB (Lewis, Challinor, and Lasenby, 2000) from the Planck 2018 cosmological parameters (Aghanim, Akrami, Ashdown, et al., 2020). The dash blue line shows the expected unlensed BB spectrum at $r = 0.01$. As r gets smaller, delensing becomes more and more important on recovering the primordial B-mode signal.

Chapter 2

GALACTIC FOREGROUNDS

The Interstellar Medium (ISM) lies between us and the last scattering surface. The radiation from the ISM becomes foreground in CMB observations and requires proper treatments. Some foregrounds can be highly polarized, and their B to E polarization ratio is much higher than the primordial signals in the CMB. Although foreground was less of a concern for the CMB temperature anisotropies at high galactic latitude, it becomes a problem in the B-mode experiments.

There are two kinds of galactic foregrounds we care most about because of their high polarization fraction and abundance.

2.1 The Thermal Dust Radiation

The interstellar dust grains are heated by absorbing radiations from the background starlights. They are cooled down through thermal emission in far-infrared and sub-millimeters with a spectrum described as a modified black-body $\epsilon B(\nu, T_d)$, where ϵ depending on the dust property and frequency. The thermal dust has a typical T_d around 20 K. The dust radiation dominates in the higher frequency bands in CMB observations.

The thermal dust radiation is highly polarized. The polarization fraction can be as high as 20% (Aghanim, Akrami, Alves, et al., 2020). The dust polarization originates from its asymmetric shape and alignment with the galactic magnetic field. More discussion can be found in Chapter 3.

We model the polarized dust emission as

$$I_d(\nu, l) \propto l^{\alpha_d} \nu^{\beta_d} B(\nu, T_d) \tag{2.1}$$

α_d is the spatial power-law index, while β_d is the frequency power-law index of the emissivity. T_d is the thermal dust temperature, fixed at 19.6 K in our analysis. The amplitude of dust emission is usually quoted as $A_{d,353}^{l=80}$ in thermodynamic temperature unit at 353 GHz and multipole $l = 80$.

2.2 The Synctrotron Radiation

Relativistic charged particles gyrating ultra-relativistically in the galactic magnetic field emit highly polarized radiation. The direction of polarization is decided by both the orientation and the strength of the B-field. (Westfold, 1959). The predicted polarization fraction is as high as 70%, assuming a power-law SED of the electrons. The measured polarization fraction at high galactic latitude is only about 15%, suggesting substantial tangling of the B-field even on lines of sight looking out of the galactic disc(P. A. R. Ade, Aghanim, et al., 2016).

The spectral response of the synchrotron radiation can be approximated by a power law in the wavelength of interest. We describe the synchrotron foreground in our analysis as

$$I_s(\nu, l) \propto l^{\alpha_s} \nu^{\beta_s} \ . \tag{2.2}$$

α_s is the synchrotron spatial index. The spectral index β_s is around -3 due to the population distribution of high-energy cosmic rays. The negative spectral index makes the synchrotron radiation dominate in the lower frequency bands. $A_{s,23}^{l=80}$ is the synchrotron amplitude in thermodynamic $\mu\mathrm{K}^2$ unit at 23 GHz and multipole $l = 80$.

2.3 Component separation

We can separate the foregrounds from CMB using their very different spectral features. We use a multi-component, multi-spectrum likelihood analysis to constrain all parameters in our lensed-ΛCDM+dust+synchrotron+r module. The model we use has eight parameters, six of which are for the two foregrounds mentioned in the previous two sections, plus r and the dust-synchrotron correlation factor ε. The likelihood analysis uses all BK maps and the external polarization maps from WMAP and Planck. Early on, we almost entirely relied on the WMAP 23 GHz and Planck 353 GHz for constraining the foreground components in our sky area. In BK18(P. A. R. Ade, Z. Ahmed, Amiri, et al., 2021), for the first time, our own 220 GHz data is providing equal constraining power as the Planck 353, as shown in Figure 2.1. The high sensitivity data at 95 GHz from BICEP3 pushed down the upper limit of synchrotron by a lot, but it remains undetected due to the lack of constraining power from lower frequency bands. This motivated us to develop our low-frequency receiver to measure the synchrotron foreground in our sky patch.

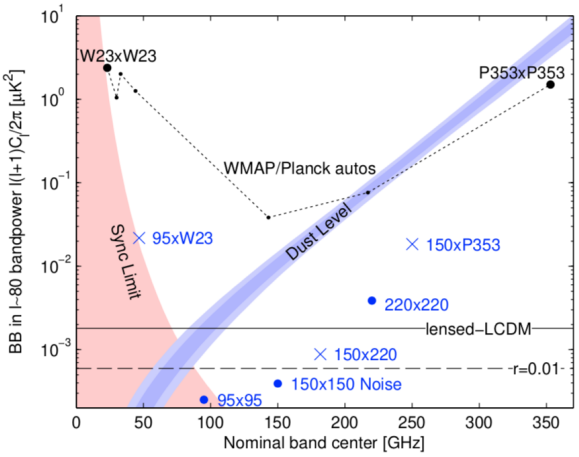

Figure 2.1: Expectation values and noise uncertainties of the $l \sim 80$ BB bandpower in BK field. The color bands are the 95% synchrotron upper limit (red) and the 1 and 2 σ constraint on dust (blue). The black horizontal dashed line is the expected bandpower for the primordial BB assuming $r = 0.01$, well below the lensed-ΛCDM level. The blue dots and crosses are the noise uncertainties of all the auto- and cross-spectra involving BK data. The black dots are the noise uncertainties of the external data used in the analysis. Plot from (P. A. R. Ade, Z. Ahmed, Amiri, et al., 2021).

Chapter 3

AN IMPRINT OF THE GALACTIC MAGNETIC FIELD IN THE DIFFUSE UNPOLARIZED DUST EMISSION

From the discovery of starlight polarization induced by dichroic extinction in the interstellar medium (ISM, Hiltner, 1949; Hall, 1949) and articulation of a theory of grain alignment (Davis and Greenstein, 1951; Spitzer and Tukey, 1951), measurements of dust extinction and emission have been recognized as a way to trace magnetic fields (Hiltner, 1951; Stein, 1966). While historically starlight polarization has been and continues to be a powerful probe of magnetic fields in the interstellar medium (e.g., Clemens et al., 2012; Planck Collaboration Int. XXI, 2015; Panopoulou et al., 2019), the relatively recent advent of sensitive ground-based, stratospheric, and space-based probes of polarized far-infrared (FIR) dust emission has opened new windows to study magnetic fields in molecular clouds, protoplanetary disks, and the diffuse ISM (e.g., Benoît et al., 2004; Galitzki et al., 2014; Stephens et al., 2014; Planck Collaboration Int. XIX, 2015; Ward-Thompson et al., 2017; Chuss et al., 2019). In particular, maps of polarized dust emission from the Planck satellite enable mapping of magnetic fields across the entire sky (Planck Collaboration Int. XX, 2015; Planck Collaboration XII, 2018).

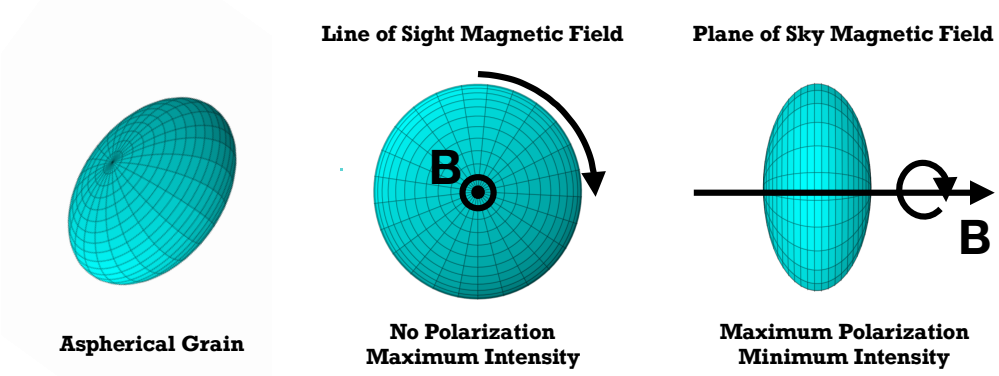

Figure 3.1: Schematic illustrating the effect of orientation on dust intensity and polarization. Grains rotate about their shortest principal axis, and the rotation axis is systematically aligned with the interstellar magnetic field. Therefore, the grain has a larger effective cross section, and thus greater emission, when the magnetic field is oriented along the line of sight than in the plane of the sky. In contrast, grain rotation eliminates polarization when the magnetic field is along the line of sight, while polarization is maximal when the magnetic field is in the plane of the sky.

Because of the importance of the Galactic magnetic field in many areas of astrophysics, including cosmic ray propagation, the formation and structure of the Milky Way, and polarized foregrounds for Cosmic Microwave Background (CMB) science, constraining its morphology has been the subject of much research (see Jaffe, 2019, for a recent review). With the sensitive, full-sky Planck maps, dust emission is actively being used to complement other tracers, such as synchrotron emission and pulsar rotation measures, yielding insights on both the large-scale field morphology and the Local Bubble (e.g., Planck Collaboration Int. XLII, 2016; Alves et al., 2018; Pelgrims and Macıas-Pérez, 2018; Skalidis and Pelgrims, 2019).

However, the dust polarization angle as determined from measurements of the Stokes Q and U parameters is sensitive only to the plane of sky component of the Galactic magnetic field. In this work, we describe a new method for constraining the line of sight component of the magnetic field, and thus the full 3D orientation, using the total (i.e., unpolarized) intensity and the HI column density.

Emission from interstellar dust grains dominates the spectral energy distribution (SED) of the Galaxy from FIR to microwave wavelengths. The interstellar magnetic field aligns dust grains such that their short axes are parallel to the field direction (see Andersson, Lazarian, and Vaillancourt, 2015, for a review). Since grains emit photons preferentially with electric field oriented along the long axis of the grain, the resulting emission from a population of dust grains is polarized. Observations of polarized dust emission allow straightforward determination of the orientation of the interstellar magnetic field projected onto the plane of the sky. When the magnetic field lies in the plane of the sky, the polarization is maximal, while the polarization vanishes when the magnetic field is parallel to the line of sight. This effect accounts for much of the variation in the dust polarization fraction across the sky, though averaging of multiple magnetic field orientations along the line of sight is also an important contributor (Clark, 2018).

While the effect of the viewing angle is most readily apparent in polarization, in principle the total intensity of dust emission also depends on the angle between the line of sight and the interstellar magnetic field (Lee and Draine, 1985). This arises simply because the effective cross section of an aspherical grain changes with viewing angle. Consequently, the effective cross section of dust grains, and thus the total emission per grain, is larger when the magnetic field is along the line of sight, and smaller when it lies in the plane of the sky, as illustrated in Figure 3.1. Using the Planck 353 GHz data, we present the first detection of this effect in intensity.

In addition to mapping magnetic fields, the dust polarization angles and their statistics provide tests of models of magnetohydronamic (MHD) turbulence. For instance Planck Collaboration XII (2018) found that the dispersion in polarization angles is best reproduced by models with strong turbulenceequipartition between the ordered and turbulent magnetic field. In this work, we demonstrate that the polarization angle dispersion function $\mathcal{S}$ is strongly influenced byis driven primarily by the orientation of the Galactic magnetic field with respect to the line of sight , which may complicate this interpretation.

3.1 Theory

Emission and Polarization from Aligned Grains

While the actual shapes of interstellar grains are unknown, they are often modeled as spheroids or ellipsoids. For generality, we model dust grains as triaxial ellipsoids with principal axes $a_1 \leq a_2 \leq a_3$. Let $\hat{a}_1$, $\hat{a}_2$, and $\hat{a}_3$ be unit vectors along the respective axes. Suprathermally rotating interstellar grains spin about their short axis, i.e., angular momentum $J \parallel \hat{a}_1$. Paramagnetic dissipation brings J into alignment with the interstellar magnetic field B, and so perfectly aligned grains have $\hat{a}_1 \parallel B$.

In this work, we model polarized dust emission at $\lambda = 850\,\mu$m, which is much larger than the size of interstellar grains ($a \lesssim 0.1\,\mu$m). In the limit of $a/\lambda \ll 1$, i.e., the "electric dipole limit," the polarization cross section of an arbitrarily oriented grain can be written in terms of the cross sections for photons propagating along the principal axes. For non-magnetic grains in the electric dipole limit, this reduces to just the three cross sections C^1_{abs}, C^2_{abs}, and C^3_{abs}, which are the absorption cross sections for photons polarized with E parallel to $\hat{a}_1$, $\hat{a}_2$, and $\hat{a}_3$, respectively. In the limit of perfect internal alignment, grain rotation further simplifies the analysis by time averaging C^2_{abs} and C^3_{abs} irrespective of the grain orientation.

Under these assumptions, the absorption cross section for randomly oriented grains C^{ran}_{abs} is given by

$$C^{ran}_{abs} = \frac{1}{3}\left(C^1_{abs} + C^2_{abs} + C^3_{abs}\right) \ . \tag{3.1}$$

A population of randomly-oriented grains produces no net polarization.

Now consider a population of grains with $\hat{a}_1$ perfectly aligned with B. Let ψ be the angle between the line of sight and B. The total and polarized absorption cross sections can be defined relative to two orthogonal polarization modes:

$$C_{abs} \equiv \frac{1}{2}\left(C_{abs}^{\perp} + C_{abs}^{\parallel}\right) \tag{3.2}$$

$$C_{pol} \equiv \frac{1}{2}\left(C_{abs}^{\perp} - C_{abs}^{\parallel}\right) \ . \tag{3.3}$$

We define $C_{abs}^{\perp}$ and $C_{abs}^{\parallel}$ relative to the orientation of B projected onto the plane of the sky. With this definition, perfectly aligned grains have total and polarized absorption cross sections

$$C_{abs}^{align} = \frac{1}{2}\left(C_{abs}^{2} + C_{abs}^{3}\right)\cos^2\psi + \frac{1}{2}\left[C_{abs}^{1} + \frac{1}{2}\left(C_{abs}^{2} + C_{abs}^{3}\right)\right]\sin^2\psi \tag{3.4}$$

$$C_{pol}^{align} = \frac{1}{2}\left[\frac{1}{2}\left(C_{abs}^{2} + C_{abs}^{3}\right) - C_{abs}^{1}\right]\sin^2\psi \ , \tag{3.5}$$

respectively.

Grain alignment and disalignment mechanisms operate on finite timescales and so in any environment there will be a distribution of angles between the grain angular momenta J and B, with J tending to precess around B. However, in the electric dipole limit, this can be accurately approximated by assuming a fraction f of grains are perfectly aligned with B and the remaining $(1-f)$ are randomly oriented (Dyck and Beichman, 1974). Thus,

$$C_{abs} = f C_{abs}^{align} + (1-f)\, C_{abs}^{ran} \tag{3.6}$$

$$C_{pol} = f C_{pol}^{align} \ . \tag{3.7}$$

In the electric dipole limit, the absorption cross section per unit grain volume V is independent of grain size. Assuming the grains have mass density ρ, it is convenient to define the opacities

$$\kappa_{\nu}^{ran} = \frac{1}{3\rho V}\left(C_{abs}^{1} + C_{abs}^{2} + C_{abs}^{3}\right) \tag{3.8}$$

$$\kappa_{\nu}^{pol} = \frac{1}{2\rho V}\left[\frac{1}{2}\left(C_{abs}^{2} + C_{abs}^{3}\right) - C_{abs}^{1}\right] \tag{3.9}$$

such that a population of grains with mass surface density Σ_d and temperature T_d emits total and polarized intensities

$$I_\nu = \Sigma_d B_\nu\left(T_d\right)\left[\kappa_\nu^{ran} + f\kappa_\nu^{pol}\left(\frac{2}{3} - \sin^2\psi\right)\right] \tag{3.10}$$

$$P_\nu = \Sigma_d B_\nu\left(T_d\right) f\kappa_\nu^{pol}\sin^2\psi\ , \tag{3.11}$$

where $B_\nu\left(T\right)$ is the Planck function. The dust polarization fraction p_ν is defined as

$$p_\nu \equiv \frac{P_\nu}{I_\nu} = \frac{f\sin^2\psi}{1 + \frac{\kappa_\nu^{pol}}{\kappa_\nu^{ran}} f\left(\frac{2}{3} - \sin^2\psi\right)} \frac{\kappa_\nu^{pol}}{\kappa_\nu^{ran}}\ . \tag{3.12}$$

Since we employ $N_{\rm HI}$ as a proxy for the dust column, we define the dust to gasHI mass ratio δ_{DG} as

$$\delta_{DG} \equiv \frac{\Sigma_d}{m_p N_{\rm HI}}\ , \tag{3.13}$$

where m_p is the proton mass. Combining these equations, we obtain our principal result:

$$\frac{I_\nu}{N_{\rm HI}} = \left(\kappa_\nu^{ran} + \frac{2f}{3}\kappa_\nu^{pol}\right) m_p \delta_{DG} B_\nu\left(T_d\right) - \frac{P_\nu}{N_{\rm HI}}\ . \tag{3.14}$$

If the dust properties κ_ν^{ran}, κ_ν^{pol}, f δ_{DG}, and T_d are not varying across the sky, we expect a negative correlation between the observed $I_\nu/N_{\rm HI}$ and $P_\nu/N_{\rm HI}$ with slope of -1.

Instead of working with the limiting cases of perfect alignment and random orientation, the effects of imperfect grain alignment can be parameterized by the Rayleigh reduction factor $\mathcal{R}$ (Greenberg, 1968). $\mathcal{R}$ accounts for the distribution of angles θ between J and B and is given by

$$\mathcal{R} \equiv \frac{3}{2}\left(\langle\cos^2\theta\rangle - \frac{1}{3}\right)\ . \tag{3.15}$$

In the case of both oblate ($C_{abs}^2 = C_{abs}^3$) and prolate ($C_{abs}^1 = C_{abs}^2$) spheroidal grains, the equations for the total and polarized intensities in the electric dipole limit are recovered from our results by simply replacing the alignment fraction f with $\mathcal{R}$ (Lee and Draine, 1985; Draine and Hensley, 2016).

This derivation assumes all dust emission is associated with a single magnetic field orientation. In reality, averaging of multiple orientations both along the line of

sight and within the beam is expected. These effects typically reduce the level of polarization and bring $I_\nu/N_{\rm HI}$ closer to the mean value.

The Polarization Angle Dispersion Function

The polarized emission from interstellar dust is characterized by the Stokes parameters Q_ν and U_ν, which are directly observable. When expressed as specific intensities, they are related to the polarized intensity by

$$Q_\nu = P_\nu \cos 2\chi \tag{3.16}$$

$$U_\nu = P_\nu \sin 2\chi \ , \tag{3.17}$$

where χ is the polarization angle and Stokes V has been assumed to be zero. For electric dipole emission from dust grains aligned with $\hat{a}_1 \parallel B$, χ is the angle perpendicular to the projection of B onto the plane of the sky. The numerical value of χ depends on the adopted polarization convention.

The polarization angle dispersion function $\mathcal{S}$ is a measure of the spatial variability of χ over a given region. For a given pixel i on the sky, $\mathcal{S}$ is computed over a region R such that

$$\mathcal{S}_i = \sqrt{\frac{1}{N}\sum_{j\in R}\left(\chi_j - \chi_i\right)^2} \ , \tag{3.18}$$

where the sum is over the N pixels in R. In practice, R is often taken to be annulus centered on pixel i of width equal to the radius of its inner edge (see Section 3.2). Note that $\mathcal{S}$ is not dependent on the adopted polarization convention, though care should be taken to avoid computing $\mathcal{S}$ near singularities in the coordinate system (see discussion in Planck Collaboration Int. XIX, 2015).

Interpretation of $\mathcal{S}$ can be subtle as a number of effects can give rise to dispersion in the polarization angle. For instance, $\mathcal{S}$ will be high in a region in which the magnetic field is relatively disordered. Indeed, measurements of $\mathcal{S}$ (and the closely related structure function) have been used to constrain models of interstellar turbulence in clouds and in the diffuse ISM (e.g. Hildebrand et al., 2009; Houde et al., 2009; Poidevin et al., 2013; Planck Collaboration Int. XX, 2015; Planck Collaboration XII, 2018). Disorder in the magnetic field along the line of sight can likewise induce spatial variability in the measured polarization angles, as can instrumental noise in the Q_ν and U_ν measurements.

The magnitude of each of these effects is modulated by the angle ψ between the line of sight and B (Falceta-Gonçalves, Lazarian, and Kowal, 2008; Poidevin et al., 2013; Planck Collaboration Int. XX, 2015; King et al., 2018). If B is nearly along the line of sight, then even small perturbations to the 3D field orientation can induce large changes in χ, leading to large values of $\mathcal{S}$. In contrast, if B lies mostly in the plane of the sky, small perturbations to its 3D orientation have only a modest impact on χ, resulting in small values of $\mathcal{S}$. This connection between $\mathcal{S}$ and ψ is consistent with the strong empirical anticorrelation between $\mathcal{S}$ and the dust polarization fraction p_ν observed over a large range of column densities (Planck Collaboration Int. XIX, 2015; Fissel et al., 2016; Planck Collaboration XII, 2018).

The p_ν–$\mathcal{S}$ relation is often parameterized with a power law. Over the full sky, Planck Collaboration XII (2018) found that $p_\nu \propto \mathcal{S}^{-1}$ while Fissel et al. (2016) found that $p_\nu \propto \mathcal{S}^{-0.67}$ in the Vela C Molecular Cloud. Given these results, we hypothesize that over the diffuse high latitude sky,

$$\sin^2 \psi \propto \mathcal{S}^n \ . \tag{3.19}$$

Under this assumption, Equations 3.10 and 3.11 can be rewritten as

$$\frac{I_\nu}{N_{\rm HI}} = A - B \left(\frac{\mathcal{S}}{1^\circ} \right)^n \tag{3.20}$$

$$\frac{P_\nu}{N_{\rm HI}} = B \left(\frac{\mathcal{S}}{1^\circ} \right)^n \ , \tag{3.21}$$

where A, B, and n are global mean values with scatter induced by variations in dust properties, such as the dust temperature and dust to gas ratio. In this work, we find that the observed relationship between I_ν and P_ν in the low column density sky ($N_{\rm HI} < 4 \times 10^{20}\,{\rm cm}^{-2}$) is well described by this model.

3.2 Data

In this section we introduce the data sets used in this work. Our principal analysis is performed on HEALPix[1] (Górski et al., 2005) maps smoothed to a resolution of $160'$ with $N_{side} = 64$.

[1] `https://healpix.sourceforge.io/`

Dust Emission Maps

The 353 GHz band was the highest-frequency Planck channel designed for polarimetry. Dominated by thermal dust emission, it is ideal for studying dust polarization properties across the sky.

Like Planck Collaboration XII (2018), we are interested in the astrophysical properties of Galactic dust and therefore require maps minimally contaminated by other sources of emission, notably the CMB and the Cosmic Infrared Background (CIB). We therefore follow Planck Collaboration XII (2018) in utilizing the component-separated maps produced by application of the Generalized Needlet Internal Linear Combination (GNILC) algorithm (Remazeilles, Delabrouille, and Cardoso, 2011) to the Planck data (Planck Collaboration IV, 2018). Critically for this study, these maps were created with the intention of separating the contributions of the CIB and Galactic dust by exploiting both spatial and spectral information. This is not true of the dust maps made with the Commander parametric component separation algorithm, in which both CIB and Galactic dust emission are absorbed in the "thermal dust" component (Planck Collaboration X, 2016; Planck Collaboration IV, 2018).

We employ the 2018 GNILC Stokes I, Q, and U maps[2] at 353 GHz. We smooth the maps to 160′ resolution and repixellate them at $N_{side} = 64$. Following Planck Collaboration XII (2018), we subtract 389 $\mu\mathrm{K}_{CMB}$ from the I map to account for zero level offsets from, e.g, the CIB monopole,(-452 $\mu\mathrm{K}_{CMB}$ for the CIB monopole and +63 $\mu\mathrm{K}_{CMB}$ for the Galactic offset) and convert to MJy sr^{-1} with the factor 287.5 MJy sr^{-1} $\mu\mathrm{K}_{CMB}^{-1}$ (Planck Collaboration III, 2018). The P map is obtained via $P = \sqrt{Q^2 + U^2}$. Because of the substantial smoothing, the noise bias is very small even at low column densities (Planck Collaboration XII, 2018), and so we do not perform any debiasing.

Polarization Angle Dispersion Function

Employing the 353 GHz GNILC Q and U maps, Planck Collaboration XII (2018) constructed maps of the polarization angle dispersion function $\mathcal{S}$ (see Equation 3.18) at different resolutions. In all cases, they computed $\mathcal{S}$ on an annulus with inner radius $\delta/2$ and outer radius $3\delta/2$, where the "lag" δ is taken to be half the resolution of the map. They found that the map of $\mathcal{S}$ computed at 80′ resolution ($\delta = 40'$) was affected by noise bias and so recommended resolution 160′ ($\delta = 80'$) when computing $\mathcal{S}$. In this work, we employ their map[3] of $\mathcal{S}$ at 160′ pixellated at $N_{side} = 64$. With this

[2] COM_CompMap_IQU-thermaldust-gnilc-unires_2048_R3.00.fits

[3] V. Guillet, private comm.

resolution, we find that debiasing would have a 10% or greater effect on the value of $\mathcal{S}$ in less than 1% of the high latitude pixels considered in this work. Therefore, as with the P map, we do not perform any debiasing, and we have verified that this choice does not affect any of our conclusions. The $\mathcal{S}$ map requires the coarsest resolution of all data products analyzed, and so we smooth all other maps to this resolution.

HI Map

The 21 cm line from atomic H has been mapped spectroscopically over the Southern Hemipshere by the Parkes Galactic All-Sky Survey (GASS, McClure-Griffiths et al., 2009) and the Northern Hemisphere by the Effelsberg-Bonn *HI* Survey (EBHIS, Kerp et al., 2011). These datasets have been combined and homogenized by the HI4PI Survey (HI4PI Collaboration et al., 2016) to a uniform $16.'2$ resolution over the full sky. In this work, we employ the $N_{\rm HI}$ map[4] derived from the HI4PI data by Lenz, Hensley, and Doré (2017), which filters out all HI emission having radial velocity $|v_{LSR}| > 90\,{\rm km\,s^{-1}}$. Such high velocity gas was found to have little correlation with dust reddening (Lenz, Hensley, and Doré, 2017), and so the filtered map provides a better predictor of the dust column. Additionally, this velocity-filtered map is free from extragalactic contamination down to very low levels (Chiang and Ménard, 2019). We smooth the HI map to a resolution of $160'$ and repixellate to $N_{side} = 64$.

All analysis in this work is restricted to lines of sight with $N_{\rm HI} < 4 \times 10^{20}\,{\rm cm^{-2}}$, where the HI column density has been shown to be a linearly related to the dust column density (Lenz, Hensley, and Doré, 2017). At $160'$ resolution and $N_{side} = 64$, this corresponds to a sky fraction of 39% and 19,120 pixels.

Dust Temperature Map

In addition to its application to the Planck data, the GNILC algorithm has also been employed on the IRIS 100 μm map (Miville-Deschênes and Lagache, 2005), a reprocessing of the IRAS 100 μm map (Wheelock et al., 1994), to derive multi-frequency Galactic dust SEDs across the sky (Planck Collaboration Int. XLVIII, 2016). The Planck and IRIS Galactic dust maps were then fit with a modified blackbody emission model to derive full-sky maps of dust temperature T_d that are minimally contaminated by CIB emission. We employ the resulting T_d map[5], which has a native resolution of approximately $5'$ and is pixellated with $N_{side} = 2048$. We

[4] `https://doi.org/10.7910/DVN/AFJNWJ`

[5] COM_CompMap_Dust-GNILC-Model-Temperature_2048_R2.00.fits

smooth this map to $160'$ resolution and repixellate to $N_{side} = 64$.

In principle, maps of T_d should not be smoothed by simple averaging but rather by redoing the parameter fits on smoothed intensity maps. We investigate the potential impact of smoothing on T_d in Section 3.3 and find our principal conclusions relating to T_d also hold at $16.'2$ resolution, suggesting that such effects are not important for our analysis.

3.3 Data Model

Statistical Model

The principal aim of this work is to assess whether the observed 353 GHz dust intensity per $N_{\rm HI}$ has a statistically significant correlation with the orientation of the Galactic magnetic field relative to the line of sight. The maps of the dust intensity and HI intensity employed in this study have high signal-to-noise, and the maps of the polarized intensity and polarization angle dispersion $\mathcal{S}$ are also signal dominated because of the aggressive smoothing. However, $I_\nu/N_{\rm HI}$ and $P_\nu/N_{\rm HI}$ are expected to have large astrophysical scatter owing to changes in, e.g, the dust to gas ratio, dust composition, and dust temperature in addition to the orientation effect we seek.

In Section 3.4, we investigate the relationship between $I_\nu/N_{\rm HI}$ and $P_\nu/N_{\rm HI}$ predicted by Equation 3.14. While the magnetic field orientation induces a negative correlation with slope $m = -1$, variations in other properties such as dust temperature and dust to gas ratio induce a positive correlation. To test whether a statistically significant negative correlation is present in the data, we employ the likelihood function

$$\mathcal{L} \propto \prod_i \frac{1}{\sigma_I}\, exp\left[-\frac{\left(I_\nu/N_{HI,i} - mP/N_{HI,i} - b\right)^2}{\sigma_I^2}\right], \tag{3.22}$$

where we have assumed a linear relationship with slope m and intercept b. σ_I is the random scatter in the $I_\nu/N_{\rm HI}$ measurements and is assumed to be constant across the sky. While this model enables determination of whether or not a trend exists between $I_\nu/N_{\rm HI}$ and $P_\nu/N_{\rm HI}$, it does not take into account that pixel-to-pixel variations in these two quantities can be strongly correlated. We discuss these correlated variations in Section 3.4.

In Section 3.4, we employ Equations 3.20 and 3.21 to model the relations between $I_\nu/N_{\rm HI}$, $P_\nu/N_{\rm HI}$, and $\mathcal{S}$. We fit for the parameters A, B, and n in the model using

the observations of both $I_\nu/N_{\rm HI}$ and $P_\nu/N_{\rm HI}$. We employ the likelihood function

$$\mathcal{L} \propto \prod_i \frac{1}{\sigma_I \sigma_P}\, exp\left[-\frac{\left(I_{\nu,i}/N_{HI,i} - A + B\mathcal{S}_i^n\right)^2}{\sigma_I^2}\right] \times exp\left[-\frac{\left(P_{\nu,i}/N_{HI,i} - B\mathcal{S}_i^n\right)^2}{\sigma_P^2}\right], \tag{3.23}$$

where σ_I and σ_P are the random scatter in the $I_\nu/N_{\rm HI}$ and $P_\nu/N_{\rm HI}$ measurements, respectively.

All model fitting is performed with the `emcee` Markov Chain Monte Carlo software[6] (Foreman-Mackey et al., 2013). For all parameters, we employ broad, uninformative priors.

Dust Temperature Correction

The total and polarized emission from a fixed amount of dust are sensitive to the dust temperature (see Equations 3.10 and 3.11), with the long-wavelength emission scaling as the first power of T_d in the Rayleigh-Jeans limit. Dust temperature variations add scatter to $I_\nu/N_{\rm HI}$ and $P_\nu/N_{\rm HI}$ unrelated to orientation effects. Even more critically, T_d fluctuations affect $I_\nu/N_{\rm HI}$ and $P_\nu/N_{\rm HI}$ in the same manner, inducing a positive correlation between these quantities. This effect minimizes and potentially eliminates the negative correlation expected between these quantities from orientation effects (see Equation 3.14). We therefore seek to mitigate the effects of dust temperature by employing a dust temperature map obtained from SED fitting. However, we find that, over this range of column densities, the available dust temperature maps do not improve upon simply assuming a constant temperature.

The correlation between the dust intensity and $N_{\rm HI}$ is remarkably tight, and should tighten further when a correction is made for T_d variations. In Figure 3.2, we use the GNILC T_d map to plot $I_\nu/B_\nu\,(T_d)$ against $N_{\rm HI}$, finding that the T_d-corrected intensity map is indeed tightly correlated with $N_{\rm HI}$. However, in Figure 3.2 we present the same plot but instead assuming a sky-constant $T_d = 19.6$ K. We find that this relationship has even less scatter, i.e., the GNILC T_d map appears to make the I_ν–$N_{\rm HI}$ correlation worse.

We are examining here the lowest column densities on the sky, and therefore the regions of lowest signal-to-noise on the dust emission. It is therefore possible that variations in the T_d map are driven by noise. To investigate this further, we

[6] `https://emcee.readthedocs.io/en/v2.2.1/`

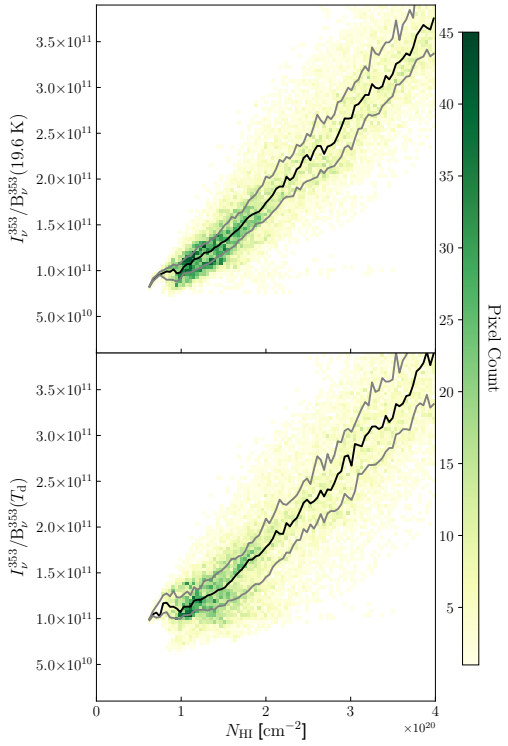

Figure 3.2: Relationship between N_{HI} and the 353 GHz dust intensity I_ν. Top: On the y-axis, I_ν is divided by the blackbody function at $T_d = 19.6\,\mathrm{K}$. The black line is the running median while the gray lines are the 25th and 75th percentiles. Bottom: Instead of assuming a constant T_d, I_ν is by the blackbody function evaluated at the T_d determined by SED fits to the GNILC component separated maps (Planck Collaboration Int. XLVIII, 2016). The dust temperature correction does not improve the scatter or the linearity of the relation.

present the correlation between I_ν/N_{HI} and T_d in the left panel of Figure 3.3. We expect a strong positive correlation in this space since hotter dust produces more long-wavelength emission per grain, yet there is no apparent trend in the data.

In contrast, as shown in the right panel of Figure 3.3, we find a strong positive correlation between N_{HI} and T_d for $N_{\mathrm{HI}} < 2 \times 10^{20}\,\mathrm{cm}^{-2}$. While it is possible that the lowest column density sightlines have systematically cooler dust, it seems more likely that this correlation is driven by the fitting degeneracy between the dust column and the dust temperature. If the effects of T_d on the shape of the dust SED cannot be adequately constrained due to low signal-to-noise, then both T_d and the normalization parameter both have the effect of increasing the overall amplitude of the dust emission. Thus, an artificial correlation between T_d and the true dust column can emerge. This may also explain why the effect is limited to only the very lowest values of N_{HI}, where the signal-to-noise on the dust SED is the lowest.

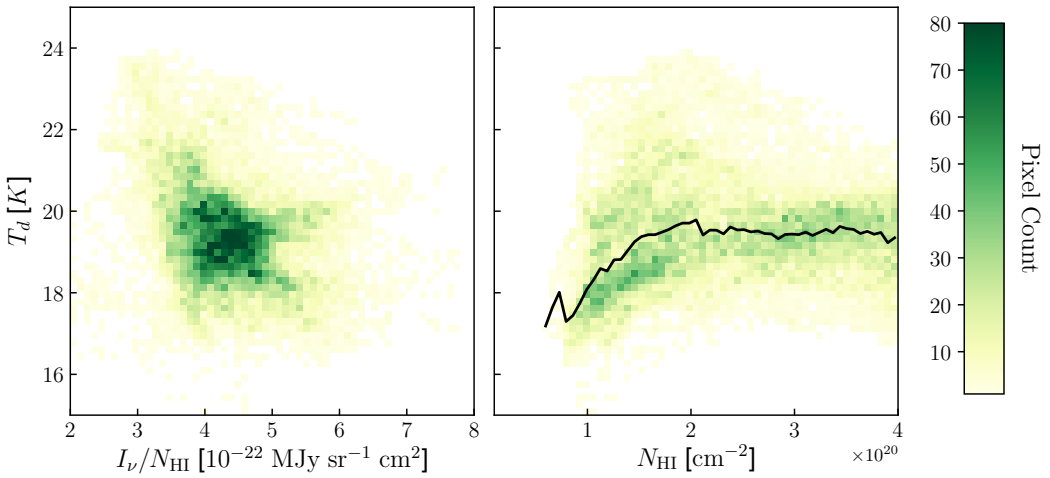

Figure 3.3: Left: 2D histogram of $I_\nu/N_{\rm HI}$ versus dust temperature T_d. In principle, higher temperature dust should emit more radiation per H, but the expected positive correlation is not evident. Right: The relationship between the HI column density and dust temperature. No a priori correlation is expected in the diffuse gas examined here. However, a positive correlation is evident for $N_{\rm HI} < 2.0 \times 10^{20}\, cm^{-2}$ as highlighted by the running median (black solid line). This may reflect a systematic trend that the lowest column density gas happens to have cooler dust temperatures, or may be an artifact of model fitting, as discussed in the text.

This analysis employed the GNILC dust temperature maps smoothed to 160′ as described in Section 3.2. Such aggressive smoothing, particularly by simple averaging of T_d across pixels, could induce biases in the map. However, the effects seen here persist even at the limiting 16.′2 resolution of the $N_{\rm HI}$ map. It seems therefore unlikely that the issues identified in the T_d map are solely the result of smoothing.

Finally, we attempted a dust temperature correction using the `Commander` T_d map instead (Planck Collaboration X, 2016). However, it is also unable to improve the I_ν–$N_{\rm HI}$ correlation relative to assuming a constant T_d. In addition to being subject to similar issues as the GNILC map, this alternative dust temperature map is more prone to CIB contamination since CIB anisotropies were not fit as a separate component from Galactic dust. For a more in-depth exploration of these issues in presently-available dust temperature maps, see Herman (2019).

We therefore conduct our analysis without a dust temperature correction, effectively assuming that T_d is constant over the diffuse high-latitude sky.

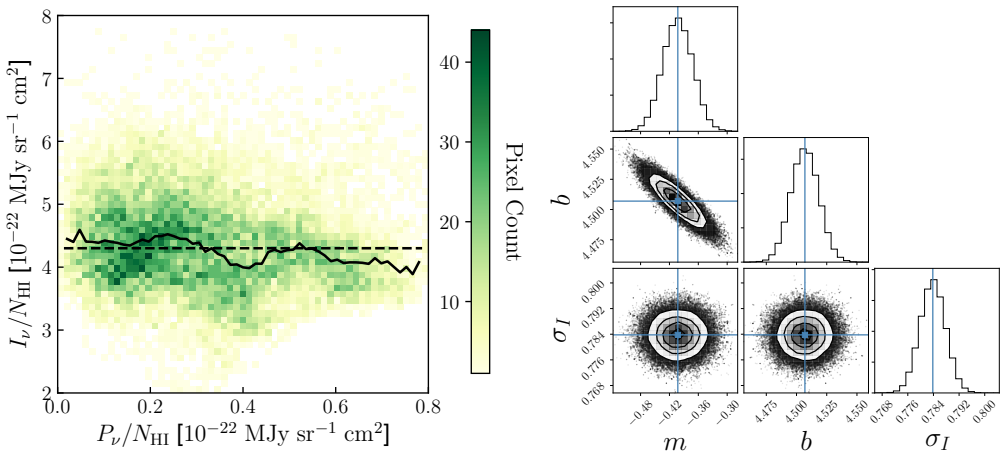

Figure 3.4: Left: 2D histogram of $I_\nu/N_{\rm HI}$ and $P_\nu/N_{\rm HI}$ for the 39% of the sky having $N_{\rm HI} < 4.0\times10^{20}\,cm^{-2}$. The overall mean is plotted as a black dashed line while the black solid line is the running median. Right: Posterior distributions of fit parameters after applying the fitting formalism of Section 3.3. Best fit values are indicated with solid blue lines and are $m = -0.40^{+0.03}_{-0.03}$, $b = 4.51^{+0.01}_{-0.01} \times 10^{22}$ MJy sr^{-1} cm^2, $\sigma_I = 0.784^{+0.004}_{-0.004} \times 10^{22}$ MJy sr^{-1} cm^2.

3.4 Results

$I_\nu/N_{\rm HI}$–$P_\nu/N_{\rm HI}$ Correlation

The most direct test of the sensitivity of the total dust intensity to the magnetic field orientation is the predicted anti-correlation between $I_\nu/N_{\rm HI}$ and $P_\nu/N_{\rm HI}$ (see Equation 3.14). In the left panel of Figure 3.4, we present the 2D histogram of these quantities over all pixels having $N_{\rm HI} < 4\times10^{20}$ cm^{-2}. The running median suggests a slight tendency for low values of $P_\nu/N_{\rm HI}$ to correspond to high values of $I_\nu/N_{\rm HI}$ and vice-versa, but the effect is not strong (Spearman rank coefficient $\rho = -0.15$).

We quantify the significance of the linear trend using Equation 3.22 and the formalism presented in Section 3.3. We indeed find a statistically significant preference for a negative slope, $m = -0.40 \pm 0.03$, even given the degeneracy with the fit intercept. The posterior distributions for each of the three fit parameters (m, b, and σ_I) are given in the right panel of Figure 3.4.

Even if the negative correlation is robust, the slope is much shallower than the expected -1. However, positive correlations between $I_\nu/N_{\rm HI}$ and $P_{\rm HI}/N_{\rm HI}$ are easily induced from fluctuations in the dust to gas ratio, dust temperature, and dust opacity. Indeed, we find that $\sim$ 10% variations in T_d in Equations 3.10 and 3.11 are alone sufficient to reduce the slope to values comparable to what is observed. Further, systematic errors in separation of the Galactic dust from the CIB induces scatter in

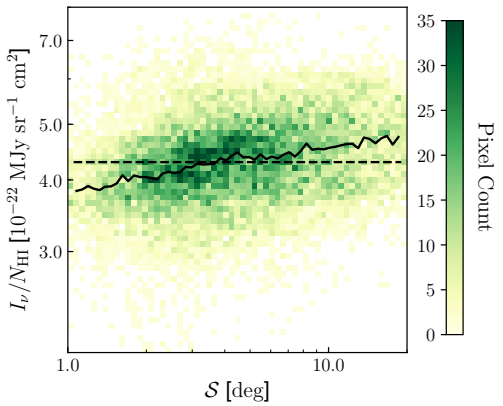

Figure 3.5: 2D histogram of $I_\nu/N_{\rm HI}$ and $\mathcal{S}$ for the 35% of the sky having $N_{\rm HI} < 4.0 \times 10^{20}\, cm^{-2}$ and $1^\circ < \mathcal{S} < 20^\circ$. As in Figure 3.4, the overall mean is plotted as a black dashed line while the black solid line is the running median. The Spearman rank coefficient $\rho = 0.29$.

$I_\nu/N_{\rm HI}$ and potentially also correlations in this space. That the negative correlation induced by the orientation of B persists despite these complicating factors is indicative of the homogeneity of dust properties in the diffuse high latitude sky. A more robust correlation could likely be extracted with a higher fidelity map of T_d, and indeed the strength of this correlation may be a means of validating future dust temperature maps.

$I_\nu/N_{\rm HI}$–$\mathcal{S}$ Correlation

While the $I_\nu/N_{\rm HI}$–$P_\nu/N_{\rm HI}$ anti-correlation may be the most direct probe of the effect of the magnetic field orientation on the unpolarized dust emission, it is complicated by physical variations in dust properties that induce a positive correlation between these quantities, as discussed in the previous section. Therefore, we seek a quantity that is sensitive to the magnetic field orientation but insensitive to the dust temperature, dust to gas ratio, and other dust properties. In this section, we demonstrate that the polarization angle dispersion function $\mathcal{S}$ satisfies these criteria and robustly illustrates the sensitivity of $I_\nu/N_{\rm HI}$ to the angle ψ between the Galactic magnetic field and the line of sight.

As discussed in Section 3.1, $\mathcal{S}$ is a measure of the variability of the polarization angle χ in a given region of the sky. Because $\mathcal{S}$ is computed only from polarization angles, it is not sensitive to the dust column density and has no a priori dependence on dust temperature. Further, changes in χ are more easily induced when B is oriented along the line of sight than when B is in the plane of the sky. Thus, high

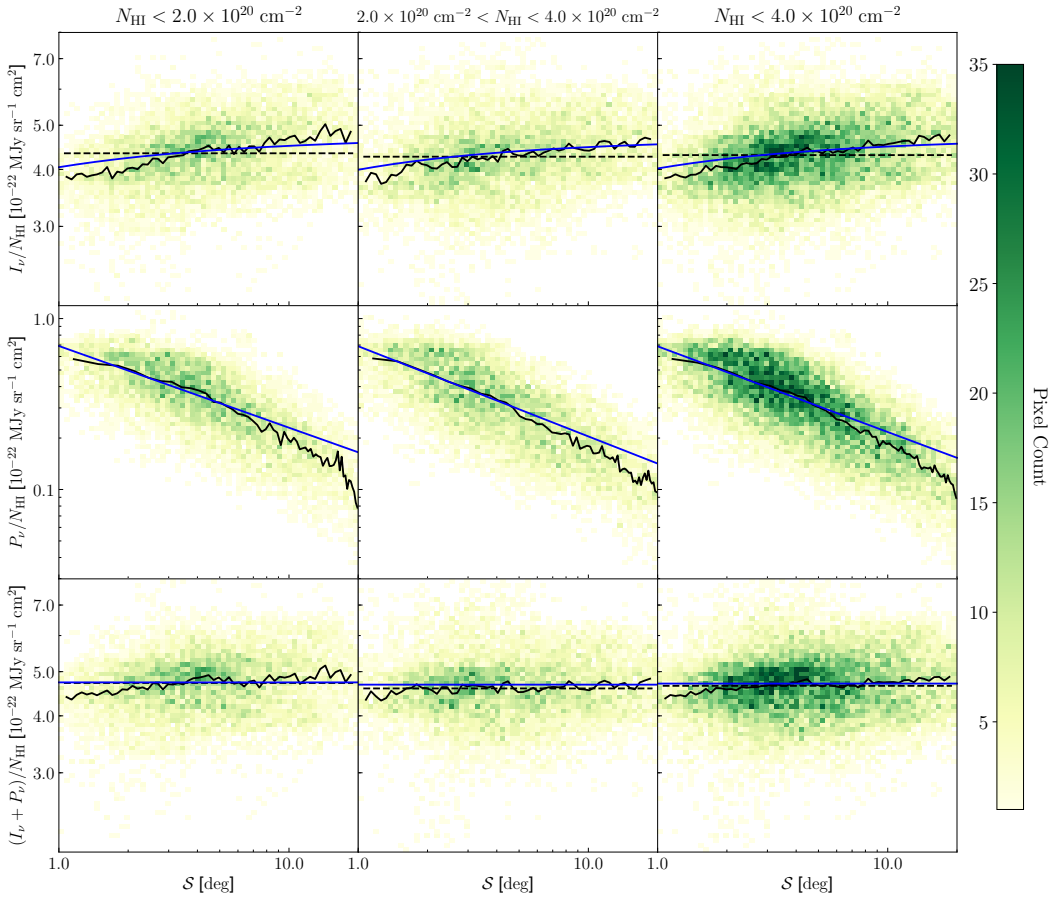

Figure 3.6: 2D histograms of $I_\nu/N_{\rm HI}$, $P_\nu/N_{\rm HI}$ and $\mathcal{S}$, with global means (black dashed) and running medians (black solid) plotted as in Figure 3.4. The columns correspond to different $N_{\rm HI}$ thresholds: $N_{\rm HI} < 2.0\times10^{20}\,cm^{-2}$ (left), $2.0\times10^{20}\,cm^{-2} < N_{\rm HI} < 4.0\times10^{20}\,cm^{-2}$ (middle), and $N_{\rm HI} < 4.0\times10^{20}\,cm^{-2}$ (right). The top row illustrates the robustness of the $I_\nu/N_{\rm HI}$–$\mathcal{S}$ correlation to column density. The middle row presents the strong anti-correlation between $P_\nu/N_{\rm HI}$ and $\mathcal{S}$, similar to what has been observed using the polarization fraction (Planck Collaboration XII, 2018). The bottom row demonstrates that summing $I_\nu/N_{\rm HI}$ and $P_\nu/N_{\rm HI}$ removes much of the correlation, as expected from Equation 3.14. The blue solid lines are the best joint fits to $I_\nu/N_{\rm HI}$, $P_\nu/N_{\rm HI}$, and $\mathcal{S}$ in each $N_{\rm HI}$ range. The best fit parameters are $A = 4.736 \pm 0.008$, 4.682 ± 0.009, and $(4.708 \pm 0.006) \times 10^{22}$ MJy sr^{-1} cm^2; $B = 0.691 \pm 0.005$, 0.689 ± 0.005, and $(0.688 \pm 0.003) \times 10^{22}$ MJy sr^{-1} cm^2; and $n = -0.478 \pm 0.005$, -0.528 ± 0.006, and -0.502 ± 0.004 in the left, middle, and right columns, respectively.

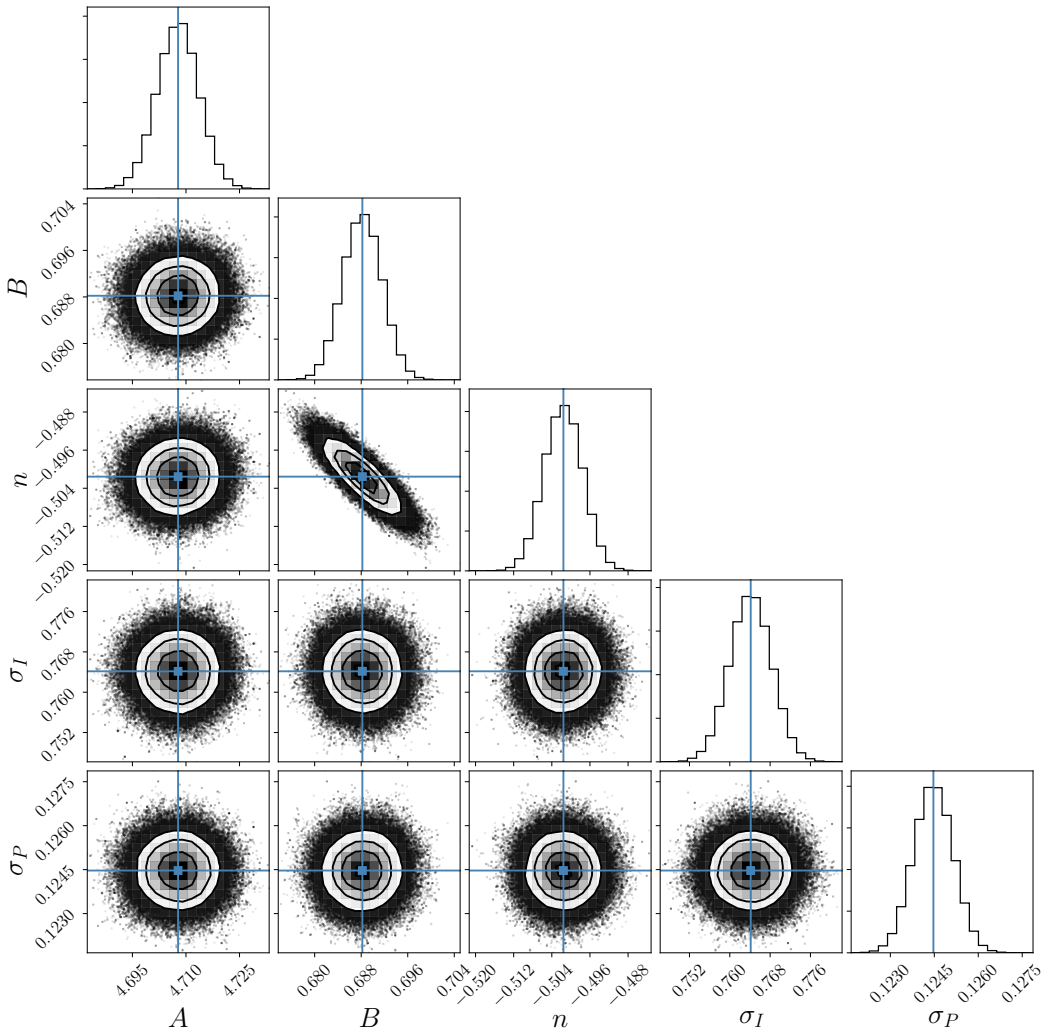

Figure 3.7: Posterior distributions of fit parameters after applying the fitting formalism of Section 3.3 to the $I_\nu/N_{\rm HI}$, $P_\nu/N_{\rm HI}$, and S data. The fit was restricted to pixels having $N_{\rm HI} < 4 \times 10^{20}\,{\rm cm}^{-2}$ and $1^\circ < \mathcal{S} < 20^\circ$. Best fit values are indicated with solid blue lines and are $A = (4.708 \pm 0.006) \times 10^{22}\,{\rm MJy\,sr^{-1}\,cm^2}$, $B = (0.688 \pm 0.003) \times 10^{22}\,{\rm MJy\,sr^{-1}\,cm^2}$, $n = -0.502 \pm 0.004$, $\sigma_I = (0.764 \pm 0.004) \times 10^{22}\,{\rm MJy\,sr^{-1}\,cm^2}$, and $\sigma_P = (0.124 \pm 0.001) \times 10^{22}\,{\rm MJy\,sr^{-1}\,cm^2}$.

$\mathcal{S}$ is expected when B is along the line of sight and low $\mathcal{S}$ when in the plane of the sky. We therefore expect $I_\nu/N_{\rm HI}$ to be positively correlated with $\mathcal{S}$.

In Figure 3.5, we present the correlation between $I_\nu/N_{\rm HI}$ and $\mathcal{S}$ over the diffuse high latitude sky ($N_{\rm HI} < 4 \times 10^{20}\,{\rm cm}^{-2}$). These quantities have a clear positive correlation (Spearman rank coefficient $\rho = 0.29$) despite considerable scatter.

It is worth emphasizing the remarkable nature of this correlation. $I_\nu/N_{\rm HI}$ is the ratio of density tracers having no polarization information. $\mathcal{S}$ is computed purely from polarization angles, which contain no information about the density field. It is difficult to explain their evident correlation in any way other than through the orientation of the Galactic magnetic field.

We present a more detailed test of the correlation in Figure 3.6. Each column in this figure corresponds to a different range of column densities, with the left column being $N_{\rm HI} < 2 \times 10^{20}\,{\rm cm}^{-2}$, the middle $2 \times 10^{20}\,{\rm cm}^{-2} < N_{\rm HI} < 4 \times 10^{20}\,{\rm cm}^{-2}$, and the right $N_{\rm HI} < 4 \times 10^{20}\,{\rm cm}^{-2}$. Thus, the first two columns are two independent sets of pixels on the sky. As in Figure 3.5, the top row presents the correlation of $\mathcal{S}$ with $I_\nu/N_{\rm HI}$. It is present at the same level in all three panels, demonstrating robustness to the range of $N_{\rm HI}$ considered.

The middle row of Figure 3.6 presents the correlation between $P_\nu/N_{\rm HI}$ and $\mathcal{S}$. Planck Collaboration XII (2018) demonstrated a clear anti-correlation between the polarization fraction p and $\mathcal{S}$, and so the strong (Spearman rank coefficient $\rho \simeq -0.7$) anti-correlation seen here is expected.

The bottom row of Figure 3.6 correlates $(I_\nu + P_\nu)/N_{\rm HI}$ and $\mathcal{S}$. If the simple model described in Section 3.1 holds, then the positive correlation between $I_\nu/N_{\rm HI}$ and $\mathcal{S}$ should precisely balance the negative correlation between $P_\nu/N_{\rm HI}$ and $\mathcal{S}$. Indeed, the correlation with $\mathcal{S}$ is greatly reduced (Spearman rank coefficient $\rho \simeq 0.1$), though some residual correlation remains.

Figure 3.6 demonstrates that $\mathcal{S}$ is a proxy for the angle ψ between B and the line of sight. If $\mathcal{S}$ were sensitive only to disorder in the magnetic field along the line of sight, then there would be no expected correlation with $I_\nu/N_{\rm HI}$. That this correlation exists and is of the same magnitude as the correlation with $P_\nu/N_{\rm HI}$ suggests that variation in ψ is the dominant driver of the empirical anti-correlation between $\mathcal{S}$ and both $P_\nu/N_{\rm HI}$ (this work) and the polarization fraction p (Planck Collaboration XII, 2018) across the high latitude sky.

Using the model presented in Equations 3.20 and 3.21, we can perform a joint fit

to the $I_\nu/N_{\rm HI}$, $P_\nu/N_{\rm HI}$, and $\mathcal{S}$ data. We fit for the model parameters A, B, and n as well as the intrinsic scatter σ_I and σ_P in $I_\nu/N_{\rm HI}$ and $P_\nu/N_{\rm HI}$, respectively, using the likelihood function in Equation 3.23. In addition to the column density threshold of $N_{\rm HI} < 4 \times 10^{20}\,{\rm cm}^{-2}$, we restrict the fit to pixels having $1^\circ < \mathcal{S} < 20^\circ$ where the relationship between the polarization fraction and $\mathcal{S}$ is observed to be linear (Planck Collaboration XII, 2018). The additional restriction on $\mathcal{S}$ reduces the usable sky fraction from 39% to 35%.

Over this sky area, corresponding to the right column of Figure 3.6, we find $A = (4.708 \pm 0.006) \times 10^{22}\,{\rm MJy\,sr^{-1}\,cm^2}$, $B = (0.688 \pm 0.003) \times 10^{22}\,{\rm MJy\,sr^{-1}\,cm^2}$, $n = -0.502 \pm 0.004$, $\sigma_I = (0.764 \pm 0.004) \times 10^{22}\,{\rm MJy\,sr^{-1}\,cm^2}$, and $\sigma_P = (0.124 \pm 0.001) \times 10^{22}\,{\rm MJy\,sr^{-1}\,cm^2}$. The posterior distributions for each of the fit parameters are presented in Figure 3.7. The overall fit to the data is quite good, reinforcing the fact that the observed variation in $I_\nu/N_{\rm HI}$ is of the magnitude expected from orientation effects given the the observed variations in $P_\nu/N_{\rm HI}$.

We find that $P_\nu/N_{\rm HI}$ scales approximately as $1/\sqrt{\mathcal{S}}$, somewhat shallower than the scaling of $p_\nu \propto S^{-0.67}$ found with BLASTPol observations in Vela C (Fissel et al., 2016) and significantly shallower than $p_\nu \propto S^{-1}$ found over the full sky with the same Planck 353 GHz data as we employ (Planck Collaboration XII, 2018). The $P_\nu/N_{\rm HI}$–$\mathcal{S}$ relation departs from a pure power law for $\mathcal{S} \gtrsim 10^\circ$. While the relation is expected to change character as $\mathcal{S}$ approaches the asymptotic value of $\pi/\sqrt{12} \simeq 52^\circ$ expected for uniform random variations in the polarization angles, that we observe this departure at smaller $\mathcal{S}$ than the full-sky Planck analysis may also point to spatial variability in the power law index n. As the relation is an empirical one depending on properties of MHD turbulence and the three-dimensional structure of the ISM (see discussion in Planck Collaboration XII, 2018), such variations are not unexpected.

Indeed, for the other column density cuts presented in Figure 3.6, we find slightly different values of our fit parameters. While B is consistent with $0.689 \times 10^{22}\,{\rm MJy\,sr^{-1}\,cm^2}$ in all $N_{\rm HI}$ ranges considered, n varies from -0.478 for $N_{\rm HI} < 2 \times 10^{20}\,{\rm cm}^{-2}$ to -0.528 for $N_{\rm HI}$ between 2 and $4 \times 10^{20}\,{\rm cm}^{-2}$ with fitting uncertainty of about 0.005. Likewise, A has best fit values of 4.736 and $4.682 \times 10^{22}\,{\rm MJy\,sr^{-1}\,cm^2}$ in the two column density ranges, respectively, with an uncertainty of $0.009 \times 10^{22}\,{\rm MJy\,sr^{-1}\,cm^2}$.

As evident from the bottom row of Figure 3.6, there remains residual correlation between $(I_\nu + P_\nu)/N_{\rm HI}$ and $\mathcal{S}$ that is not accounted for in the model. This could be attributed to a number of effects. First, the model considers only a single magnetic field orientation in a given pixel, both along the line of sight and within the beam.

Variations in the field orientation affect the total and polarized intensities differently, complicating the simple linear correlation. Second, there can be true correlations between $\mathcal{S}$ and dust properties in our Galaxy. For instance, if $\mathcal{S}$ depends in part on the properties of MHD turbulence, and if those properties are found preferentially in regions of high or low dust temperature or dust to gas ratio, then such residual correlations could emerge.

3.5 Discussion

We have demonstrated that the $\sim$ 10% variation in the dust emission per grain induced by orientation effects is detectable in the 353 GHz Planck data at a statistical level. Unlike the polarization angle which gives the projection of B onto the plane of the sky, this effect is sensitive only to the orientation of B relative to the line of sight, making it a complementary probe of the field orientation.

To progress from the statistical detection presented here to using this effect as a tracer of field orientation in specific sky regions, it will be necessary to improve the dust model fitting to extract reliable dust temperatures. Additional sensitive, high-frequency data, such as that provided by a mission like the Probe of Inflation and Cosmic Origins (PICO, Hanany et al., 2019), would greatly improve existing SED fitting. In particular, high frequency polarization data is minimally contaminated by the CIB and thus may be more effective in constraining dust model parameters such as T_d than the total intensity data.

In the nearer term, incorporation of HI data into component separation, as has been demonstrated in CIB studies (Planck Collaboration XXX, 2014; Lenz, Doré, and Lagache, 2019) and is being explored in the context of CMB foregrounds (Zhang et al., 2019), has considerable potential for improving the fidelity of dust model fits. Further, such HI-based model fits could explicitly account for the effect of viewing angle in the data model.

Beyond improving determination of the dust temperature and other dust model parameters, HI emission itself is a powerful tracer of the Galactic magnetic field. Linear filamentary structures seen in HI emission have been shown to align strongly with the local magnetic field (Clark et al., 2015), allowing the magnetic field orientation to be traced both as a function of position on the sky as well as HI velocity (Clark & Hensley, in prep.). A synthesis of far-infrared and HI emission could therefore in principle enable mapping of the full three-dimensional orientation of the Galactic magnetic field over the sky. With existing stellar distances from Gaia

(Gaia Collaboration et al., 2016) and upcoming starlight polarization measurements from PASIPHAE (Tassis et al., 2018), such Galactic magnetic field models could be translated from magnetic field orientations in HI velocity-space to the full distribution of dust and magnetic field orientations in the three spatial dimensions.

The line of sight component of the Galactic magnetic field can be constrained in ways other than the one presented here. For instance, the dust polarization fraction p_ν is sensitive to the inclination of B (see Equation 3.12), but is complicated by non-uniformity in the magnetic field orientation along the line of sight (Clark, 2018). Joint modeling of p_ν and $I_\nu/N_{\rm HI}$ can help overcome the different limitations of each diagnostic and therefore also quantitatively distinguish between the effects of magnetic field orientation and beam/line-of-sight depolarization. Additionally, Faraday rotation and Zeeman splitting have both been used to measure the line of sight component of B, though they may preferentially probe different ISM phases than dust-based tracers.

Dust emission in total intensity and polarization are tightly coupled in ways straightforwardly captured in parametric models, as described in Section 3.1. As the quest for the detection of primordial B-modes in the polarized CMB pushes to ever-increasing precision, the importance of accurate modeling and subtraction of dust foregrounds is paramount (see discussion in BICEP/Keck Collaboration et al., 2018). Effects like the one discussed in this work enable other datasets, such as dust intensity and HI emission, to be brought to bear on modeling dust polarization. Even if not accounted for explicitly, this effect can validate dust temperatures and dust column densities that emerge from model fitting. As we are pushed to higher fidelity modeling of dust foregrounds, we should at the same time be learning about the structure of the magnetized ISM in increasing detail.

3.6 Conclusions

The principal conclusions of this work are as follows:

1. Because dust grains are aspherical, the effective cross section and thus total emission from dust depends on the viewing angle. We demonstrate that this induces a direct anti-correlation between the total dust intensity per $N_{\rm HI}$ and the polarized dust intensity per $N_{\rm HI}$ (Equation 3.14).

2. In the low column density sky ($N_{\rm HI} < 4\times10^{20}\,{\rm cm}^{-2}$), we find that application the GNILC dust temperature map does not improve the correlation between the

353 GHz dust intensity and the HI column density as expected. We suggest this arises from parameter degeneracies in the low signal to noise regime. The tests outlined in Section 3.3 can provide a means of validating future dust temperature maps.

3. We find a robust positive correlation between $I_\nu/N_{\rm HI}$ and the polarization angle dispersion function $\mathcal{S}$ as predicted from the orientation effect. This suggests that observed variations in $\mathcal{S}$ are driven largely by the variations in the angle between the Galactic magnetic field and the line of sight.

4. We find that the positive correlation between $I_\nu/N_{\rm HI}$ and $\mathcal{S}$ is largely compensated by the anti-correlation between $P_\nu/N_{\rm HI}$ and $\mathcal{S}$, as predicted by Equation 3.14.

5. We argue that the variation in dust emission per $N_{\rm HI}$ can be used to probe the full 3D magnetic field orientation vector, complementing the plane of sky orientation provided by the dust polarization angle.

6. We suggest this effect can also be exploited in component separation in CMB experiments, particularly since the formalism developed in Section 3.1 provides a physically-motivated means of connecting observations of total intensity and polarization.

Chapter 4

THE BICEP ARRAY EXPERIMENT AND INSTRUMENT OVERVIEW

4.1 The BICEP/*Keck* Experiments

The BICEP/*Keck* (BK) Experiments are a series of experiments measuring primordial B-mode in the CMB polarization with degree-scale telescopes. All BK telescopes share a similar design and observing strategy, aggressively targeting the bump around $l = 100$ (about two degrees on the sky) in the B-mode spectrum by making deep maps of a relatively small patch of sky. Table 4.1 lists all the BK experiments with their frequency bands and year of operation. The interested reader is referred to the following references for more information on the former experiments: (Tolan, 2014; Teply, 2015; Karkare, 2017) for BICEP2 and *Keck* Array, (Wu, 2015; Grayson, 2016; Hui, 2018; Kang, 2020; Yang, 2021) for BICEP3, and (Crumrine, 2022; Palladino, 2021) for BICEP Array. In the rest of this Chapter, I will talk about the observing site and the experimental strategy.

Experiment	Band (GHz)	Year of Operation
BICEP1	100 / 150	2005-2009
BICEP2	150	2009-2012
Keck Array	95	2014-2015
	150	2012-2016
	220	2015-present[1]
	270	2017-present
BICEP3	95	2015-present
BICEP Array	30 / 40	2019-present
	150	2022
	95	2023
	220 / 270	2023

Table 4.1: Table of all the BK experiments, frequency bands, and the year of operation.

[1] *Keck* Array stopped mission at the end of 2019. Three *Keck* receivers, two at 220 GHz and one at 270 GHz, have been put into the new BICEP Array mount running along with the first BICEP Array receiver.

Observing Site

The BK experiments are based at the Amundsen-Scott South Pole Station. The station has supported ground-based microwave observations for the past three decades. Owing to the National Science Foundation's support, operations at the South Pole are logistically simple. Lodging, power, heat, meals, transportation, and shipping are all taken care of by the Antarctic Support Contract (ASC), which supports the day-to-day needs of the station. Also available are: an on-site machine shop, a woodshop, and a large stock of scientific equipment and supplies. BICEP1 (2005-2009), BICEP2 (2009-2012), and BICEP3(2015-present) are located in the Dark Sector Laboratory (DSL). *Keck* Array (2011-2019) and BICEP Array (2019-present) are located in the Martin A. Pomerantz Observatory (MAPO). Both sites are about 1 kilometer from the main station building.

The South Pole station is at 2,835 meters (9,306 feet). The atmosphere is extremely cold and dry, thus proving excellent transparency at millimeter wavelength (Lane, 1998). There is only one sunrise-to-sunset cycle a year at the South Pole, which proves stable weather conditions, especially in the water vapor fluctuations. Figure 4.1 shows the median atmospheric transmission during the winter season in black bracketed by the 10th and 90th percentiles, overlaid with the frequency bandpasses of the BK experiments. The effect of water vapor fluctuations is almost negligible at low-frequency bands while remaining at an acceptable level at the high frequencies.

Because the station sits right on the Earth's rotation axis, the sky rotates around the zenith without any shift in elevation. Thus the targeted sky patch is visible to the telescope all year round, allowing long continuous observing season and long integration times, which is essential for measuring the faint polarization signals.

Observing Strategy

The main idea of BK experiments' observing strategy is making deep polarization maps of a small sky patch, about 1% of the full sky, which is large enough for the modes in interest. The map depth goes down as the square root of the covered sky area, making the current strategy suitable for an initial detection. The mapping area is 400 $\deg^2$ for *Keck* Array, and has been enlarged to 600 $\deg^2$ for BICEP3 because of its larger field of view. BICEP Array inherited the extended sky patch from BICEP3.

Unlike the CMB, foregrounds vary a lot over the sky. The BK sky patch is chosen to be a low-foreground area centered at RA = 0h, Dec = 57.5°, within a region known as the "Southern Hole". Figure 4.2 shows the sky patch on the map of dust

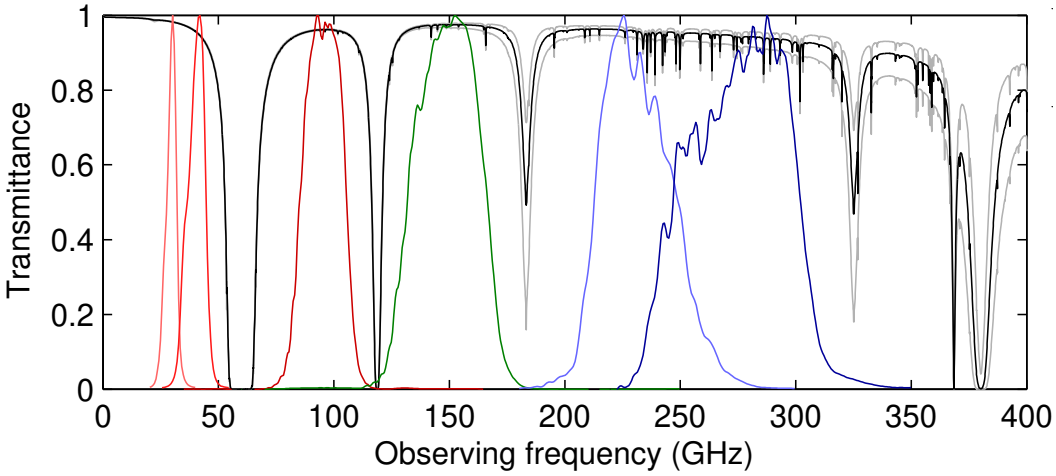

Figure 4.1: Atmospheric transmission at the South Pole and the bandpasses of existing BICEP/*Keck* receivers. Median atmospheric transmission during the winter season is shown in black, bracketed by the 10th and 90th percentiles.

emission. BICEP Array observes the same sky patch as BICEP3 for CMB, covering $-60° < \text{R.A.} < 60°$ and $-70° < \text{decl.} < -40°$, with an effective sky area of ~ 600 deg^2. About 15% of the observing time is targeting a separate field mapping a part of the Galactic plane, centered at R.A. = 15 : 42 hr, decl. = $-53°$.

BICEP Array scans the targeted fields continuously through the austral winter. The fundamental observing block is called "scanset", consisting of 48 back-and-forth scans in azimuth at a constant elevation over 50 minutes. The scan is at a speed of $2.8°$ s^{-1}, spanning $64.4°$. The scan center is shifted by $25°$ in azimuth every other scanset to track the change in R.A. due to the earth's rotation. The azimuth-fixed scan pattern enables us to develop templates at an hour time scale for subtracting ground-fixed signal. The elevation is stepped every other scanset by $0.25°$ to fill in coverage between the spatially separated detector beams.

Detector load curves and elevation nods are taken before and after each scanset for calibration purposes. The load curves scan the TES bias current from high to low and measure the detector current to power responsivity for temporal gain calibration. The elevation nod is usually abbreviated as "elnod", which is a quick elevation motion by $1.6°$. The current response to the elnod can be fit linearly to the airmass varies as the cosecant of the elevation angle. The elnod can provide immediate gain calibration over each band. We take load curves and elnods at the beginning and end of each scanset to ensure the stability of the gain through the observation.

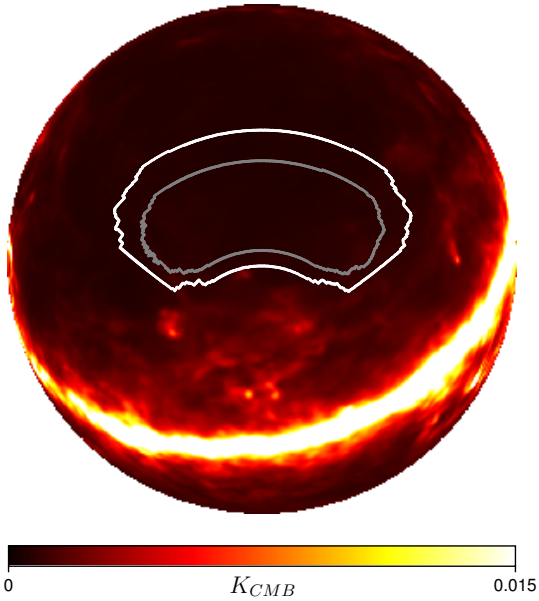

Figure 4.2: The BK sky patch plotted against the Planck 2018 GNILC dust intensity map at 353 GHz. The grey line shows the 400 deg^2 area mapped by *Keck* Array. The white line shows the extended 600 deg^2 area mapped by BICEP3 and BICEP Array.

BICEP Array has adapted the 2-day observation schedule from *Keck* Array. The scansets are grouped into "phases", each has 7 or 10 scansets along with the accompanying calibrations. During the 2-day schedule, the telescopes complete one cryogenic cycle, four 10-hour phases on the CMB field, and one 7-hour phase on the Galactic plane. The whole telescope mount rotates about the boresight of the array after each 2-day schedule for polarization measurement. A total of eight boresight angles at 23°, 68°, 113°, 158°, 203°, 248°, 293°, and 338° are used.

The BICEP Array receiver can hold at desired base temperature for three days or longer. The current 2-day schedule is a compromise for the *Keck* receivers running along. The schedule may be extended when more BA receivers are deployed for observation.

Design Strategy

The BK telescopes are on-axis refractors with small apertures. The angular resolutions are at the sub-degree level. This design is optimized for detecting the degree-scale patterns and is compact enough to allow cold optics for low instrument loading. The on-axis design allows deck rotations around the telescope boresight,

modulating the polarization angles of the detectors, and enables cancellations of beam systematics(P. A. R. Ade, R. W. Aikin, et al., 2015).

The BK experiments build telescopes at different frequency bands within the atmosphere window constraints, as shown in Figure 4.1. Deep mapping at multiple frequencies is the key to foreground component separation. *Keck* Array added 95, 220, and 270 GHz bands in 2014, 2015, and 2016. In the latest BK18 results (P. A. R. Ade, Z. Ahmed, Amiri, et al., 2021), the constraint power from *Keck* 220 is equivalent to that from Planck 353 GHz, which means BK now can independently constrain dust without priors derived from other sky areas. BICEP3 is a stage-3 CMB telescope that started observation at 95 GHz in 2016. Three years of BICEP3 data has achieved the same map depth as all the 150 GHz data accumulated over the past decade. BICEP Array will have four BICEP3 class receivers at all existing frequency bands and new bands at 30/40 GHz for constraining synchrotron. Figure 4.3 shows the progression of the BK instruments.

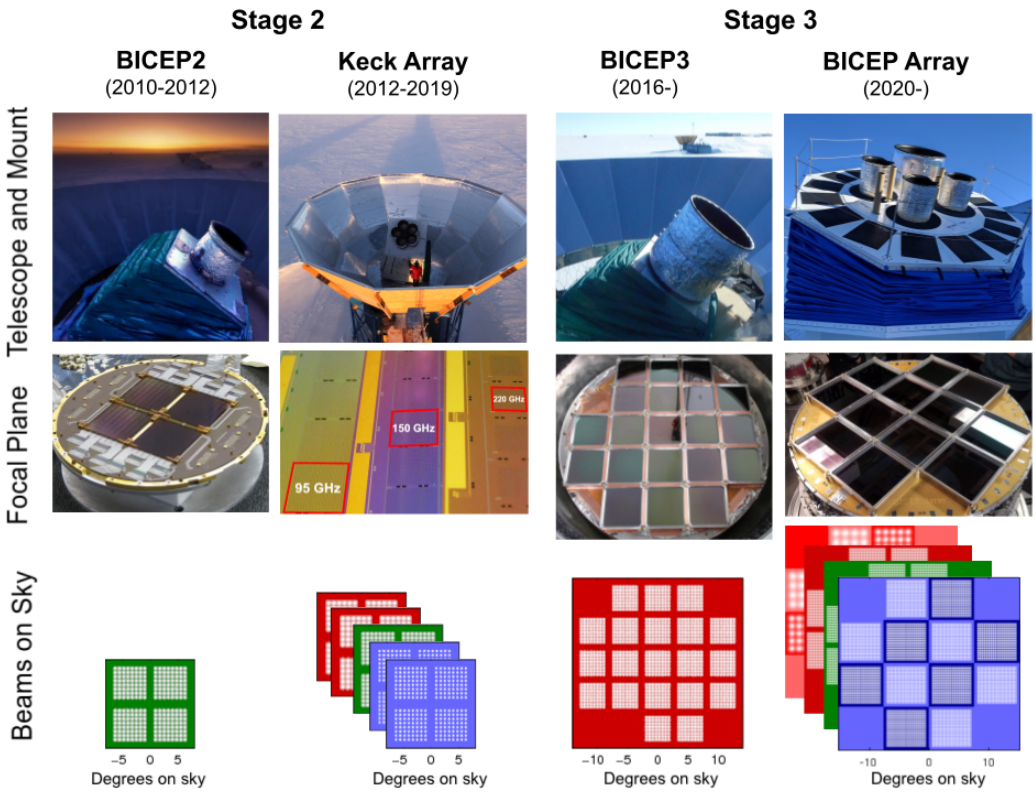

Figure 4.3: The progression of the BICEP/*Keck* instruments. The relative sizes of the instruments as installed at the South Pole and their focal planes can be seen in the first two rows. The final row depicts detector beams as projected on the sky with colors denoting the frequency coverage of the arrays. Figure from the BICEP/*Keck* collaboration.

4.2 BICEP Array

BICEP Array is the latest generation of the BK experiments. In the final configuration, it has four BICEP3-class telescopes spanning six frequency bands, with an ultimate sensitivity to the amplitude of the primordial gravitational wave of $\sigma(r) \lesssim 0.003$ (Hui et al., 2018).

The first BICEP Array receiver is at 30/40 GHz for synchrotron foreground. It was deployed to the South Pole around the end of 2019 along with the new telescope mount. The rest three receivers are planned to be deployed in 2022-2023. Table 4.2 shows the proposed detector counts and sensitivities.

Receiver Observing Band (GHz)	Number of Detectors	Single Detector NET ($\mu K\sqrt{s}$)	Beam FWHM (arcmin)	Survey Weight ($\mu K^{-2} yr$)
Keck Array				
95	288	288	43	24,000
150	**512**	313	**30**	**25,700**
220	**512**	837	**21**	**3,500**
270	512	1,310	17	300
BICEP3				
95	**2,560**	288	**24**	**211,000**
BICEP Array				
30	192	260	76	19,400
40	300	318	57	20,300
95	4,056	288	24	334,000
150	7,776	313	15	390,000
220	8,112	837	11	55,500
270	12,288	1,310	9	34,300

Table 4.2: The proposed detector counts and sensitivity of BICEP Array. The achieved numbers for the past experiments are also listed in the table. The boldface numbers are actual/achieved quantities which we scale from. The BICEP Array values in the survey weight column are scaled from the achieved values using only the ratio of the number of detectors, plus, if necessary to change frequency, the ratio of nominal NET values squared.

4.3 The BICEP Array receiver

Cryogenic, optics, and baffling

The cryostat structure of the BICEP Array builds on the success and heritage of the previous BICEP/*Keck* instruments. The cryostat is mainly composed of a series of co-axial shells, as shown in Figure 4.4. The out-most shell is the vacuum jacket at the ambient temperature. The two inner layers are cooled down to 4K and 50K by

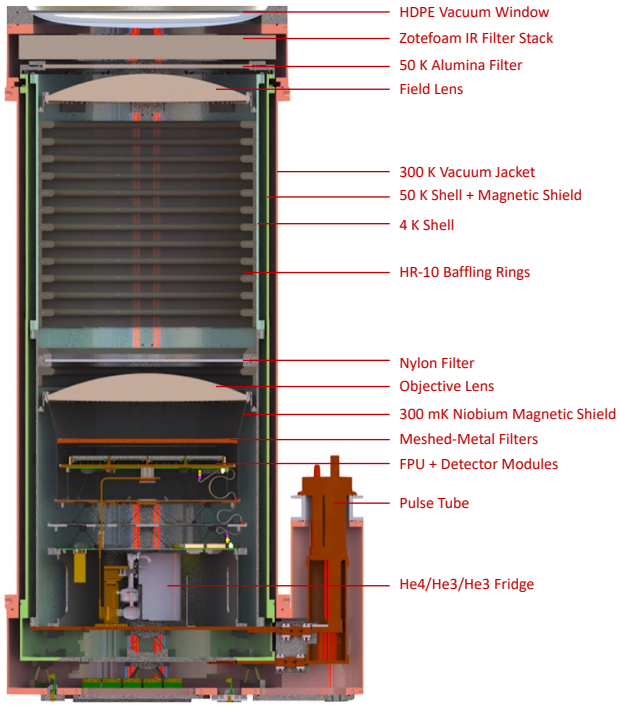

Figure 4.4: A rendered cross section of the 30/40 GHz BICEP Array receiver deployed during the 2019-2020 austral summer.

the Cryomech PT415 cryocooler [2]. The outer 50K shell is covered with one high-μ sheet for magnetic shielding and 30 layers of MLI to reduce radiation absorption. The 4K shell is also covered by 5 layers of MLI externally for the same purpose. The top side of the receiver is enclosed by an "extension piece", which provides mounting surfaces for the HDPE vacuum window and a stack of twelve layers of high-density polyethylene (HD30) absorptive foam filters blocking unwanted IR. An alumina filter is anti-reflection coated and mounted at the top of the 50 K cylinder. The bottom side is bucket-like structures with openable hatches supporting the upper structures and providing attachment points for the readout electronics. The whole 50 K radiation shield (bucket+shell) is held by six low-conductivity G10 fiberglass legs from the bottom. Six thin titanium strips maintain the concentricity of the shells from the top. The Pulse Tube cold head is mounted outside the main cylinder in a structure usually referred to as "doghouse".

Our telecentric refractive optics design consists of a pair of HDPE lenses with a clear aperture of 550 mm at 4K. The f#s from ZEMAX simulation are 1.57 at the center of the FPU, 1.72 at the worst sagittal, and 2.04 at the worst tangential. Figure

[2]https://www.cryomech.com/products/pt415/

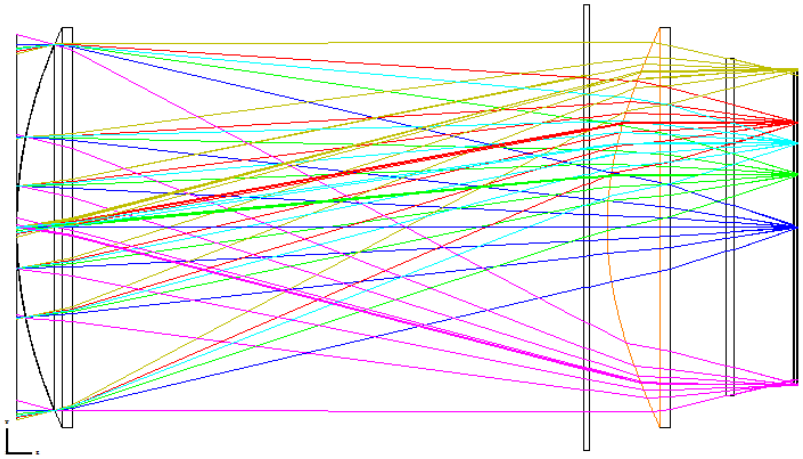

Figure 4.5: ZEMAX ray-tracing of the BICEP Array optics model for the 30/40 GHz receiver.

4.5 shows the optics stack and the ray-tracing diagram. A Nylon IR filter is mounted between the two lenses. All optics elements are cooled down to 4K for less detector loading from instruments. The inner surface of the 4K optics tube is covered by HR-10 baffling rings to intercept unwanted reflections.

An extended piece called "forebaffle" is attached above the cryostat window and comoves with the receiver during observations, blocking side-lobe rays, ground-sourced rays which may reflect from the lip of the external ground shield, and RFI from base communications. The very top of the receiver hosts a thin membrane of Bi-axially Oriented Polypropylene (BOPP) pressurized into a tightly stretched dome by a feed of room temperature dry nitrogen, preventing snow and ice from accumulating on the vacuum window inside the forebaffle.

Sub-Kelvin camera

The bottom part of Figure 4.4 shows the sub-K camera. The structure is tower-like, with the coldest stage on the top. The supporting legs are made of low conductivity carbon fiber trusses whose mechanical strength has been carefully simulated and tested.

Detectors of BICEP Array require an operating temperature at around 300 mK, which is realized by a three-stage ^{4}He/^{3}He/^{3}He sorption fridge, as shown in Figure 4.6. ^{4}He is condensed into the evaporating cylinder by the 4K stage of the cryostat. The pump is activated charcoal which can absorb He molecules and keep the pressure low in the still. The ^{3}He stages work in a similar way as the ^{4}He, except they use the

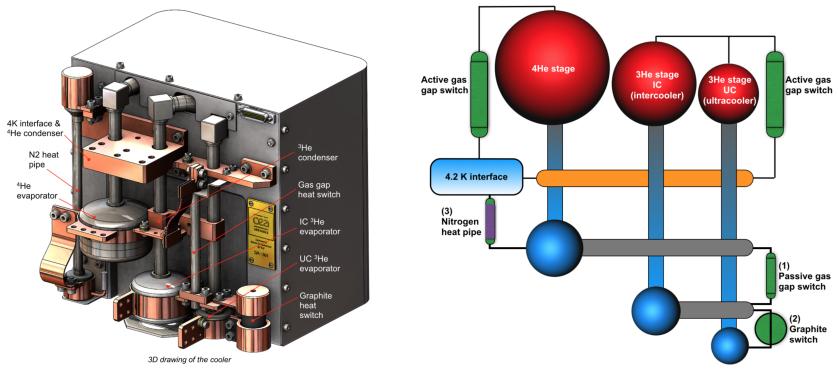

Figure 4.6: Schematics and rendered figure of the sub-Kelvin sorption fridge.

previous stages for condensing. The fridge requires cycling after the liquid "runs out", during which we heat up the charcoal pump to release all the molecules and condense them back into the evaporator. The three evaporators of the fridge are connected to the 2K plate, the intercooler (IC) plate, and the ultracooler (UC) plate in the sub-K system through Cu heat straps. Progressive stacking of the colder tiers provides conduction insulation for the coldest stage and progressive heat sinking for the readout cabling at each tier. The IC stage additionally provides a mounting ring for a superconducting niobium plate to dampen axial magnetic fields and a niobium spittoon which extends above the focal plane to dampen radial magnetic fields. The UC stage hosts the gold-plated OFHC focal plane to which the detector modules are mounted. Each BICEP Array focal plane can host twelve 6-inch detector modules.

Detector module

Figure 4.7 shows the design of the BA 6-inch detector module. The plot is up-side-down, with the bottom facing the sky when once mounted in the receiver. The module is a niobium box with detectors and SQUIDs inside in a layered structure. An aluminum frame with corrugation patterns holds the inner elements from the sky side. The corrugation patterns are specially designed to minimize the edge effect for the edge pixels (Soliman et al., 2018). The detector wafer is with the fabricated patterns facing away from the sky. This is because the antenna receiver power better through the silicon subtract than the vacuum (P. A. R. Ade, R. W. Aikin, et al., 2015). A $\lambda/4$ superconducting niobium back-short is placed on the vacuum side of the antenna to terminate the back response. We mount $\lambda/4$ quartz anti-reflection (AR) tiles to minimize reflection at the air-substrate surface. An additional layer of A4K is placed behind the back-short.

The SQUIDs and Nyquist chips are glued on the circuit board located after the A4K

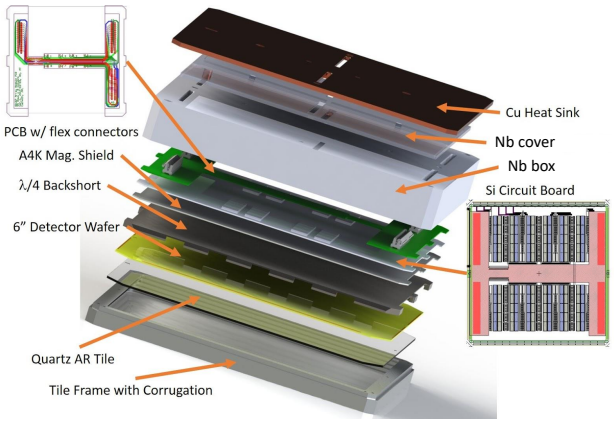

Figure 4.7: An exploded view of the BA module design.

sheet. The superconducting niobium case and back-short, together with the A4K sheet, provide ultimate magnetic shielding for the SQUIDs. The circuit board is made in alumina for BA1 while in FR-4 for BA2 and future receivers. An H-shape PCB routes out the readout lines through a few flexible flat cables through slots on the backside of the niobium box. An additional niobium plate offset the slots and enhanced the magnetic shielding. Finally a Cu plate is mounted at the bottom of the module for heat sink.

Readout

As discussed in Chapter 5, we use Transition Edge Sensors (TES) as our detectors and apply constant voltage bias for continuous operation at the high responsivity transition edge. We use a SQUID-based time-domain multiplexing architecture to measure the small current change in the TES array.

The superconducting quantum interference device SQUID consists of two Josephson junctions in parallel in a superconducting loop. SQUIDs are very sensitive to the magnetic field. A typical DC SQUID has a periodic sine wave-like $V - \phi$ curve when biased above two times the critical current I_0. In this case, the SQUID can be a current amplifier by coupling to the magnetic field generated by the current. If biased between I_0 and $2I_0$, the SQUID is "half-on", which means the voltage across the SQUID only appears for a specific range of ϕ and remains zero otherwise. The $V - \phi$ curve of a half-on SQUID is like a bottomed-out sine wave. The SQUID in half-on mode can be used as a flux switch.

Figure 4.8 shows the schematics of our time-domain multiplexing readout. Each detector is coupled to a first stage SQUID (SQ1) through the SQ1 input coil. All

SQ1s in the same readout column share one bias line, but whether a SQ1 is biased or not depends on the state of the row-select SQUID (RS). RS is parallel to the SQ1 and biased in its half-on state. With the proper amount of flux applied, the RS can be turned on and activate the SQ1 for sampling the TES current. Panels at the top-right corner of Figure 4.8 show $V - \phi$ curves of SQ1 and RS. The fact that SQ1 and RS share the same bias line requires RS to have larger critical current than SQ1. By turning on the RSs sequently, we can readout detectors in a common column one by one. When a RS is on, the corresponding SQ1 can sample on TES current, and the signal is amplified by a column-shared SQUID series array (SSA). SSA is sampling at 50MHz. The resulted adc readout is accumulated through each frame and used in SQ1 feedback calculation through a PID servo. The SQ1 feedback cancels out the effect from TES current and locks the SQ1 at its linear responding point. SSA is biased at its maximum peak-to-peak $V - \phi$ amplitude and is operated at its linear responding point with the SA feedback line. SQ1 and RS are located inside the detector module, while SSA modules are on the 4K stage, packaged in Niobium boxes, and additionally wrapped with 10 layers of high-μ Metglas 2714A.

Control of the multiplexing system and the feedback-based readout of the TES data is via the room temperature Multi-Channel Electronics (MCE) systems developed by UBC. The first 30/40 GHz receiver of BICEP Array has 24 readout columns, each with 33 rows. The raw sampling rate of the system is 50 MHz. The number of clock cycle spent at each row is specified by the parameter "row_len", which is set to be 120 in BA1. As a result, the row-revisit rate is 50 MHz/33 rows/120 $\simeq$ 12 kHz. We have verified that the ~6 kHz Nyquist frequency is high enough to avoid large aliasing penalty in BA1 detectors. The data is then low-pass filtered by a 4-pole Butterworth digital filter cut-off at about 60 Hz to suppress high frequency noise before decimated according to an external syncbox which triggers at 200 Hz. The Linux General Control Program (GCP) applies an acausal Finite Impulse Response (FIR) filter and further downsamples the data by a factor of 9 for a final on-disk sample rate of 22.22 Hz.

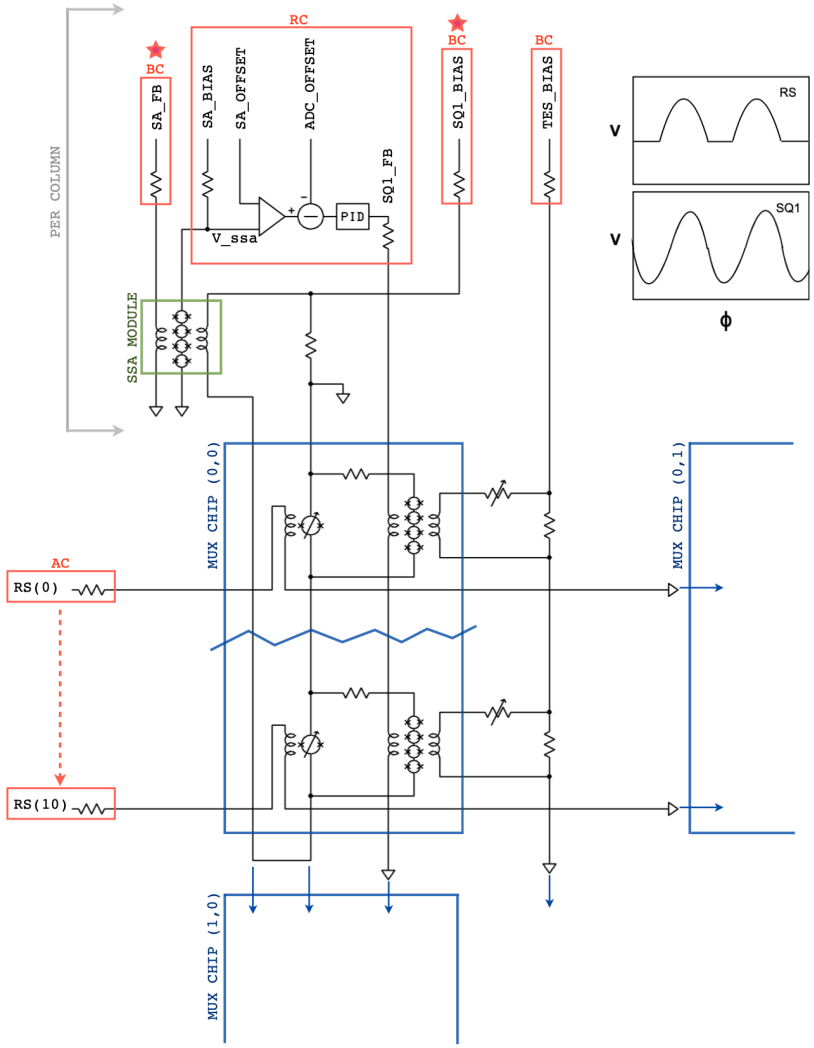

Figure 4.8: Schematic of the BA MUX11d SQUID-based time-domain multiplexing. Plot adapted from an earlier version by Jimmy Grayson.

Chapter 5

ANTENNA-COUPLED TRANSITION EDGE SENSOR FOR 30/40 GHZ

BA1 uses antenna-coupled Transition Edge Sensor (TES) detectors. Each detector element (pixel) has two sets of co-located, orthogonally polarized planar antenna arrays, each composed of slot sub-radiators patterned in the superconducting niobium (Nb) ground plane. The optical power collected by each polarized array is coherently summed, band-passed by a third-order Chebyshev filter, and fed to a TES bolometer. Figure 5.1 shows the path of photons. The design conventions of the planar antenna-coupled detectors can be found in (P. A. R. Ade, R. W. Aikin, et al., 2015). In this and the next chapters, I discussed optimizations for 30/40 GHz bands and showed the results of detector characterizations.

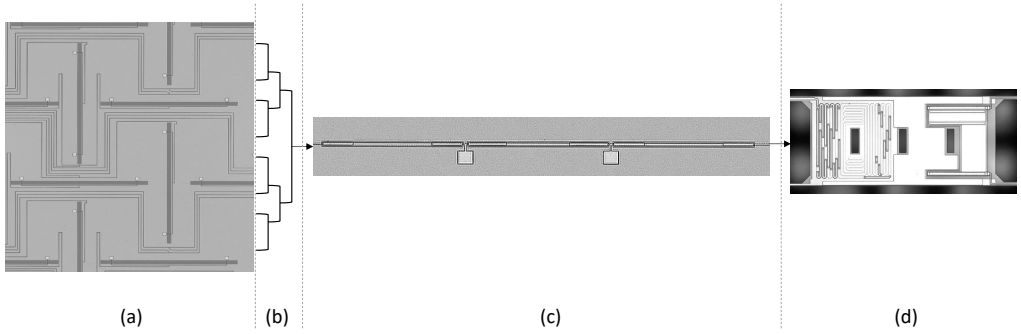

Figure 5.1: The photon path through a BA detector. (a) Two co-located slot antenna arrays collect optical power from polarized radiation. (b) The optical power from antenna slots is coherently summed by the microstrip summing tree (c) and sent to a third-order Chebyshev band-pass filter. (d) The in-band power is deposited on the thermal isolated TES island through the gold meander resistor.

5.1 Antenna

We use the slot antenna for its highly polarized radiation pattern. The slots are patterned on the Niobium ground plane in the Bravais lattice fashion. The two polarizations are co-located to minimize the differential pointing, as shown in Figure 5.1 (a). The dimension of the individual slot decides the band center of the antenna, while the size of the slot array controls the beam coupling to the aperture. Both 30 and 40 GHz have 8-by-8 slots array, with a side length 21.6 and 17.9 mm respectively.

The slots are uniformly illuminated, which gives a sinc radiation pattern in the far-field. The size of the pixel roughly follows the 2f#λ rules, which put the aperture near the first minimum in the radiation pattern. This design optimizes the spillover efficiency of the detector while terminates the side-lobes at the cold aperture. The 40 GHz slot antenna array is directly scaled from the deployed BICEP3 95 GHz design by the ratio of wavelengths. The slot size for 30 GHz is also directly scaled from the higher frequency design, while the packing at 30 GHz is slightly tighter to shrink the pixel size and fit a 4-by-4 pixel array on the 6 inches silicon wafer. Antenna designs for both 30 and 40 GHz are verified with EM simulations.

5.2 Microstrip summing tree

The microstrip summing network coherently sums the power from all slots in each polarization, see Figure 5.1 (a) and (b). The microstrip line consists of 170 nm thick Nb ground plane, 270 nm silicon dioxide ILD, and 400 nm thick Nb transmission layer. Impedance of the microstrip line with a certain width can be calculated using equations from (Hammerstad and Jensen, 1980) at the frequency of interest with simple extension to include the extra inductance of superconducting transmission line. The calculated impedance has been verified with Sonnet simulations. Impedance has to be matched at antenna feeding ports and all the branching junctions in the network to insure optimized efficiency. Junctions in the network are impedance-matched when looking from the port closest to the bolometer, with the power splits proportional to the number of slots on each side. This produces a top-hat illumination and a sinc pattern in the far-field as discussed in Section 5.1.

5.3 Measurement of the loss tangent in superconducting $Nb/Si0_2/Nb$ microstrip

The loss of the transmission line is a major concern in pixel design in consideration of the detector's optical efficiency. We use $Nb/Si0_2/Nb$ microstrip in the summing network as described above. The superconductor loss is supposed to be small or negligible as the frequencies we care about are comfortably below the Nb gap frequency ($\sim$ 700 GHz). Thus, the microstrip loss is dominated by the loss tangent of the amorphous SiO_2 dielectric layer, which is usually independent to frequency. This keeps the total loss from the microstrip line at about the same level for pixels at different frequency bands as the pixel size grows roughly proportional to the wavelength. However, if imperfections in the superconductor layers add in non-negligible loss due to the finite metal conductivity, the total loss could get worse in

lower frequency pixels. Therefore, a measurement of the microstrip loss is important for low-frequency design and informative for future mm/sub-mm applications.

We measured the loss of the microstrip line with loss devices as shown in Figure 5.2. The loss device is a modification from the real 270 GHz Keck pixel. Instead of having each slot antenna array readout by one TES bolometer, the power from one polarization is divided into two equal parts and fed to two TESs, while the other polarization is left unconnected. In each pixel, lengths of the microstrip lines between the split junction and TES islands are different by ΔL. The microstrip consists of a 170 nm thick Nb ground plane, 270 nm silicon dioxide ILD, and 400 nm thick Nb transmission layer, the same as in the real BK detectors. The width of the top Nb conductor is about 3.7μm. The TES bolometers measure the transmitted power at the end of the microstrip lines. By comparing power reaching the two bolometers, we can estimate the loss in a microstrip line with length ΔL.

Another thing to note is that, unlike normal pixels, there is no on-chip band-pass filter (Section 5.4) in the loss devices. This allows the loss measurement to be performed over the whole frequency range defined by the antenna response, extended from 130 GHz to 330 GHz.

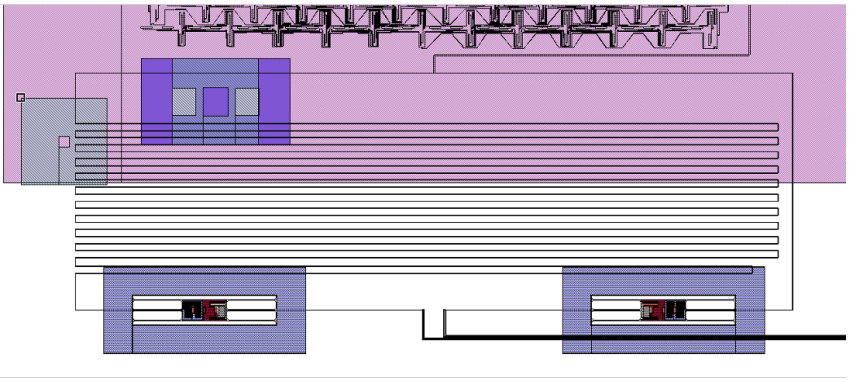

Figure 5.2: Loss devices have the power from a single polarized antenna array divided into two equal parts and fed to two TES bolometers. The length of microstrip branches after the power splitting junction is different.

We made two 4-inch wafers for the loss measurement, each containing an 8-by-8 pixel array. The 64 pixels in each wafer is evenly assigned to four different types of loss device, named 'a', 'b', 'c', 'd', with ΔL = 2.9, 3.8, 5.8, 11.8 cm respectively. Figure 5.3 shows the physical distribution of the four types in a wafer. The semi-uniform pattern of the loss device allows us to sample on both the edge and central area of the wafer, even out any systematic introduced from fabrication uniformity.

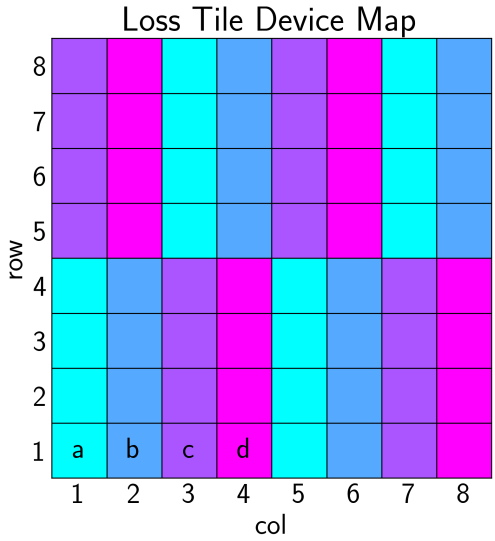

Figure 5.3: A tile map shows the distribution of the four loss types in a 4-inch wafer.

The test was done in a modified Keck receiver with an HDPE window and no optics. The detectors were cooled down to around 360 mK during measurement. The detectors' optical efficiencies and spectra are measured as described in Section 6.2 and 6.3, with a thermal source at liquid nitrogen temperature. The measured spectra are calibrated into the unitless end-to-end optical efficiency with Eq. 6.4 and the measured $\mathrm{d}P/\mathrm{d}T$. The power attenuation at the end of a transmission line with length z is described as

$$P(z) = P_0 \mathrm{e}^{-2\alpha z} \,, \tag{5.1}$$

where P_0 and $P(z)$ are the input and output power at the two ends of the transmission line. In our setup, P_0 is the power measured by the bolometer on the shorter branch, while $P(z)$ is the power measured on the longer branch. $z = \Delta L$. We do not care much about the absolute power reaching the bolometers as the ratio is what matters. Figure 5.4 shows an example of measured spectra from a loss device in its top panel and their ratio in the middle panel. The attenuation derived from Eq. 5.1 is shown in the bottom panel.

We report on the loss tangent of the microstrip line. Assuming the attenuation is dominated by the dielectric, the loss tangent can be derived from the measured attenuation α using

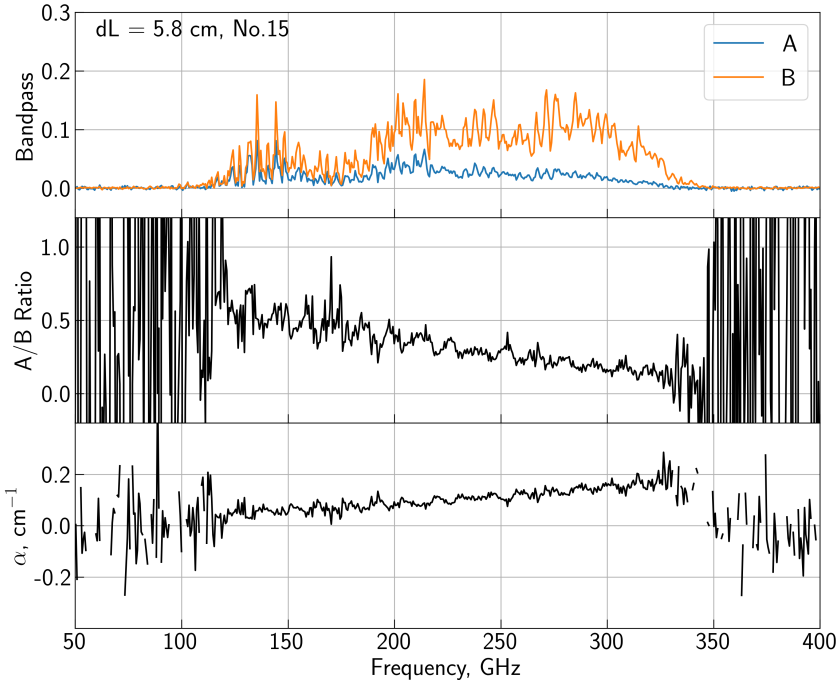

Figure 5.4: (Top) Measured spectra from a loss device pixel. Here "A" and "B" are not standing for polarizations but just labels for the two bolometers. A is the one on the longer microstrip branch while B is the one on the shorter branch. As there is no band-pass filter, frequency response spans from about 130 GHz to 330 GHz. (Middle) The ratio between the two spectra is shown in the top panel, which gets noisy outside the antenna's frequency band. (Bottom) Derived attenuation for the same pixel. The missing points are where the logarithmic function becomes undefined.

$$\tan\delta = \frac{c\alpha}{\pi\nu\sqrt{\varepsilon_R}}\,, \tag{5.2}$$

where ε_R is the relative permittivity of the transmission line. In our case, $\varepsilon_R \simeq 3.9$ (P. A. R. Ade, R. W. Aikin, et al., 2015).

Figure 5.5 summarizes the loss tangent results. The two columns are for the two detector wafers, while the rows are for the four types of loss devices. There is no type d device yielded in tile 1. The curves are the derived loss tangent. Grey curves are measurements for individual pixels, while blue curves are medians per type per tile. To better present the results, we find the medians of measured loss tangent within each of the three frequency bands covered by this test: 150, 220, and 270 GHz. The medians are shown as red data points in the plots, with the x errorbar representing the bandwidth (27%) and the y errorbar as the RMS within the band. Numbers are summarized in Table 5.1.

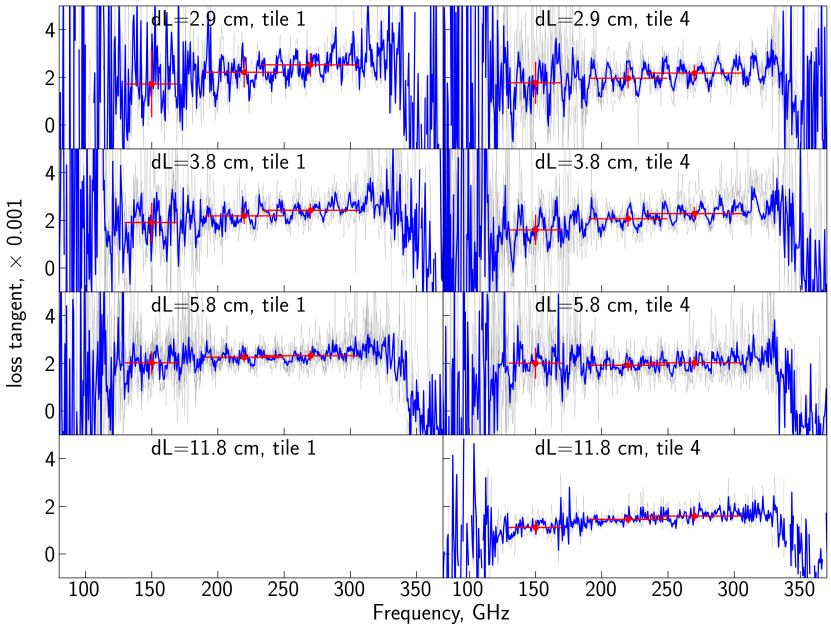

Figure 5.5: Measured loss tangents. See the text for detailed descriptions.

	tile 1			tile 2		
$\times 10^{-3}$	150 GHz	220 GHz	270 GHz	150 GHz	220 GHz	270 GHz
a	1.7 ± 1.4	2.2 ± 0.6	2.5 ± 0.5	1.8 ± 0.9	2.0 ± 0.4	2.2 ± 0.4
b	1.9 ± 0.8	2.2 ± 0.4	2.4 ± 0.3	1.6 ± 0.6	2.1 ± 0.3	2.3 ± 0.3
c	2.0 ± 0.5	2.3 ± 0.2	2.3 ± 0.2	2.0 ± 0.7	1.9 ± 0.3	2.0 ± 0.3
d				1.1 ± 0.3	1.4 ± 0.2	1.6 ± 0.2

Table 5.1: Measured results of the loss tangents for the three observing bands. This table is the same as the red data points in Figure 5.5.

Loss tangent results are consistent between the two tiles for type a, b, and c. Type d, however, suggests a lower loss tangent. Combine the numbers of the first three types, we get measured loss tangent as $1.7 \pm 0.5 \times 10^{-3}$, $2.1 \pm 0.3 \times 10^{-3}$, and $2.3 \pm 0.2 \times 10^{-3}$ for 150, 220, and 270 bands respectively. These numbers are at the high end but still consistent with the $5 \times 10^{-4} \sim 2 \times 10^{-3}$ results at ~100 GHz in (Gao et al., 2009). The slight positive dependency of the loss tangent on frequency is likely due to imperfections in the superconductor. We also notice the uncertainties do not go down by much after combining tiles and types. The uncertainties are not dominated by noise in the spectra, but instead by the fringing pattern that emerges in pair ratio and gets passed into the loss tangent results. We will discuss more about the fringing in the next section.

Reflection at the TES absorber

We see fringing pattern across frequency in the two lower panels in Figure 5.4 and all panels in Figure 5.5. There are a few notable features of the fringing. (1) It exists in all types of loss devices. (2) The frequency gap between two adjacent peaks in the fringing pattern is the same across the whole band and in all types of loss devices. (3) The amplitude of the fringing reduces with ΔL. It can hardly be seen in type d devices.

Basing on the features listed above, we think that the fringing pattern is likely to be caused by reflections along the transmission line, between the junction where the two branches split and the absorber on the TES island. Consider a lossless two-port transmission line with reflectances R_1 and R_2 on its two ends, the transmittance in frequency space has the same form as a Fabry-Perot resonator

$$T_e = \frac{(1-R_1)(1-R_2)}{1+R_1R_2-2\sqrt{R_1R_2}\cos\Delta_{ph}} \,. \tag{5.3}$$

Δ_{ph} is the phase difference between each successively transmitted beams

$$\Delta_{ph} = 2\beta L \,, \tag{5.4}$$

where L is the length of the transmission line and β is the propagation constant. Two problems are usually considered in superconducting microstrip modeling. One is the penetration of the E and H fields into the superconductors. Another one is the effect of the fringing field (Belitsky et al., 2006). For the first one, we can assume a uniform field assumption. The propagation constant in this case is

$$\beta = \frac{2\pi}{\Lambda_0}\sqrt{\epsilon_r\left[1+\frac{\lambda_0\coth(t_s/\lambda_0)+\lambda_0\coth(t_g/\lambda_0)}{h}\right]} \,. \tag{5.5}$$

Λ_0 is the vacuum wavelength. λ_0 is the London penetration depth, which is $\sim$ 50 nm for pure Nb and $\sim$ 100 nm for our case as stated in (P. A. R. Ade, R. W. Aikin, et al., 2015). t_s and t_g are the thickness of the microstrip and ground plane superconducting layer, and h is the thickness of the dielectric. Adding the fringing field into the consideration requires using the frequency-dependent penetration depth $\lambda_0 \rightarrow \lambda(\omega)$ in Eq. 5.5.

The microstrip geometry gives $t_s/h \simeq 1.5$ and $W/h \simeq 14$, and the frequency bands we care about are comfortably below the Nb gap frequency, including the fringing

field or not shouldn't make a huge difference. In our bands, λ also changes very slow with frequency. In the analysis below, we keep β as a free parameter and fit for the precise penetration depth with real data.

The power reflectivity at the split junction can be calculated as $R = \left|\frac{Z_1 - Z_2}{Z_1 + Z_2}\right|^2$ where $Z \propto 1/W$ is the characteristic impedance of the line. W is the width of the strip conductor. The width of the trunk is 8.000 μm, while the width of both branches is 3.679 μm. $Z_1 = Z_{trunck} \parallel Z_{branch}$, and $Z_2 = Z_{branch}$. We get $R_1 = 0.27$. R_2 is the reflectivity at the TES absorber, which will be fitted from the data.

For a lossy transmission line, Eq. 5.3 becomes

$$T_e = \frac{(1 - R_1)(1 - R_2)e^{-2\alpha l}}{1 + R_1 R_2 e^{-4\alpha l} - 2\sqrt{R_1 R_2}e^{-2\alpha l}\cos\Delta_{ph}} \,. \tag{5.6}$$

In Figure 5.2, lengths of the shorter and longer branches are $L = 4.54$ cm and $L+\Delta L$. The measured attenuation including the reflection is

$$\alpha' = \alpha + \frac{1}{2\Delta L}\ln\left[\frac{1 + R_1 R_2 e^{-4\alpha(L+\Delta L)} - 2\sqrt{R_1 R_2}e^{-2\alpha(L+\Delta L)}\cos\Delta_{ph}(L + \Delta L)}{1 + R_1 R_2 e^{-4\alpha L} - 2\sqrt{R_1 R_2}e^{-2\alpha L}\cos\Delta_{ph}(L)}\right] \tag{5.7}$$

We use Eq. 5.7 to fit the data for loss tangent, reflectivity at the TES absorber R_2, and the propagation constant β. We include a small linear frequency dependence in modelling the loss tangent, $\tan\delta = k\nu + const.$, which provides a quadratic drifting baseline in α'. The fringing amplitude is decided by R_2, while the fringing frequency is most sensitive to β.

We select to apply the fit on nine of our pixels with high signal-to-noise data. Results are shown in Fig. 5.6. The power reflected at the absorber is between 1 to 2%. The fit also gives a penetration depth of about 64 nm, which is closer to the London depth of the pure Nb than expected. The fit also gives loss tangents at the six BK frequency bands 30, 40, 95, 150, 220, 270 GHz as $\sim$ 1.0, 1.1, 1.4, 1.7, 2.1, 2.3 $\times 10^3$, with uncertainties much smaller than listed in Table. 5.1. The total length of the microstrip trace is 5.7 cm in 40 GHz pixels and 1.8 cm in 270 GHz pixels. The fractional power loss due to the lossy line is $\sim$ 10% at 40 GHz and $\sim$ 37% at 270 GHz. Thus, we expect much less loss in the low-frequency pixels than in our previous devices.

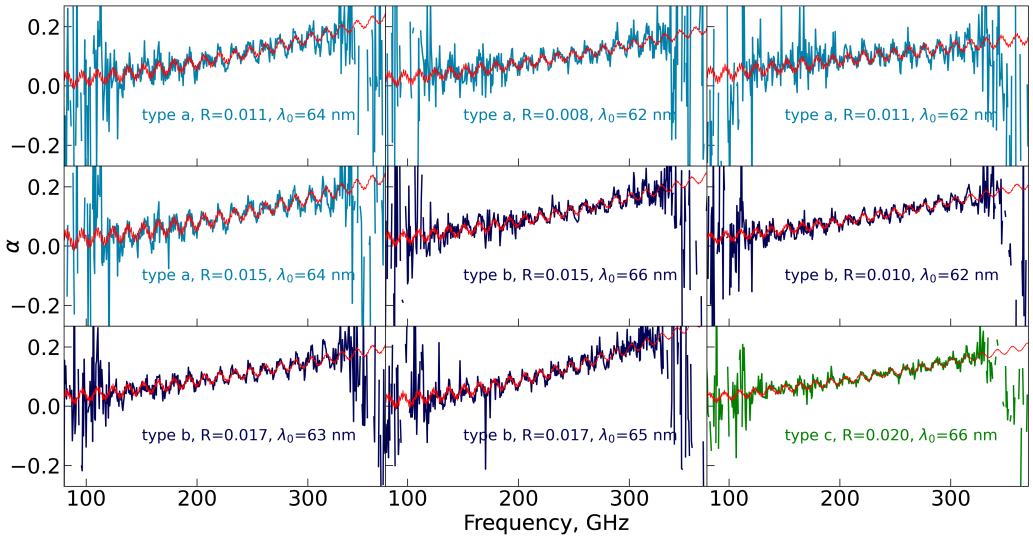

Figure 5.6: Fit results of nine high signal-to-noise ratio pixels using Eq. 5.7.

5.4 Band-pass filter

The band-pass filter between the antenna and the bolometer defines the observing frequency band. We use a three-pole Chebyshev filter design as a compromise between bandwidth and loss. The design targets a 0.25 fractional bandwidth, a 0.1 dB ripple, and an input impedance of 10 Ω. Figure 5.7 shows the filter design and Figure 5.8 shows the simulation result using Sonnet software. The two schematics are equivalent to each other through circuit transformations demonstrated in (Galbraith and Rebeiz, 2008). The inductors are short stretches of high-impedance coplanar waveguide (CPW). The capacitors are parallel plate capacitors whose capacitance is approximately proportional to the overlapping area. The geometry of each component is decided through separated simulation using Sonnet.

5.5 Transition-Edge Sensors

The Transition-Edge Sensors (TES) are superconductors operated at their transition temperature T_c. The transition between superconducting ($R = 0$) and normal ($R = R_n$) states usually happens within a very narrow temperature range. At this sharp transition edge, resistance R strongly depends on temperature T, thus forming an ultra-sensitive thermometer.

Figure 5.9 shows simplified schematics of the TES electrical and thermal circuits. Figure 5.10 shows a photo of an actual 30 GHz device. The TES superconductor (R) and the gold meander absorber are laid on a thermally isolated island connected to the surrounding thermal bath (T_0) only through a few long narrow legs. The absorber

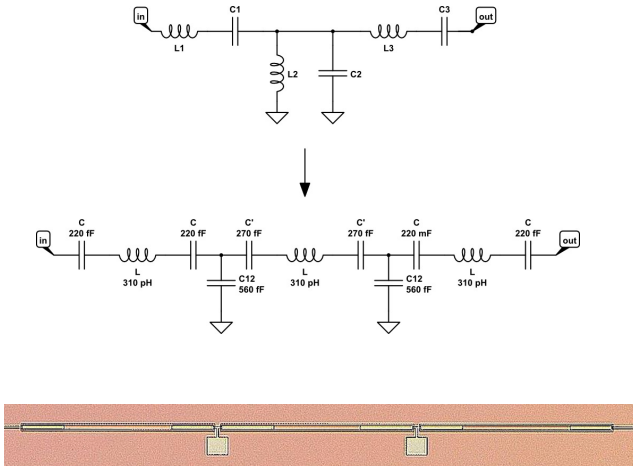

Figure 5.7: Schematics of the 30 GHz on-chip band-pass filter and a photo of the real device.

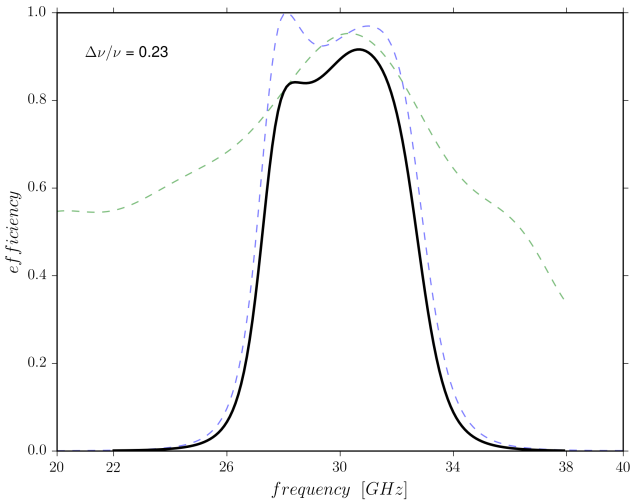

Figure 5.8: Sonnet simulation result of the 30 GHz filter (blue dash line) overlaid on the antenna simulation (green dash line).

is a lossy resistor that terminates the microstrip from the antenna and deposites the optical power onto the island in the form of heat. The random patterned blue short sessions on the gold meander are Nb to optimize power absorption at 30 and 40 GHz. The return-loss at the port of the meander is less than -20dB at the targeted frequency by Sonnet simulation. The TES is biased with constant voltage through a parallel circuit as shown in Figure 5.9. The shunt resistor R_{sh} is around 3 mΩ. A current source provides bias current I_b to the parallel circuit. The voltage across the TES is simply

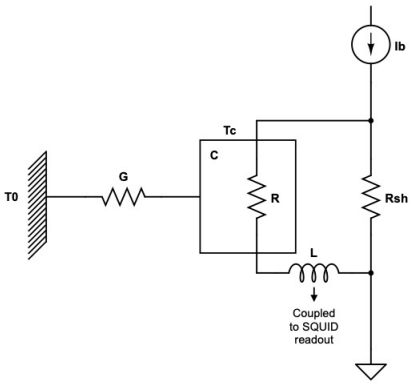

Figure 5.9: A Schematics of the voltage-biased TES.

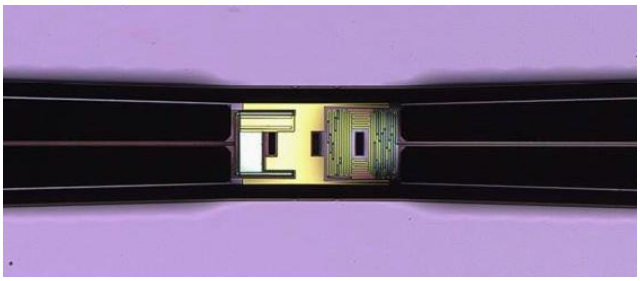

Figure 5.10: A zoom-in photo of a real TES for 30 GHz.

$$U = I_b \frac{R_{sh} R}{R_{sh} + R} \approx I_b R_{sh} \ . \tag{5.8}$$

The second part of Eq. 5.8 holds when $R \gg R_{sh}$, which is true for most part of the transition as R_{sh} is much smaller than the normal resistance (R_n) of the TES. The Joule power deposited on the TES island is

$$P_e = \frac{U^2}{R} \ . \tag{5.9}$$

The legs serve as weak thermal links between the island and the thermal bath. The geometry of the legs controls the thermal conductivity G. G is a temperature dependent property

$$G(T) \propto T^{\beta} \ . \tag{5.10}$$

β is the index of the temperature dependence of G. The bath temperature (T_0) is lower than T_c. The heat flows from the island to the thermal bath is

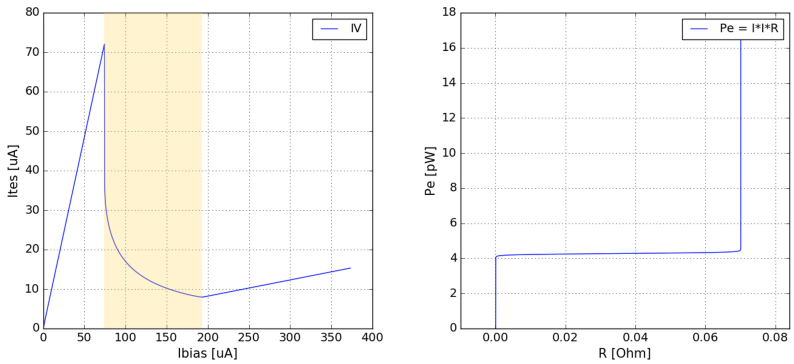

Figure 5.11: A Ti TES load curve. (Left) The I-V curve. X is the bias current. Y is the current goes through TES. The yellow color band marks out the transition. (Right) The P-R curve. X is the TES resistance. Y is the electrical power. In transition, the negative electrothermal feedback keeps the electrical power at a fixed level.

$$P(T) = \frac{G}{\beta+1}\frac{T^{\beta+1} - T_0^{\beta+1}}{T^{\beta}}\,, \tag{5.11}$$

The island, the legs, and the thermal bath together form a thermal circuit, which is coupled with the electrical biasing circuit as shown in Figure 5.9. When the TES is in transition, R changes in the same direction as T. Under a constant voltage bias, the Joule power in Eq. 5.9 decreases with an increasing temperature, forming a negative electrothermal feedback. The negative feedback allows the detectors to be operated stably at the transition edge with high loopgain and linearized response.

During operation, the TES has a balanced power budget $P = Q + P_e$, where Q stands for the incoming optical power from the antenna. $P_{sat} = P(T_c)$ is also called the saturation power of the TES. When $Q \geqslant P_{sat}$, there is no room to bias the TES in transition, and the device is saturated. We have two types of superconductors, Ti and Al, connected in serial on the detector island. The Ti has $T_c = 0.5$ K, while the Al T_c is much higher, about 1.2 K. According to Eq. 5.11, the Al TES has high saturation power and is used for in-lab or beam calibrations. In science observations, we use Ti TESs for better noise performance and stability.

Current responsivity

The derivation of the TES small-sign response can be found in (Irwin and Hilton, 2005). Since the differential equations describing the coupled electrical and thermal circuit can be linearized under the small-signal approximation, studying the response

of the TES to a small sinusoidal signal at a certain frequency is sufficient. The current responsivity ($\mathrm{d}I/\mathrm{d}P$) to a small signal at frequency ω is

$$s_I(\omega) = -\frac{1}{I_o R_o}\left[\frac{L}{\tau_{el} R_o \mathcal{L}_I} + \left(1 - \frac{R_L}{R_o}\right) + i\omega\frac{L\tau}{R_o\mathcal{L}_I}\left(\frac{1}{\tau_I} + \frac{1}{\tau_{el}}\right) - \frac{\omega^2\tau}{\mathcal{L}_I}\frac{L}{R_o}\right]^{-1} . \tag{5.12}$$

I_o and R_o are steady-state current and resistance at the operating point. $R_L = R_{sh} + R_{par}$ is the load resistance, where R_{par} is the parasitic resistance in serial with the SQUID input coil. $\mathcal{L}_I$ is the low-frequency loop gain

$$\mathcal{L}_I = \frac{P_{e,o}\alpha_I}{GT_o} , \tag{5.13}$$

where α_I is the unitless logarithmic temperature sensitivity of the TES resistance

$$\alpha_I \equiv \left.\frac{\partial \log R}{\partial \log T}\right|_{I_o} = \left.\frac{T_o}{R_o}\frac{\partial R}{\partial T}\right|_{I_o} . \tag{5.14}$$

The resistance may also have current responsivity,

$$\beta_I \equiv \left.\frac{\partial \log R}{\partial \log I}\right|_{T_o} = \left.\frac{I_o}{R_o}\frac{\partial R}{\partial I}\right|_{T_o} . \tag{5.15}$$

And the linearized perturbation of R is

$$\delta R = R_o\left(\frac{\alpha_I}{T_o}\delta T + \frac{\beta_I}{I_o}\delta I\right) . \tag{5.16}$$

In most cases, we assume $\beta_I = 0$ for our device. τ in Eq. 5.12 is the natural thermal time constant of the thermal circuit

$$\tau = \frac{C}{G} , \tag{5.17}$$

and $\tau_I = \tau/(1 - \mathcal{L}_I)$ is the thermal time constand under hard current bias. τ_{el} is the time constant of the electrical circuit without electrothermal feedback ($\mathcal{L}_I = 0$)

$$\tau_{el} = \frac{L}{R_L + R_o(1 + \beta_I)} . \tag{5.18}$$

Under constant-voltage bias ($R_L \ll R_o$) and strong feedback $\mathcal{L}_I \gg 1$, the responsivity in Eq. 5.12 can be approximated by the inverse of the bias voltage at DC

$$s_I(\omega = 0) \approx -\frac{1}{I_o R_o} \,. \tag{5.19}$$

Load curve

Detector load curve is an important tool in TES characterization and instrument diagnosis. To take a load curve, we ramp the bias current through an extensive range and record the current in the TES. Figure 5.11 shows an example of the load curve for a Ti TES. The left panel is the I-V curve. The y-axis is the TES current I, while the x-axis is the bias current I_b. According to Eq. 5.8, the voltage across the TES is approximately proportional to I_b for most parts of the transition and the normal state. In the I-V curve, there are three distinguishable sections. The straight part on the high bias side is the normal state, where the TES acts just like a typical resistor. The curved section marked with the yellow band is the transition. The straight part on the low bias side is the superconducting state, with $R = 0$, and $I_{TES} = I_b$. The right panel is the P-R curve, with the electrical power P_e on the y-axis and the TES resistance R on the x-axis. The P-R curve can be directly derived from the I-V curve.

From the P-R curve one can also recognize the normal, transition, and superconducting sections. The normal and superconducting states show up as straight vertical lines at fixed resistances (0 and R_n), while the transition has a leveled P_e because of the negative electrical thermal feedback. From Eq. 5.13,

$$\mathcal{L}_I = \frac{P_{e,o}\alpha_I}{GT} = \frac{P_{e,o}}{R_o}\frac{\partial R/\partial T|_{I_o}}{\mathrm{d}P/\mathrm{d}T} \overset{\beta_I=0}{=\!=} \frac{P_{e,o}}{R_o}\frac{\mathrm{d}R}{\mathrm{d}P} \,. \tag{5.20}$$

Because each data point in the load curve is taken under a steady-state condition, where $P = P_e + Q$ with Q fixed. The loop gain can be estimated from the load curve

$$\mathcal{L}_I = \left(\frac{P_e}{R}\frac{\mathrm{d}R}{\mathrm{d}P_e}\right)_{Load\ Curve} \,. \tag{5.21}$$

A flat P-R curve gives a large loop gain, indicating strong electrothermal feedback.

Noise model

The leading noise terms are photon and phonon noise. Photon noise is caused by the random arrival time of photons to the device. The noise equivalent power (NEP)

can be written as

$$NEP^2_{photon} = \int 2h\nu q \mathrm{d}\nu + \int q^2 \mathrm{d}\nu \simeq 2Qh\nu_0 + Q^2/\Delta\nu \ . \tag{5.22}$$

The first term is the shot noise, whereas the second term is the Bose noise or wave noise. $q = q(\nu)$ is the loading spectrum. The approximation in Eq. 5.22 assumes a uniform spectrum within the band. ν_0 is the band center while $\Delta\nu$ is the bandwidth.

The phonon noise or the thermal fluctuation noise (TFN) is

$$NEP^2_{phonon} = 4k_B T_0^2 G F(T, T_0) \ . \tag{5.23}$$

F is a unitless function of the island temperature T and the bath temperature T_0,

$$F(T, T_0) = \frac{\beta + 1}{2\beta + 3} \frac{(T_0/T)^{2\beta+3} - 1}{(T_0/T)^{\beta+1} - 1} \ . \tag{5.24}$$

The Johnson noise from the TES itself is

$$NEP^2_{TES} = 4k_B T I^2 R \frac{\xi(I)}{\mathcal{L}_I^2}(1 + \omega^2\tau^2) \ . \tag{5.25}$$

ξ is a factor accounting for the excess Johnson noise. The strong electrothermal feedback suppresses the Johnson noise power when the detector is in transition. The Johnson noise from the shunt resistor is

$$NEP^2_{shunt} = 4k_B T_0 I^2 R_{sh} \frac{(\mathcal{L}_I - 1)^2}{\mathcal{L}_I^2}(1 + \omega^2\tau_I^2) \ . \tag{5.26}$$

The SQUID readout noise is usually quoted in $NEI \simeq 3\mathrm{pA}/\sqrt{\mathrm{Hz}}$, and can be converted into NEP with the responsivity $|s_I(\omega)|$ in Eq. 5.12.

$$NEP^2_{SQ} \simeq \left(3\mathrm{pA}/\sqrt{\mathrm{Hz}}\right)^2 / |s_I(\omega)|^2 \ . \tag{5.27}$$

A low responsivity can worsen the readout noise penalty.

The current noise roll-off at kilo-Hz as a result of the serial inductor in the bias circuit and the electrothermal feedback. Detectors are "faster" in transition where strong electrothermal feedback occurs, usually with time constant at ms level. Considering

that the 2.8 deg/sec scan speed in our science observation and the l bands we are interested in, our science band in frequency is about 0.1 to 2.5 Hz (l 24 $\sim$ 600), which is much lower than the detector bandwidth. The actual readout rate and downsampling process are described in Section 4.3. The multiplexing nyquist frequency ought to be higher than the roll-off knee or any excess noise peak to avoid aliasing after downsampling.

Noise power can be converted into noise equivalent temperature in $\mu K_{CMB}\sqrt{s}$ unit through

$$NET/\sqrt{2} = \frac{NEP}{\mathrm{d}Q_{CMB}/\mathrm{d}T} \tag{5.28}$$

$\mathrm{d}Q_{CMB}/\mathrm{d}T$ is the temperature derivation of Eq. 5.30 at 2.73 K. It is sometimes referred to as the optical responsivity and is approximately proportional to the optical efficiency.

5.6 Optical loading

Optical loading estimation is an important step in bolometer design. We calculate the expected optical loading by treating the sources as a series of layers and using the plane-parallel atmosphere. The calculation should be good enough for the elevation angle range ($\theta > 45°$) we care about.

The generalized formula of the loading from one layer is

$$Q_i = \frac{1}{2}\int A\Omega\varepsilon_i(\nu)B(\nu, T_i)\eta(\nu)\mathrm{d}\nu \ . \tag{5.29}$$

$A\Omega = \lambda^2 = c^2/\nu^2$ is the throughput (area-solid angle product) with which the detector receives incident radiation. ε is a generalized emissivity of each layer. B is the black body radiation spectrum. η is the optical efficiency spectrum of the receiver. The $\frac{1}{2}$ factor accounts for the single polarization. The main difference between layers is the ϵ term and the temperature T.

For CMB,

$$Q_{CMB} = \frac{1}{2}\int A\Omega\left[1 - (1 - \mathcal{T}(\nu))/\sin(\theta)\right] B(\nu, T_{CMB})\eta(\nu)\mathrm{d}\nu \ , \tag{5.30}$$

where $\mathcal{T}(\nu)$ is the atmosphere transmission function, and $T_{CMB} = 2.73$ K is the CMB temperature.

The atmosphere Brightness temperature is a function of frequency $T_{atm} = T_{atm}(\nu)$. The loading is

$$Q_{atm} = \int B(\nu, T_{atm})\eta(\nu)/\sin(\theta)\mathrm{d}\nu \ . \tag{5.31}$$

The sky is usually at about 10 K or hoter. A Reighley-Jeans approximation is good enough for most of our calculations.

The instrument loading is calculated by assuming a stack of optics elements, each assigned a constant emissivity and a Reighley-Jeans temperature within the frequency band. For simplicity, we keep η in Eq. 5.29 as the receiver end-to-end optical efficiency, and put the transmission of an intermediate lay into ε. Using the Rayleigh-Jeans formula, the total instrument loading is

$$Q_{inst} = \sum_i \int \varepsilon_i k_B T_i \eta(\nu)\mathrm{d}\nu = k_B \bar{\eta}\Delta\nu \sum_i \varepsilon_i T_i \tag{5.32}$$

The expected loading for 30 and 40 GHz is summarized in Table 5.2.

band	GHz	30	40
Q_{CMB}	pW	0.07	0.08
Q_{atm}	pW	0.22	0.63
Q_{inst}	pW	0.19	0.26
Q	pW	0.48	0.97

Table 5.2: Expected optical loading at 30 and 40 GHz, assuming 0.3 optical efficiency and 0.27 fractional band width.

5.7 30/40 GHz Bolometer Design

The main goals of the bolometer design are to (1) have photon noise dominated device while (2) avoid saturation in observation:

$$NEP^2_{photon} > NEP^2_{phonon} + NEP^2_{TES} + NEP^2_{shunt} + NEP^2_{SQ} \ , \tag{5.33}$$

$$P_{sat} > Q \ . \tag{5.34}$$

The leading term on the RHS of Eq. 5.33 is the phonon noise. As shown in Eq. 5.23, phonon noise can be suppressed in bolometer design by lowering G, which

means lowering P_{sat}. Eq. 5.33 then sets upper limits for P_{sat} and G, while Eq. 5.34 provides the lower limits.

Eq. 5.34 needs to be strengthened for enough biasing margin in observation. The calculated loading from Section 5.6 could be off from the reality because of the scattered detector parameters in fabrication, fluctuations in atmosphere temperature, and unexpected extra loading. We define a safety factor (SF) as the ratio between P_{sat} and the expected optical loading Q. Usually, a SF about $2 \sim 3$ can satisfy both requirements.

Figure 5.12 shows the per-bolometer NET calculated under different assumptions of band averaged optical efficiency and $G_c(T_c = 0.5\text{K})$. Detector NET goes down with increasing photon collecting ability and lower G_c. Black lines show the contours of a few safety factors. We pick the assumption of 30% band average optical efficiency basing on experiences from former experiments. As discussed in Sec. 5.3, we don't expect much different optical performance between the low-frequency and former bands. The targeted parameters for 30/40 GHz TESs are summarized in Table 5.3, with loadings and noise calculated as described in previous sections.

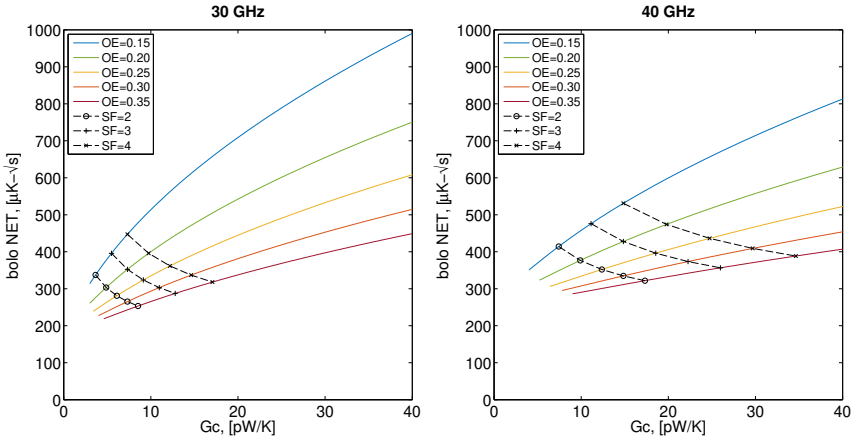

Figure 5.12: NET versus optical efficiency and G_c assuming ideal loading condition.

G is controlled by the number and geometry of the bolometer legs. The bolometers for 30 and 40 GHz take the 6-leg island design. All six legs consist of a 1μm layer of low stress nitride (LSN), a 0.27μm layer of silicon dioxide (or interlayer dielectric, ILD), and a 0.17μm layer of Nb ground plane above, except the DC bias line which does not have the ground plane layer. The three legs hosting bias lines and the microstrip for optical signal have an extra 0.4μm Nb on the top. The cross-section geometry for the 6-leg island design is summarized in Table 5.4.

parameters		30	40	sensitivity		30	40
$\bar{\nu}$	GHz	30	40				
$\Delta\nu/\bar{\nu}$		0.27	0.27				
$\bar{\eta}$		0.30	0.30				
dP/dT	pW/K	0.034	0.045				
Q_{atm}	pW	0.22	0.63				
Q_{inst}	pW	0.19	0.26				
Q_{CMB}	pW	0.07	0.08				
Q	pW	0.48	0.97				
T_0	K	0.27	0.27	NEP_{photon}	aW/$\sqrt{\text{Hz}}$	8.7	15.0
T_c	K	0.50	0.50	NEP_{phonon}	aW/$\sqrt{\text{Hz}}$	6.9	9.8
β		2	2	NEP_{TES}	aW/$\sqrt{\text{Hz}}$	1.0	1.4
G_c	pW/K	6.8	13.8	NEP_{shunt}	aW/$\sqrt{\text{Hz}}$	0.8	1.1
G_{450}	pW/K	5.5	11.2	NEP_{SQ}	aW/$\sqrt{\text{Hz}}$	3.5	5.0
SF		2	2	$NEP_{total(aliased)}$	aW/$\sqrt{\text{Hz}}$	11.8	18.9
R_0	Ω	0.03	0.03	NET	$\mu K_{CMB}\sqrt{s}$	260	318

Table 5.3: Designed parameters of the 30/40 GHz detector and the expected sensitivities.

Type	N legs	Width, μm				Thickness, μm			
		LSN	GP	ILD	MS	LSN	GP	ILD	MS
support	4	4.0	4.0	2.5		1.00	0.17	0.27	
antenna	1	9.0	9.0	7.0	5.0	1.00	0.17	0.27	0.40
DC bias	1	9.0	9.0	7.0	4.0	1.00		0.27	0.40

Table 5.4: Cross-section geometry of the 6-leg island design.

Figure 5.13: A photo of the 30 GHz bolometer island.

With the same cross-section geometry, the thermal conductivity G scales as the inverse of the leg length. In *Keck* 150 GHz, all six legs were 535 μm long, the median G measured at 450 mK (G_{450}) was ~64 pW/K. BICEP3 95 GHz detector had legs 801 μm long, with a median measured G_{450} ~ 31 pW/K. The final leg lengths decided for 30 and 40 GHz are 1400 and 2650 μm. The expected G_{450}s of these new island designs are 11 and 21 pW/K, matching the measured values pretty well. However, these Gs are much higher than the targets in Table 5.3. Before and during the deployment of BA1, we suffered large extra detector loading which pushed us to increase the saturation power. We discussed more about the extra-loading in following chapters. In addition to that, the long skinny legs added

challenges in fabrication and caused concerns about yield. Figure 5.13 shows a photo of a 30 GHz TES. Longer leg designs were not our first choice before gaining enough confidence about fabrication yield.

Chapter 6

BA1 RECEIVER CHARACTERIZATION

BA1 was deployed to the South Pole at the end of 2019, together with the new telescope mount. Three *Keck* receivers at 220 and 270 GHz were adapted to the new mount and run alongside BA1. During the austral summer of 2021-2022, we upgraded BA1 with replacements of low-performance tiles and a new mesh filter stack. This chapter summarized the characterizations of BA1 in both deployments.

6.1 Detector counts

In 2020, we fielded four 30 GHz, seven 40 GHz, and one prototype dichroic modules. Single-band 30 and 40 GHz tiles use the slot antenna and band-pass filter design introduced in Chapter 5, with 16 and 25 pixels per tile respectively. The dichroic tile uses broad-band bowtie antenna design and has 16 pixels for each band on the same wafer.[1]. In 2022, we swapped out a few low yield modules and installed more dichroic ones as a part of the effort to improve the overall synchrotron sensitivity. Table 6.1 lists the detector counts in both deployments. We name single-band 30 and 40 GHz modules with the letter "N" and "M" and use "Mx" for the dichroic. Figure 6.1 shows the FPU configuration in the 2020 versus 2022.

deployment year	type of module	number of modules	pixe perl module	total TES pairs
2020	30	4	16	64
	40	7	25	175
	dual-band	1	16	32
2022	30	4	16	64
	40	4	25	100
	dual-band	4	16	128

Table 6.1: Deployed detector counts.

Counting readout and fabrication hits, the pixel yield of 30 GHz was ~ 40% in 2020 and 2021, while increased to ~ 70% in 2022 as a result of the tile swapping. The pixel yield of 40 GHz also increased from 50 ~ 60% in 2020 and 2021 to ~ 70% in 2022.

[1]Corwin Shiu, Princeton. cshiu@princeton.edu

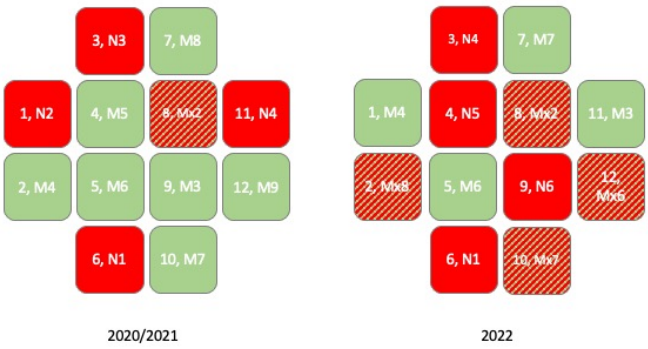

Figure 6.1: BA1 FPU configuration in 2020 and 2022 deployments.

6.2 Optical efficiency

The end-to-end optical efficiency is measured at the South Pole after the integration and cool-down of the receiver. We use aperture-filling sources at two different temperatures, liquid nitrogen at 77 K and the lab environment temperature at 300 K. For the frequency bands in interest, both sources are in Rayleigh-Jeans regime. We take Al TES load curves with both sources. The difference in optical loading at one polarization can be calculated as

$$\Delta P = \int_0^\infty A\Omega\eta(\nu)\frac{\nu^2 k_B \Delta T}{c^2} d\nu = k_B \Delta T \int_0^\infty \eta(\nu) d\nu \ . \tag{6.1}$$

$A\Omega = \lambda^2 = c^2/\nu^2$ is the throughput (area-solid angle product) with which the detectors receive incident radiation. $\eta(\nu)$ is the detector spectrum. ΔP can be measured directly from the detector P-R curve as shown in Figure 6.2. $\Delta T = 300 - 77 = 223$K. We denote $\mathrm{d}P/\mathrm{dT} \equiv \Delta P/\Delta T$. This number can be used to calculate the band-averaged end-to-end optical efficiency with the spectral band width $\Delta\nu$

$$\bar{\eta} = \frac{\mathrm{d}P}{k_B \mathrm{d}T \Delta\nu} \ . \tag{6.2}$$

As discussed in Section 7.1, a non-negligible fraction of the total optical power was coupled directly to the TES island without passing through the designed optical path. Each detector wafer has a few dark TESs which are not connected to the antenna. The dark TES's response in the optical efficiency measurement, $\mathrm{d}P/\mathrm{d}T_{dark}$, can be

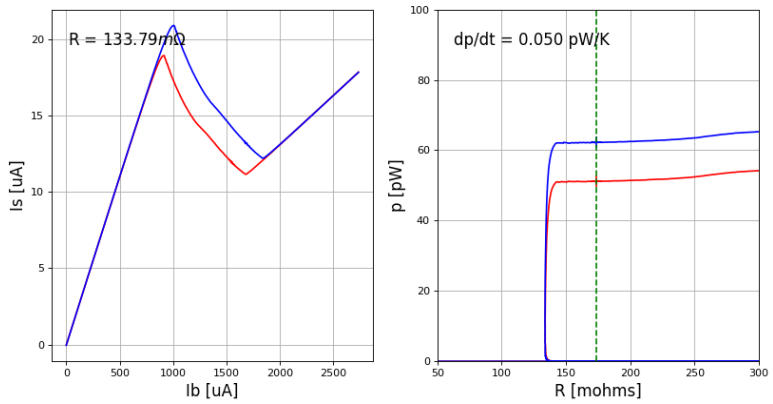

Figure 6.2: Example Al load curves taken for the optical efficiency measurement. Red curves are taken with 300 K source, whereas the blue curves are taken with the 77 K liquid nitrogen.

subtracted from the $\mathrm{d}P/\mathrm{d}T$ measured from light pixels to get an estimation of the in-band response.

$$(\mathrm{d}P/\mathrm{d}T)_{light} = (\mathrm{d}P/\mathrm{d}T) - (\mathrm{d}P/\mathrm{d}T)_{dark} \ . \tag{6.3}$$

We have done the measurement three times for BA1 in 2020, 2021, and 2022 season respectively. The results are summarized in Table 6.2. The 2021 measurement were to check for the impact from the delaminated low-pass mesh filters. $\mathrm{d}P/\mathrm{d}T$s are consistent between 2020 and 2021 except for M8 which had the worst delaminated filter. In 2022, the new filter stack largely eliminated the dark response, with a mild reduction in the light $\mathrm{d}P/\mathrm{d}T$. The last two rows summarize the median $\mathrm{d}P/\mathrm{d}T$s of all the single-band 30 and 40 modules. Figure 6.3 and 6.4 show the distribution of $\mathrm{d}P/\mathrm{d}T_{light}$ and $\mathrm{d}P/\mathrm{d}T_{dark}$ in 2020 and 2021.

With $\mathrm{d}P/\mathrm{d}T_{light}$ and bandwidth (Section 6.3), use Eq. 6.2, we can estimate the band-averaged end-to-end efficiency. 40 GHz tiles have about 30% optical efficiency, consistent with our assumption in device design. However, for 30 GHz, the optical efficiency is only about 20% in the best case, causing huge degradation in noise performance. The cause of the low efficiency is still under investigation.

The first dichroic Mx2 has a similar band-averaged efficiency as single-band 30 but a much higher $\mathrm{d}P/\mathrm{d}T$, thanks to its much wider bandpass (see Section 6.3), which means higher optical responsivity and faster mapping speed. The new dual-band tiles in 2022, Mx7, and Mx8, have the exact same design as Mx2. However, the measured $\mathrm{d}P/\mathrm{d}T$s of the new tiles are much lower than Mx2. We suspect the change

of oxide recipe in fabrication, but the actual cause is not clear. Mx6 is not included here for its extremely low yield.

dP/dT	2020			2021			2022		
(pW/K)	total	dark	light	total	dark	light	total	dark	light
N1 (30)	0.027	0.007	0.020	0.027	0.007	0.020	0.022	0.003	0.019
N2 (30)	0.028	0.010	0.018	0.028	0.009	0.019			
N3 (30)	0.027	0.007	0.020						
N4 (30)	0.027	0.007	0.020	0.029	0.008	0.021	0.021	0.002	0.019
N5 (30)							0.019	0.003	0.016
N6 (30)							0.018	0.003	0.015
M3 (40)	0.062	0.006	0.056	0.064	0.005	0.059	0.054	0.001	0.053
M4 (40)	0.063	0.006	0.057	0.065	0.005	0.060	0.058	0.002	0.056
M5 (40)	0.056			0.054					
M6 (40)	0.066	0.007	0.059	0.065	0.008	0.057	0.057	0.002	0.055
M7 (40)	0.057	0.005	0.052	0.058	0.006	0.052	0.051	0.002	0.049
M8 (40)	0.047	0.007	0.040	0.038	0.005	0.033			
M9 (40)	0.064	0.007	0.057	0.067	0.007	0.060			
Mx2 (30)	0.062	0.008	0.054	0.059	0.007	0.052	0.051	0.002	0.049
Mx2 (40)	0.046	0.008	0.038	0.048	0.007	0.041	0.044	0.002	0.042
Mx7 (30)							0.016	0.002	0.014
Mx7 (40)							0.022	0.002	0.020
Mx8 (30)							0.011	0.001	0.010
Mx8 (40)							0.005	0.001	0.004
Ns (30)	0.027	0.007	0.020	0.028	0.008	0.020	0.020	0.003	0.017
Ms (40)	0.059	0.006	0.053	0.060	0.005	0.055	0.053	0.002	0.051

Table 6.2: Measured dP/dT in 2020 and 2022. Mx6 installed in 2022 has very low yield and has been excluded from this table.

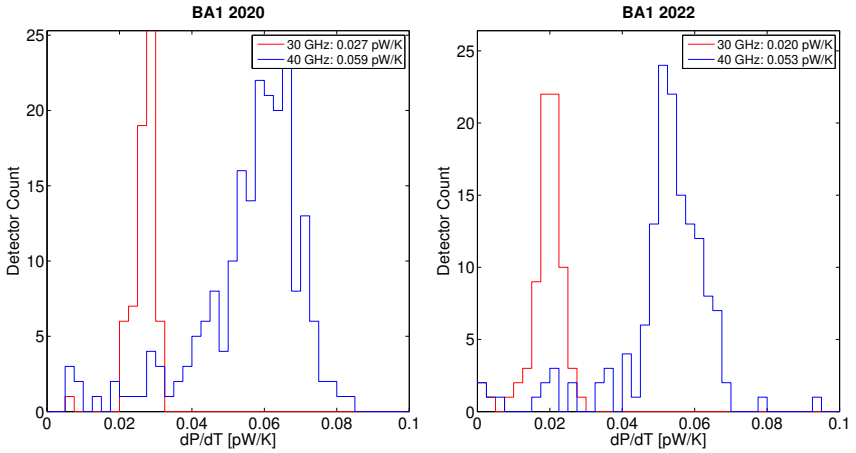

Figure 6.3: Histogram of light pixel dP/dT in 2020 and 2022.

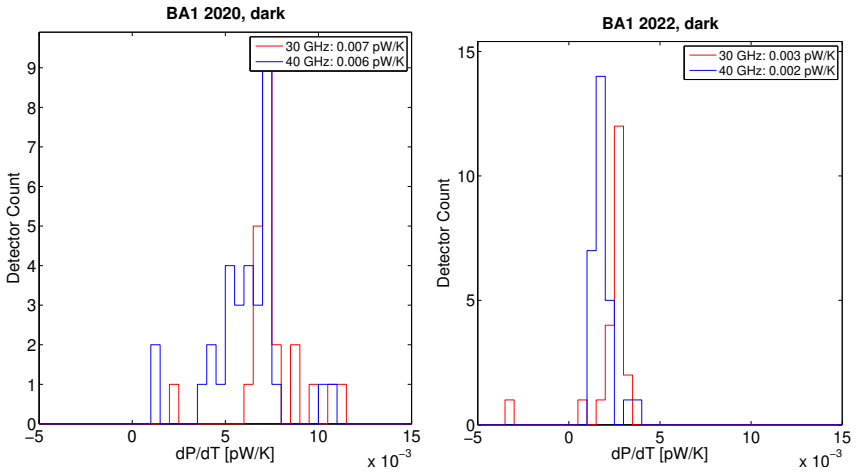

Figure 6.4: Histograms of $\mathrm{d}P/\mathrm{d}T$ for dark TESs measured in 2020 and 2022.

6.3 Spectral response

We measured detector spectra using a Fourier Transform Spectrometer (FTS) as shown in the left photo of Figure 6.5. The right panel of Figure 6.5 is a schematic of the FTS we use. The instrument is of a Martin-Puplett design (Martin and Puplett, 1970) using a polarized wired grid as a beam splitter. In the time-reversed sense, the collimated beam from the detectors shines inside the FTS through a 7-by-7 inches square aperture at the bottom of the FTS crate. The input wire grid is right above the aperture, reflecting a single polarization to the horizon direction. Because of the limited size of the FTS aperture, it isn't able to fill the beams of BA. However, it is possible to angle it towards the beam centers of selected detectors. The input wire grid is sitting on a structure of a goniometer and a rotation stage, allowing it to change pointing to cover different parts of the FPU. Another wire grid splits the reflected beam toward the two arms, each with a rooftop mirror at the end. One of the rooftop mirrors is fixed, while the other one is movable along the arm. The reflected beams recombine at the second pass of the beam splitter then illuminate a focusing parabolic mirror. The focused light from the mirror is again split into two polarizations; one terminates on Eccosorb HR-10 microwave absorber at ambient temperature, and the other on HR-10 held at 77 K in a container of LN2. The difference in temperature between the two sources leads to an interference pattern in the detector response when the path length is changed (Lesurf, 2019).

A Fourier Transform of the time-order signal gives the detector's spectral response. In our data taking, we make the mirror move at 1.905mm/s and use the data of a full length of 230mm scan. The spectrum has a frequency resolution of 0.65GHz

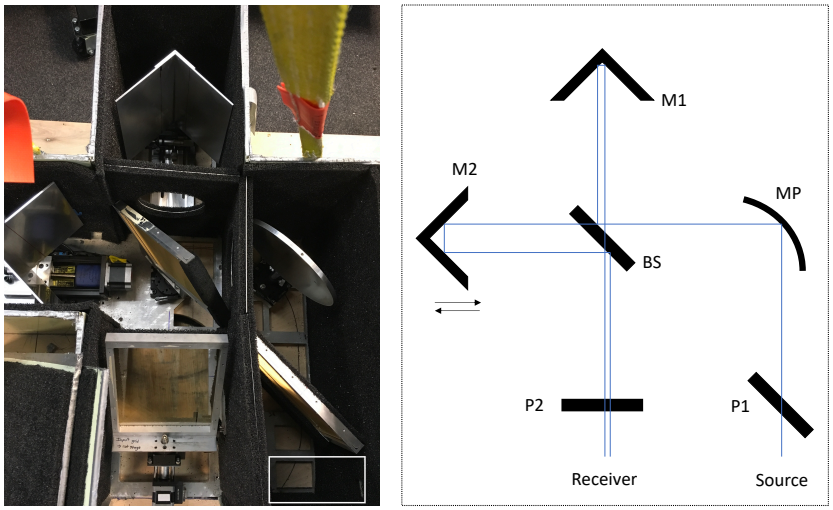

Figure 6.5: A photo of the FTS and its schematic. P1 and P2 are the input and output polarized grids. MP is the parabolic mirror. M1 and M2 are two roof shape mirrors. M1 is fixed, whereas M2 can be moved back and forth along the optical path. BS is the beam splitter. The white box at the lower right corner of the photo shows the location of the liquid nitrogen source.

with the maximum frequency at a few thousands GHz.

The y-axis of the spectrum can be scaled into end-to-end optical efficiency using the measured $\mathrm{d}P/\mathrm{d}T$. $S(\nu)$ is the spectrum we measured in arbitrary unit, while $\eta(\nu)$ is the efficiency spectrum. The conversion is

$$\eta(\nu) = \frac{\mathrm{d}P}{k_B \mathrm{d}T} \frac{S(\nu)}{\int S(\nu)\mathrm{d}\nu} \,. \tag{6.4}$$

The band-averaged efficiency in Eq. 6.2 is $\bar{\eta} \equiv \int \eta(\nu)\mathrm{d}\nu/\Delta\nu$. Figure 6.6 shows the efficiency spectrum for single-band detectors in 2020 and 2022.

In 2022, the 30 GHz spectra have a "dip" around 29 GHz which did not exist in the 2020 spectra, as shown in Figure 6.6. The change appears clearer in the band-averaged spectra in Figure 6.7. The 40 GHz bandpass is consistent between the two years. The "dip" also shows up in the spectrum of Mx2.

We calculate the band center as the mean frequency of the bandpass

$$\bar{\nu} = \frac{\int \nu S(\nu)\mathrm{d}\nu}{\int S(\nu)\mathrm{d}\nu} \,. \tag{6.5}$$

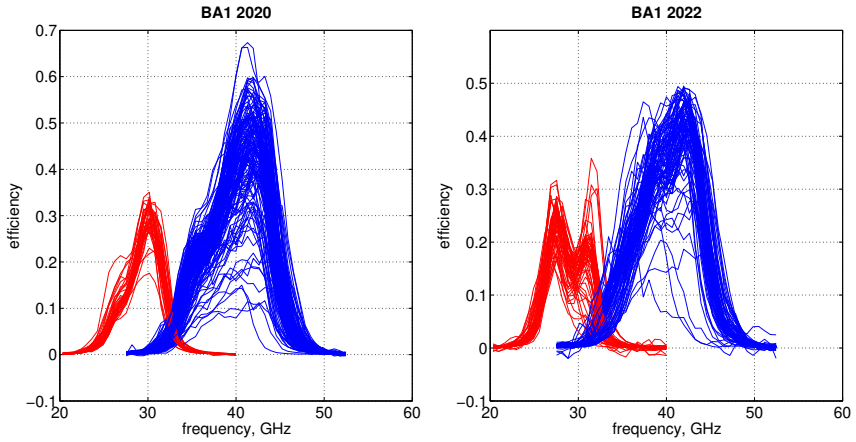

Figure 6.6: Efficiency spectra of detectors at 30 (red) and 40 (blue) GHz measured in 2020 and 2022.

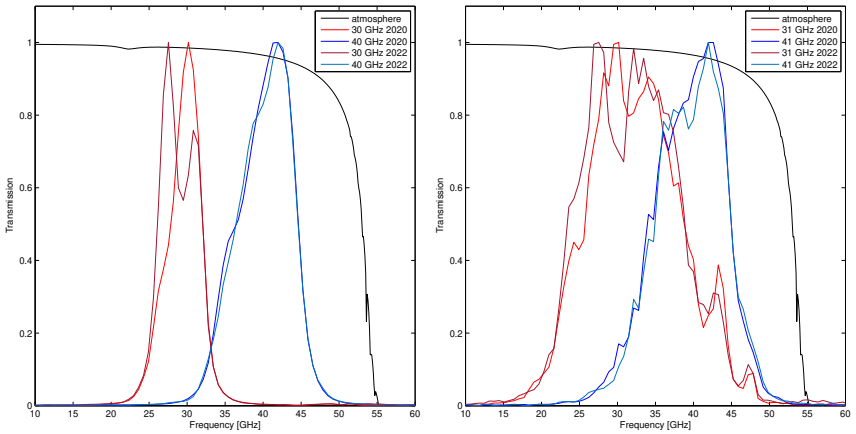

Figure 6.7: Peak normalized band-averaged spectra for (Left) single-band 30/40 and (Right) dichroic bands in Mx2. The transmission of the atmosphere is plotted as a black solid curve in the background. The dichroic 30 GHz has much wider bandpass than the single-band 30 GHz. A "dip" shows up at about 29 GHz in both single and dual band detector in 2022.

Band width uses the definition

$$\Delta\nu = \frac{(\int S(\nu)\mathrm{d}\nu)^2}{\int S^2(\nu)\mathrm{d}\nu} \,. \tag{6.6}$$

Figure 6.8 shows the measured band center and fractional bandwidth in 2020 and 2022 for all the single-band detectors. The distributions are narrow, suggesting we have a uniform bandpass for single-band detectors. In 2022, the 30 GHz band center shifted slightly lower while the fraction bandwidth increased because of the "dip" at the center of the bandpass.

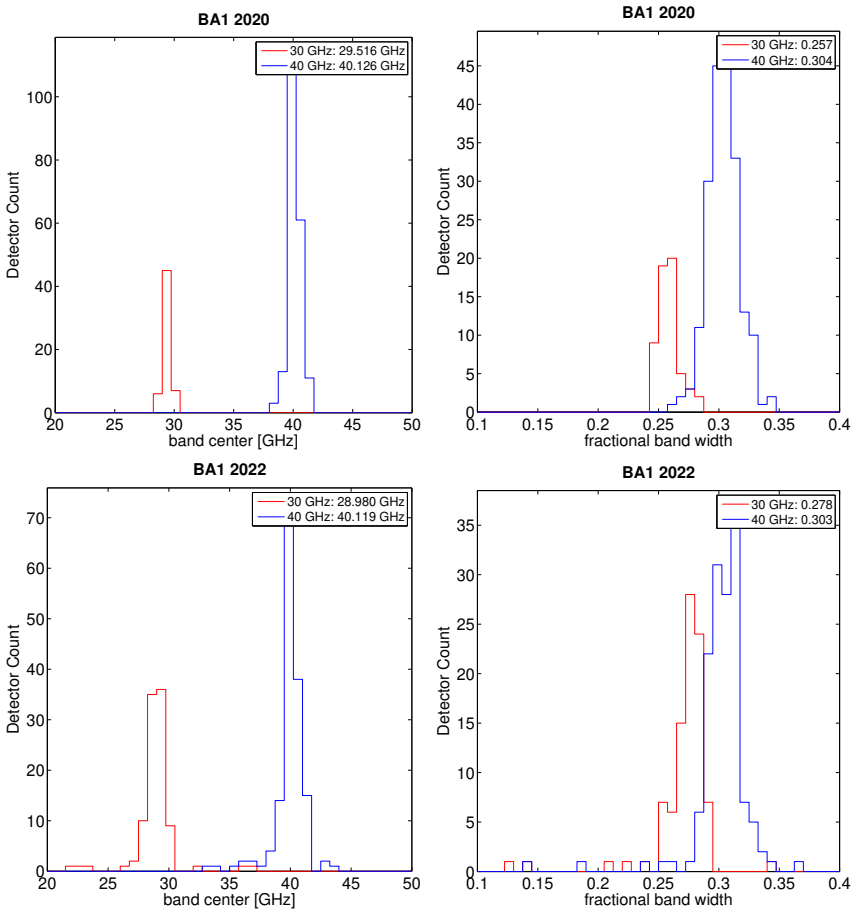

Figure 6.8: Histograms of the band center and the fractional band width for single-band detectors. (Left-Top) Band center 2020; (Left-Bottom) Band center 2022; (Right-Top) Band width 2020; (Right-Bottom) Band width 2022.

All the spectra shown in this section are without beam-filling correction, which is expected to have a limited effect on the results (St. Germaine, 2021). For more information of the corrections, see (Karkare, 2017) and (St. Germaine, 2021).

6.4 Bolometer properties

T_c, G and β

The transition temperature T_c, the thermal conductivity between the TES island and thermal bath G, and the temperature index of the thermal conductivity β can be measured by taking load curves at multiple bath temperatures in a "dark run". "Dark run" refers to the cryogenic run with no optical loading to the detector, usually achieved by covering the detector module with a metal cap whose inner side is blackened. Because the cap is at the same temperature as the Nb module box around a few hundreds mK, it thus contributes negligible loading to the detector.

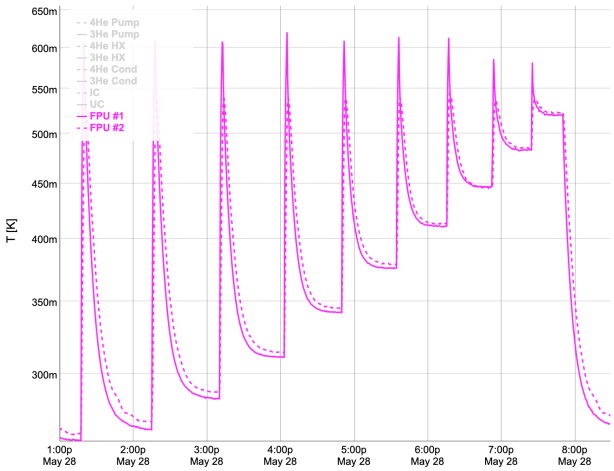

Figure 6.9: FPU temperatures through a full dark measurement. The FPU1 cernox is on the FPU Cu plate, while the FPU2 cernox is on the module cover.

Without optical loading, in superconducting transition, we have

$$P_e = P_{sat} = \frac{G_c}{(\beta+1)} \frac{T_c^{\beta+1} - T_0^{\beta+1}}{T_c^{\beta}} \,. \tag{6.7}$$

G_c is the thermal conductivity at T_c. By varying T_0 and measuring P_e from detector load curves, we can fit the rest of the parameters.

For BA1 detector testing, the dark runs were carried out in a testbed cryostat in the basement of the Cahill Centre for Astronomy and Astrophysics of Caltech. The testbed is called ShortKeck, which has the same aperture size as the *Keck* receivers, but without any optics, allowing fast turn around between runs. ShorkKeck can host two BA modules in each run. A heater is mounted right on the FPU for varying the bath temperature.

Figure 6.9 shows FPU temperatures in a dark measurement. Without extra-loading from the heater, the bath temperature is usually about 260 mK in a ShortKeck dark run. With no bias current applied, the detectors are superconducting. To get into Ti transition at about 500 mK, we need to warm the FPU up to above 500 mK with the FPU heater. The FPU temperature shoots up above 500 mK in only a few seconds. Large bias current is applied to the TES during the warm-up, making sure the detector stay out of superconducting when cool back down. We then reduce the heater power and let the FPU settle at the desired temperature. Detector load curves are taken at the settled temperature.

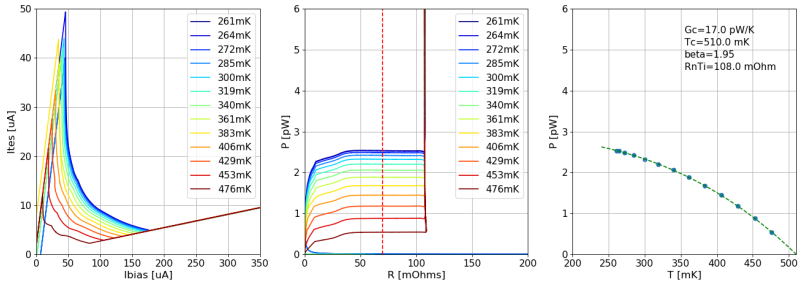

Figure 6.10: The G measurement. From left to right, we have the I-V curves, the P-R curves, and the $P_e - T_0$ fit. The saturation power is measured at a fixed resistance marked out by the red dash line in the middle panel.

Figure 6.10 shows an example of the dark measurement data and curve fitting. With the increase of the bath temperature, the transition gets "smaller" in the I-V curve, and the P_{sat} gets lower and lower. The saturation powers are measured at a fixed resistance for all the load curves. The last panel shows the fit to the Eq. 6.7.

Figure 6.11 shows the bolometer parameters of all the tiles we have done dark runs with in 2020. At the time, N1 was the only 30 GHz tile we had acquired dark run data, so the first row panels are for N1 data only. The second row is for 40 GHz tiles, including M3, M4, M5, M6, M7, and M9. The bolometer parameters are scattered between tiles, which is caused by a combination of fabrication and measurement uncertainties. However, T_c and β have medians around 0.5 K and 2 as expected. The bump in the 40 GHz G histogram at around 40 to 50 pW/K is from M9, which has the same bolometer design as the other 40 GHz tiles but a mysteriously high G. Except for the outliers in M9, the yield Gs roughly match our expectations of the designs in Section 5.7.

TES normal resistance R_n

TES normal resistance can be measured from the slope of the normal portion of the I-V curve. The typical normal resistance of a Ti TES in the former BK experiments is between 50 and 100 mΩ. We have noticed that the normal resistance of the BA detectors is much higher, with a large radial gradient across the tile. Figure 6.12 shows the Ti R_n of a 40 GHz detector tile in BA1. The four pixels around the tile center have $R_n \sim 90$mΩ, while the corner pixel goes up to 150mΩ. The radial pattern is a bit off centered because the TES bolometers locate at the edge of each pixel. The radial pattern of R_n can be seen in all the 6-inch tiles fabricated between 2018 and 2020.

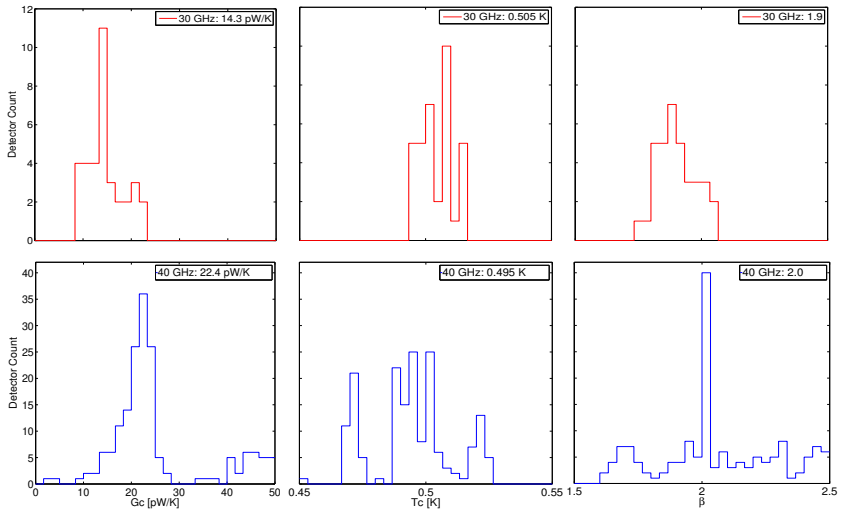

Figure 6.11: Measured bolometer parameters of some deployed tiles in 2020. The first row is for the 30 GHz single-band. We only had data for N1 at the time. The second row is for the 40 GHz single-band, including M3, M4, M5, M6, M7, and M9, sharing the same bolometer design.

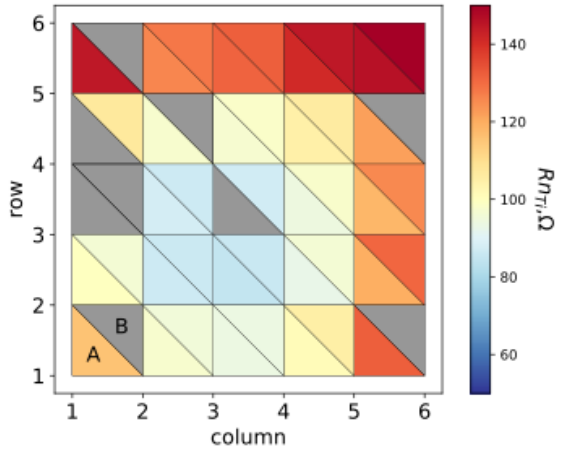

Figure 6.12: Tile map of R_n for one of the 40 GHz tiles in BA1.

6.5 Beam

The far-field optical response of BA1 detectors was measured at the beginning of the first observing season of BA1. The standard far-field distance is

$$d_{FF} = 2D^2/\lambda \, . \tag{6.8}$$

With the 550 mm clear aperture of the BA receiver, the far-field distances are about 60 and 80 m for 30 and 40 GHz. The Dark Sector Laboratory is 210 m away from

the Martin A. Pomerantz Observatory (MAPO). A chopped thermal source mounted on a 10 m mast on the top of DSL's roof comfortably sits in the far-field of BA1 and is used for beam measurements. The source is chopped between the 250 K ambient temperature and ~ 10 K sky temperature at about 18 Hz with a 60 cm aperture. We affix a flat reflective mirror—composed of an aluminum sheet on a honeycomb interior—to the front of the telescope mount. This mirror redirects the beams over the lip of the ground shield structure towards the calibration source. Due to the limited extent of the mirror, the whole array would not be able to see the source all at once. We, therefore, take raster scans with the telescope at multiple sets of boresight rotations and with different mirror positions to enable full coverage of the detectors. The scans are co-added together to form the composited beam. The final step is to take the 2D Fourier transform and then average in radial bins to get a 1D beam window function. For more information on the general beam mapping process and analysis, I refer interested readers to (P. A. R. Ade, Z. Ahmed, R. W. Aikin, et al., 2019).

Figure 6.13 shows the per-band composited beams in BA1 and their 1D beam window functions. From top to bottom, there are single-band 30, dichroic 30, single-band 40, and dichroic 40. The averaged beam widths are 0.478 and 0.364 degrees for 30 and 40 GHz, respectively.

6.6 Noise performance

We can estimate the detector noise performance from the power spectral density (PSD) of the time-order data (TOD). Results can be converted into the CMB temperature unit with calibration factors applied. The detailed description of the data reduction and calibration process can be found in (Willmert, 2019) and (Crumrine, 2022). I will briefly cover the major steps in this section.

Processing the time-ordered data

Data from all TES bolometers, along with the telescope pointing information and the thermometry readout, form the basic time-ordered data (TOD) structure which we store on disk. The detector time streams have to go through a series of down-sampling and filtering steps before being recorded. Only the information corresponding to the angular scales of interest can make it to the disk and get transferred to North America through the limited bandwidth of the South Pole satellite. The first thing to do is then **deconvolve** the transfer functions of the down-sampling steps. The down-sampling steps for the detector time streams of BA1 include:

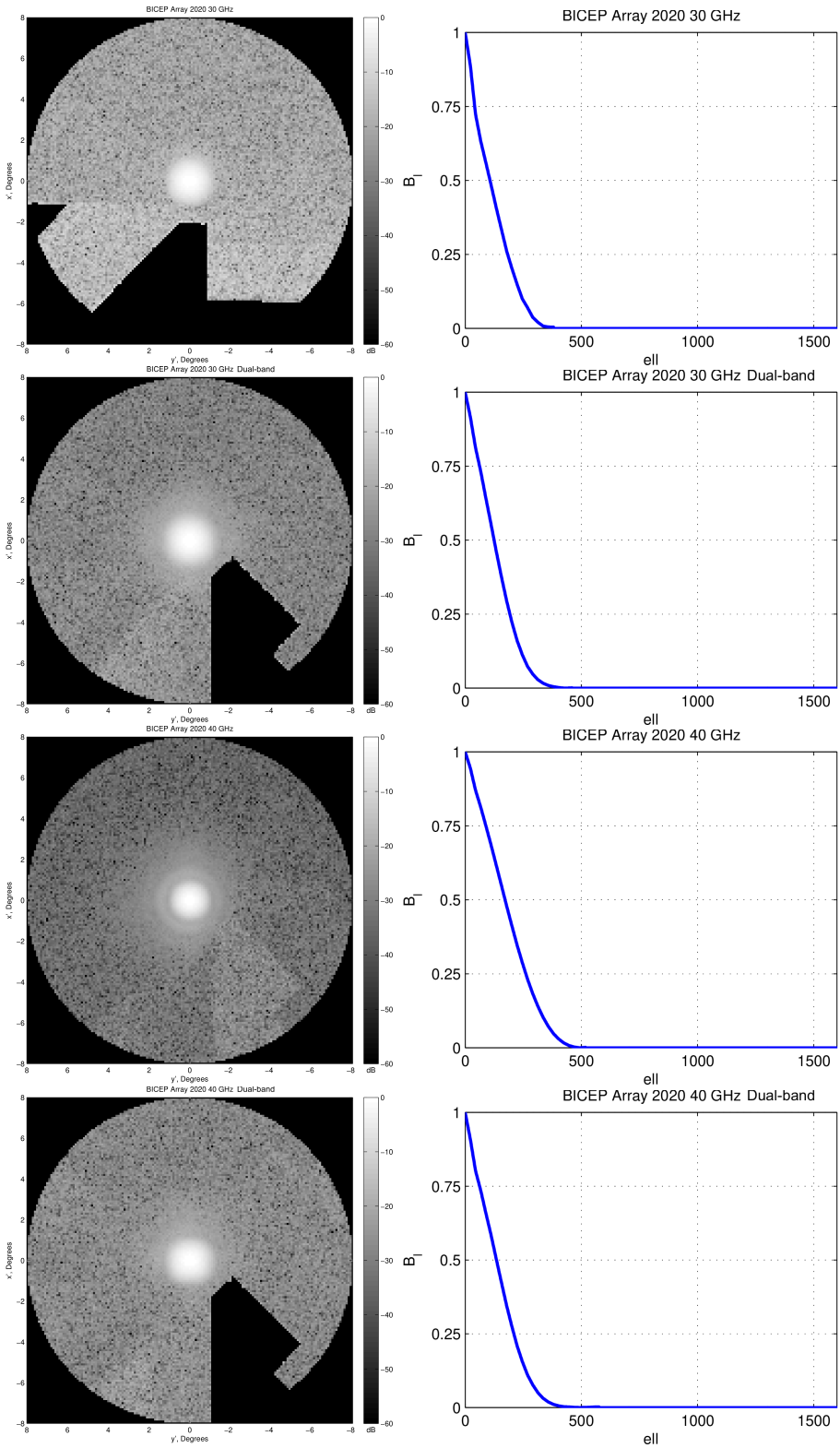

Figure 6.13: Per-band composited beams in BA1 and their 1D beam window functions. From top to bottom, we have single-band 30, dichroic 30, single-band 40, and dichroic 40. Plots by Dr. Tyler St. Germaine.

- The warm readout electronic MCE reports data of each bolometer at a frame rate of 12kHz.
- MCE applies a 4-pole Butterworth low-pass filter with a cut-off frequency at around 60Hz[2] to the data before further downsampling to about 200 Hz.
- The Linux General Control Program (GCP) (Story et al., 2012) applies an acausal Finite Impulse Response (FIR) filter and then further decimates this data by a factor of 9 for a final on-disk sample rate of 22.22 Hz.

A final 5Hz low pass filter is added to the deconvolved TOD to suppress high-frequency noise outside the interested band. The low-passed TOD is then **deglitched** and is ready for **relative gain calibration**. We normalize the TOD to the median of each frequency band using the gains measured by the elevation nods taken before and after each 50-minute scan-set. This takes care of the gain variation across the detectors in each scanset. An additional factor is added to account for the temporal variation of the gain induced by changing the bias points

$$\frac{\mathrm{d}P}{\mathrm{d}I} = I_b \frac{1 - R_{sh}/R}{1 + R_{sh}/R} \,. \tag{6.9}$$

We then take the **sum and difference** of calibrated time streams between each bolometer pair to measure the unpolarized and polarized response. A polynomial filter is applied for each half scan. We accumulate **ground subtraction** template for each hour of data taking and subtract the ground fixed signal from the TOD.

CMB calibration

We bin the TOD data into map pixels using the pointing information recorded simultaneously with the detector time streams. The resulted map is in an arbitrary feedback unit. To convert it into thermodynamic temperature units ($\mu\mathrm{K_{CMB}}$), we perform a so-called absolute calibration process using external temperature maps from Planck. The process takes two Planck maps. The first one, m_{cal}, is at a frequency close to the uncalibrated internal BK map m_{real}. The other one m_{ref} is at a different frequency. For BA1 30 and 40 GHz, the m_{cal}s are Planck30 and Planck44 temperature maps, and the m_{ref} is the Planck143 temperature map. The

[2]The cut-off of the digital filter was 30 Hz in 2020. It was increased to 60 Hz at the beginning of 2021 and preserved ever since.

external maps are re-observed to match the identical beam smoothing and filtering as the real data. The calibration factor is calculated as a function of the multipole l

$$g(l) = \frac{\langle \tilde{m}_{cal} \times \tilde{m}_{ref} \rangle}{\langle \tilde{m}_{real} \times \tilde{m}_{ref} \rangle} \,. \tag{6.10}$$

Assuming each map has independent noise, the result is unbiased. The number we use to calibrate our map, g_{abs}, is from the average of our first five l bins ($30 < l < 210$).

Time stream NET

We can take the PSD of the TOD data that goes through the standard reduction process and convert it to temperature unit with the absolute calibration factor g_{abs}. Figure 6.14 shows the band median PSD of BA1 single band 30 and 40 GHz along with the 210 and 270 *Keck* receivers using data from one tag in 2020. The dash spectra are for pair-summed data, while the solid spectra are pair-differenced. As expected from the highly unpolarized atmosphere, the $1/f$ noise has been largely suppressed by pair-differencing. The y-axis has been multiplexed by $\sqrt{2}$ to match the per bolometer NET that usually gets quoted in proposals. We take the number at 1Hz from the PSD as the estimation of the NET in this section.

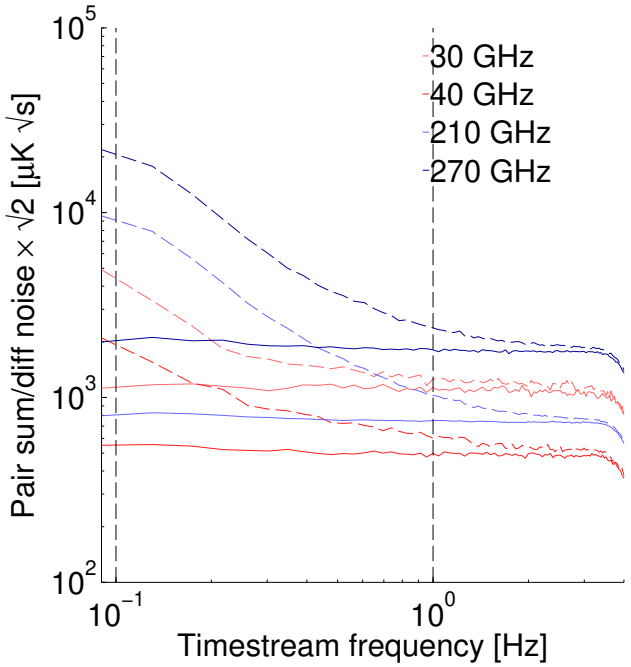

Figure 6.14: The band-median PSDs from on scanset of BA2020. Dash lines are pair-summed PSD, while solid lines are for the pair-difference result.

The NET estimation as described above has been done for all the CMB observation tags in 2020 and 2021. Table 6.3 summarizes the median NET of each detector tile and each band. The numbers are high compared with the proposed numbers in Table 4.2. 30 GHz had a median NET of 971 μK_{CMB} in 2020, which was 3.7 times the proposed 260 μK_{CMB}. With the same detector count, the mapping speed dropped to 7% of what was planned. The much better NET of the dichroic 30 GHz (Mx2) is attributed to its it's wide bandpass (Figure 6.7) and large optical response (Table 6.2). 40 GHz is slightly better but still only achieved 41% of the planned mapping speed. M8 and M9 are particularly bad. Though they have the same TES design as the other 40 GHz tile, their G are mysteriously high. In 2021, the median NET of N2, M4, and M8 increased due to the delaminated low-pass mesh filter. The other tiles were either the same as in 2020 or got slightly better. The band-median numbers improved in both frequency bands thanks to the better cryogenic performance and less loading from the instrument. However, they were still far from the desired sensitivity level.

Module (band)	2020	2021
N1 (30)	921	858
N2 (30)	928	955
N3 (30)	963	
N4 (30)	1018	1007
M3 (40)	390	386
M4 (40)	447	461
M5 (40)	540	546
M6 (40)	403	387
M7 (40)	467	427
M8 (40)	611	649
M9 (40)	819	821
Mx2 (30)	369	351
Mx2 (40)	656	515
single-band 30	971	914
single-band 40	495	479

Table 6.3: TOD-derived NET for BA1 in 2020 and 2021 in μK_{CMB} unit. The numbers are the median of each tile through all the tags that survived the standard data quality cuts. The last two rows are the median of frequency bands. These TOD-derived NET are consistency with the results we got from CMB maps as discussed in (Crumrine, 2022).

In the following chapters, we will discuss the cause of BA1's high noise level in the 2020 and 2021 seasons.

Chapter 7

BA1 DIAGNOSIS I: EXTRA LOADING

The NETs estimated for BA1 from detector time streams and the CMB calibration are much higher than the proposed numbers. The achieved detector parameters are not aligned with the assumptions in Table 5.3. For 30 GHz, instead of a 30% optical efficiency, we have only achieved around 20%, with a slightly narrower bandpass than the assumed 27%. The actual Gs are also higher than the design targets, as shown in Section 6.4. With the measured detector parameters, according to Figure 5.12, the NETs for 30 and 40 bands are degraded to about 450 and 350 $\mu\mathrm{K}\sqrt{s}$ respectively, still not enough to explain the NET derived from the data.

During the first two years of operation, we found two additional problems that might be the causes of the degraded performance. One of them was that the detector loading Q was much higher than expected. The extra part of the loading was found to be out-of-band, most likely as a blue leak, downgrading the performance by boosting the photon noise. The second issue was related to the nonuniformity of the 6-inch tile as mentioned in Section 6.4. The TESs with high R_n turn out to have strong magnetic susceptibility at low-resistance transition, pushing us to bias them at high R. The high operating resistance degrades the detector's readout noise and contributes to the high NET.

In this chapter, we present the diagnosing process for the extra-loading. An additional filter was added in 2022 to eliminate the high-frequency leak, and the improvement from the upgrade is shown here. We talk about the magnetic pickup in the next chapter.

7.1 Direct stimulation of bolometers

As described in Chapter 5, the desired optical signal is coupled to the TES through the antenna-filter path, with a well-understood spectrum and beam. However, a certain amount of optical power is coupled to the bolometer island directly without passing through the designed path.

The plausible cause of the direct coupling had been explored back in BICEP2 era. The isolated feature of the island causes it to be held at a higher potential when radiation exists. The voltage difference between the TES island and the surrounding ground

can drive millimeter-wave currents through the gold meander resistor, resulting in direct stimulation of the detector. This effect had been observed in the early phase of BICEP2 development and minimized by adding more legs in the group plane layer (P. A. R. Ade, R. W. Aikin, et al., 2015). For 30 and 40 GHz, because the length of legs is much longer than the previous design, the problem is expected to be worse from EM simulations.

In Section 6.2, we showed the dark coupling in the optical efficiency measurement. With a beam-filling, Rayleigh-Jeans source, the dark response accounts for $\sim 27\%$ of the total loading at 30 GHz and $\sim 10\%$ at 40 GHz. As a comparison, the dark response in BICEP2 before and after the improvement was only $3-4\%$ and 0.5%.

The measured beam at the near-field of a dark pixel is shown in Figure 7.1. We measured a similar beam response from all light and dark pixels with a high-pass "thick-grill" filter cut off at 60 GHz, suggesting that the dark response is likely to be at higher frequencies than the desired bandpass, a.k.a. a blue-leak. The beam of the dark response also suggests a large angular response. This matches the expected radiation pattern of the small TES island.

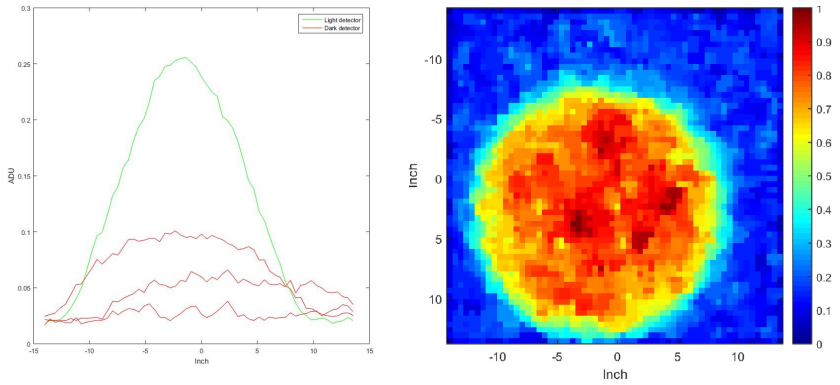

Figure 7.1: Near field beam map results of detectors in 2020 season. (Left) X cross-section through the peak of a light detector overlaid with a few darks. (Right) A beam map of a dark pixel, peak normalized. Plots by Ahmed Soliman.

The FTS measurement failed to capture the spectral feature of the dark coupling because the FTS is not a beam-filling device, and the beam of the dark response is likely to be not collimated at the receiver aperture. We also suspect that the frequency response of the dark coupling is broad-band, which makes it harder to be spotted in the FTS spectrum. Instead, we performed tests with different combinations of filter stacks to pin down the frequency range. The results show that the out-of-band power is from above 100 GHz, with a large portion between 120 and 150 GHz.

Figure 7.2: Photos of the low-pass mesh filter by Cardiff in BA1. (Left) Tiled-design 1.6 cm^{-1} filters in 2020 and 2021. Each filter tile covered two detector modules. (Right) New configuration in 2022 with a 1.6 cm^{-1} filter and a 4 cm^{-1} filter stacked together. Both are the same size as the FPU.

The dark stimulation was first noticed in lab tests before the initial deployment of BA1. In the first deployment at the end of 2019, six tiles of 1.6 cm^{-1} low-pass metal-mesh filter (Peter A. R. Ade et al., 2006) (Tucker and Peter A. R. Ade, 2006) were installed right above the detector modules at the 300 mK stage, as shown in the left panel of Figure 7.2. The filters should have a cut-off at 48 GHz and block all the photons above. However, the dark coupling still presented with the filter installed. We suspected that the tiled design made the scattered term of the filter larger than expected, leaving the high-frequency photons a path to reach the detector. It has also been proved that the 1.6 cm^{-1} filter's transmission opens back up above 140 GHz. In 2022, Cardiff provided the single-piece mesh filter which matches the size of our FPU. We also added another 4 cm^{-1} metal-mesh filter to the stack to eliminate any pickup from above 140 GHz. The new filter configuration is shown in the right panel of Figure 7.2.

The direct stimulation of the TES island added unwanted, out-of-band loading to the detectors in 2020 and 2021, elevated the photon noise, and degraded the detector performance, as shown in the following sections.

7.2 Sky and instrument loading

Assuming a plane-parallel atmosphere, the sky loading on a detector in power unit is

$$P_{sky} = P_{sky}^{zenith} \csc(\theta) \ . \tag{7.1}$$

θ is the elevation angle, and P_{sky}^{zenith} stands for the sky power when pointing at the zenith ($\theta = 90°$). For a detector pointing at an elevation θ, the in-transition electrical

power is

$$P_e(\theta) = P_{sat} - P_{inst} - P_{CMB} - P_{sky}^{zenith}\csc(\theta) \ . \tag{7.2}$$

The loading from CMB changes very slowly with $40 < \theta < 90$. As the lowest elevation accessible for the BA mount is 45°, we consider it as a constant in Eq. 7.2.

We can fit for P_{sky}^{zenith} with $P_e(\theta)$s measured at a series of θs. We rely on the integration in Section 5.6 for P_{CMB}. P_{inst} is the loading from instruments, which can also be estimated by the fit if the intrinsic saturation power P_{sat} is available.

We run the measurement at the South Pole after lifting the receiver to the mount. The forebaffle was installed, so the measured P_{inst} includes everything from the ambient temperature to 4 K. The schedule starts with the telescope's boresight pointing at 45° elevation angle and deck rotation angle at 0. We raise the telescope in elevation 5° a step to 100°, 10° pass zenith. Then we go back down from 100° to 45° with the same step size. At each elevation, the telescope is halted for taking load curves. The data taken while the mount moving in both directions provides a consistency check on the weather condition and tile temperature stability. Data with a large discrepancy between the two sets should be excluded from the final result, like the last deck 0 set in Figure 7.3. After taking load curves at all 24 elevations (up and down), we do a 45° boresight rotation and repeat all the steps above. We take data at eight different boresight angles from 0° to 315° and repeat the measurement at 0° (or 360°) at the end of the schedule for another consistency check across a longer time scale. The whole schedule takes about 6.5 hours to finish.

Figure 7.3 shows the data and the fitted curves of four detectors in 2021. The first panel of each sub-figure is a summarized plot for data taken at all deck angles. The rest panels are individual deck angles. Deck angle 0° was repeated at the end. The red and blue colors represent data taken when stepping elevation up and down, respectively. X axes are pointings corrected for individual detectors based on CMB maps (Crumrine, 2022). The dash curves are the fit using Eq.7.2. The P_c is the constant term in the equation, $P_c = P_{sat} - P_{inst} - P_{CMB}$. Numbers reported in the title of each panel are averaged between the upward and downward stepping data. Figure 7.3a and Figure 7.3c are light detectors, while Figure 7.3b and Figure 7.3d are dark detectors from the same run. The data shows clear detection of dark response to the atmosphere. We fitted the dark data with the same csc model and

got estimations of the dark sky response. Pointings of dark pixels are derived from a Zemax pointing model with the physical locations of the TES islands.

In the $Pe - \theta$ plots, we see a "fish hook barb" pattern shows up when the detector points past the zenith. Figure 7.3a deck 90 is a good example. One plausible cause is pointing error, and a pointing correction as large as 5 degrees is required for most BA1 detectors to improve the goodness of fit in the loading analysis, which is, however, much larger than the possible residual error after the CMB pointing analysis. We also noticed that the derived pointing correction tended to point toward the boresight direction, with a radial pattern in its amplitude across the FPU. This reminds us of the effect from a ghost buddy beam formed by reflection of the optics, which usually shows up at the other side of the boresight relative to the main beam (Yang, 2021). To include the effect of the buddy beam in our loading model, Eq. 7.2 becomes

$$P_e(\theta) = P_{sat} - P_{inst} - P_{CMB} - P_{sky}^{zenith}[\csc(\theta) + f\csc(\theta_b)] \ . \tag{7.3}$$

As it is hard to pin down both the pointing and the amplitude of the buddy beam from the loading analysis itself, we fixed θ_b at the mirrored location of the main beam relative to the boresight and fit for f only. Figure 7.4 (a) and (b) show P_e versus $\csc(\theta)$ with and without the correction applied. The "fish hook barb" also produced a fake deck angel dependence in all fit parameters if Eq. 7.2 is used. Figure 7.4 (c) shows an example of the sky power deck dependence in a 40 GHz tile. We carefully examined the fits and decided this deck dependence was not physical, but a result of the over-simplified model failing to describe the data especially when the "fish book barb" showed up. No deck dependence was detected after considering the buddy beam correction, as demonstrated in Figure 7.4 (d). Eq. 7.3 was used in the official loading analysis, and the residual deck angel dependence was ignored.

We saw hints of the buddy beam in Far Side Lobe (FSL) measurements in BA1. There is no published material for BA FSL, but the experiment is similar to that in BICEP3 (Yang, 2021). We originally suspected the buddy beam is related to the dark coupling. However, after the filter upgrade in 2022, the "fish hook barb" was preserved in the loading data. Thus, we defer further diagnosing to the future FSL campaign.

Figure 7.5 summarized the sky and instrument loading. The ratios between the dark and light response are much larger than the ratio between the dark and light $\mathrm{d}P/\mathrm{d}T$.

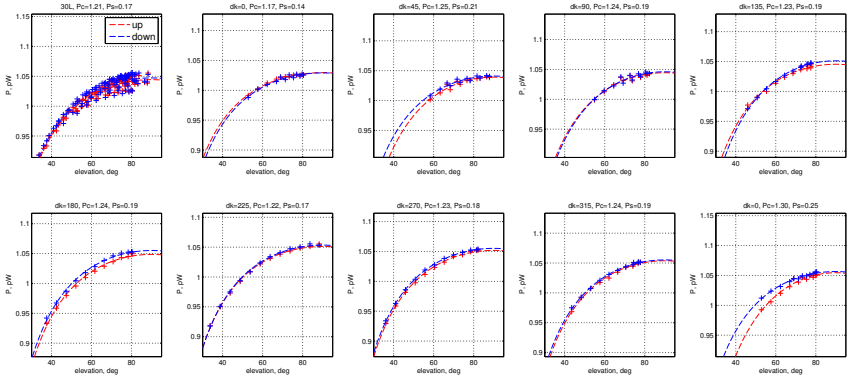

(a) A 30 GHz light detector.

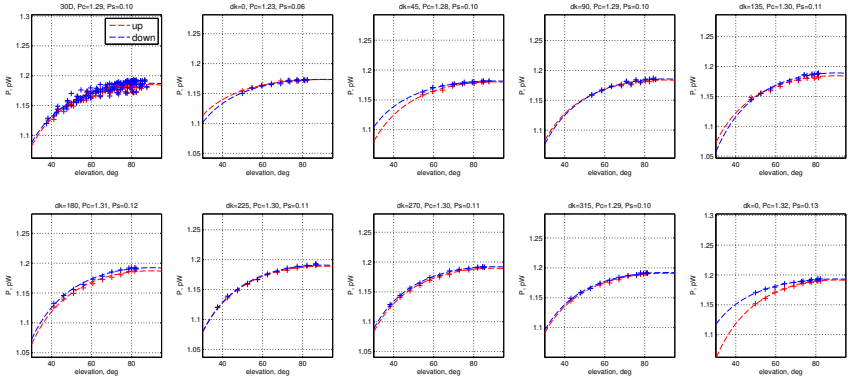

(b) A 30 GHz dark detector.

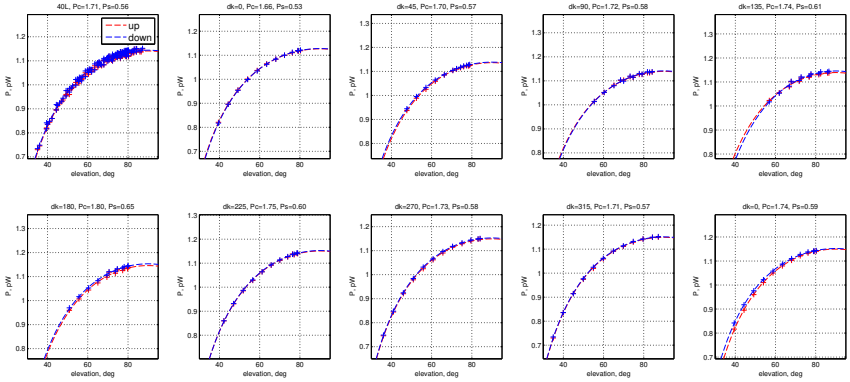

(c) A 40 GHz light detector.

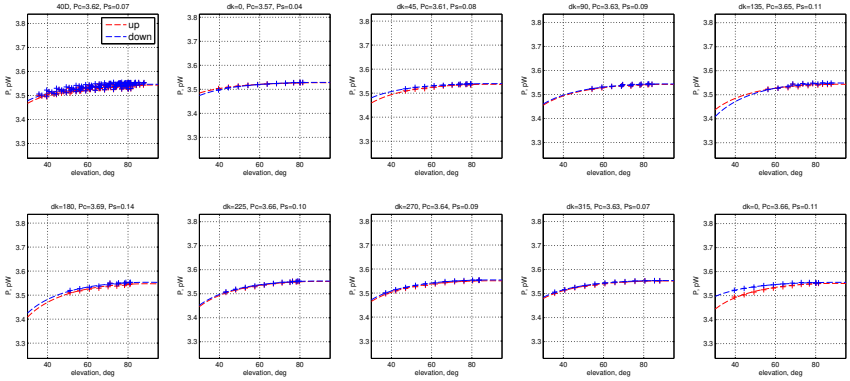

(d) A 40 GHz dark detector.

Figure 7.3: The P_e vs. elevation data and fit for detectors in BA1. Descriptions can be found in the text.

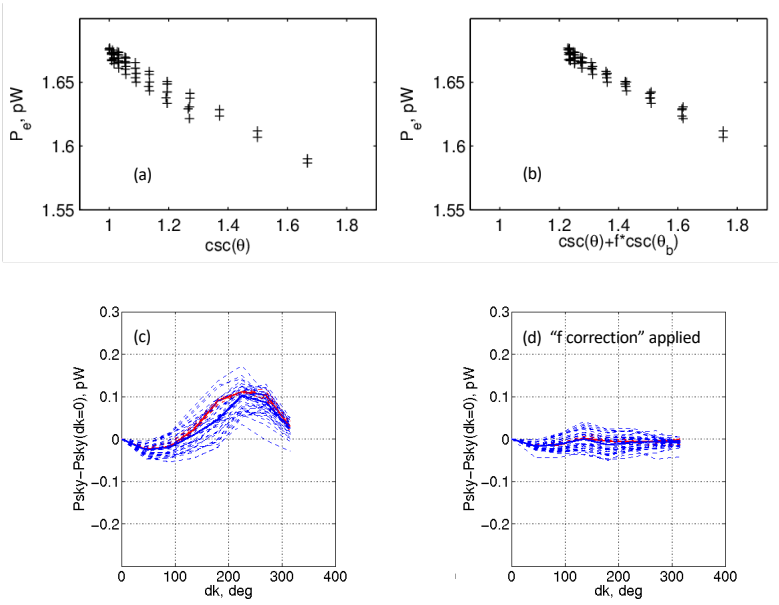

Figure 7.4: (a) P_e versus csc(θ) for one BA1 detector. (b) Same as (a) but with buddy beam correction as in Eq. 7.3. (c) Measured sky power at different deck angles for one tile in BA1. The deck 0 value is subtracted for showing the relative change between decks. Blue lines are for light pixels while red lines are for the darks in the same tile. Solid lines are the tile median. (d) Same as (c) but with buddy beam correction as in Eq. 7.3.

The plausible explanation is that the atmosphere is not a Rayleigh-Jeans source with a constant temperature. The out-of-band dark coupling could see a much hotter sky than the in-band response. We repeated the test in May 2022 after installing the new filters to eliminate the dark pickup. The results are shown in the second row of Figure 7.5. $P_{sky,dark}$ decreases while $P_{sky,light} = P_{sky} - P_{sky,dark}$ is about the same level as in 2021.

Instrument loading is tricky to estimate as it highly depends on the reliability of the dark run P_{sat} data. P_{inst}s in Figure 7.5 are scattered, and the distribution extends to negative values, which does not make sense. However, the relative change of the instrument loading between years can be measured much more reliably. The third column of Figure 7.5 shows the difference in P_{sky} and P_{inst} between the two years.

7.3 Forebaffle loading

"Forebaffle" is a cylinder tube mounted right above the receiver aperture to block stray lights reflected by the ground shield from getting into the receiver. The forebaffle inner surface is coated with HR-10. The whole piece is held at a few

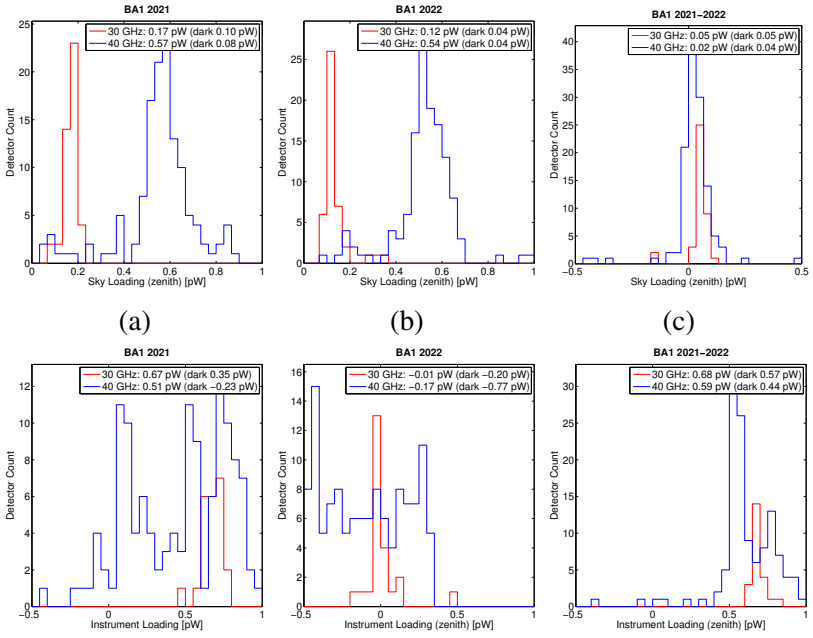

Figure 7.5: P_{sky}^{zenith} and P_{inst} histograms for data taken in 2021 and 2022. Blue is for light pixels and red is for the darks. Only common tiles between the two years are included.

degrees above the environmental temperature by the heat trace attached to the exterior of the cylinder. The diameter of the BA forebaffle is 1.01 m. Figure. 7.6 show photos of forebaffles after they are installed.

The coupling of the forebaffle to the receiver is only through a large-angle response. The extra loading added by the forebaffle is at about 1 K level in BICEP2 and 3 to 4 K in *Keck* receivers. Forebaffle loading is measured by taking detector load curves with and without it installed. I denote the measured power load in light and dark pixels as P_{FB} and $P_{FB,dark}$.

Table 7.1 shows the measured forebaffle loading in BA1 2020 and 2022 in both power and temperature unit. The conversion between power and temperature is done by dividing the power by the measured dP/dTs (Table 6.2). The measured P_{FB} in 2020 is 0.33 and 0.35 pW for 30 and 40 GHz, which is 11.9 and 6.0 K in the Rayleigh-Jeans unit. These are much higher than what was in *Keck*. The $P_{FB,dark}$s indicate that the dark response can account for a large portion of the total forebaffle loading. The ratio between P_{FB} and $P_{FB,dark}$ is much larger than the ratio of dark and light dP/dTs, because dP/dTs are measured with beam-filling sources, while the forebaffle only exists at large angle. After the filter configuration upgrade, we

retook the forebaffle measurement. Improvements can be seen in both bands.

We estimate the in-band forebaffle coupling through dark subtraction

$$P_{FB,light} = P_{FB} - P_{FB,dark} \tag{7.4}$$

$$T_{FB,light} = \frac{P_{FB,light}}{(\mathrm{d}P/\mathrm{d}T) - (\mathrm{d}P/\mathrm{d}T)_{dark}} \,. \tag{7.5}$$

This provides information on how large the forebaffle loading will be if there is no dark coupling. Using data taken in 2020, the $T_{FB,light}$ is 5 K for 30 GHz and 3 K for 40 GHz. In 2022, these numbers come to 4 K and 3 K.

Figure 7.6: A photo of the BA1 forebaffle.

year	band GHz	P_{FB} pW	$P_{FB,dark}$ pW	$P_{FB,light}$ pW	T_{FB} K	$T_{FB,dark}$ K	$T_{FB,light}$ K
2020	30	0.33	0.23	0.10	11.9	30.9	5.0
	40	0.35	0.19	0.16	6.0	31.6	3.0
2022	30	0.15	0.08	0.07	7.3	27.7	4.0
	40	0.22	0.07	0.15	4.1	34.8	3.0

Table 7.1: Measured forebaffle coupling in 2020 and 2022.

7.4 Summary and improvement in 2022

Table 7.2 summarizes our best guess on the break-down loading based on measurements. The Q_{CMB}s are calculated in the same way as in Section 5.6 with the

measured optical efficiency. The light and dark ratio of the CMB loading are scaled with the measured $\mathrm{d}P/\mathrm{d}T$s, assuming a constant atmosphere transmission. In reality, the transmission could change at the dark pickup frequency, but we think this scaling should be good enough for the first order. The atmosphere loadings are taken from Figure 7.5. We divide all the zenith loading numbers by a $\sin(55°)$ to account for the elevation pointing in CMB observations. Instrument loadings are from combination of information in Section 7.2 and 7.3 in a logical way. We assume that the dark loading from cold optics is negligible in 2022. The total instrument loading in 2022 is the sum of cold optics loading from the integration in Section 5.6 and the measured forebaffle loading. We get the 2021 instrument loading by adding on the measured difference between the two years.

Finally, we get total loading for the two bands and sub-total for the dark pickup. The filter upgrade in 2022 helps a lot. The dark fraction comes down to ~10% for 40 GHz in 2022. While it's still a bit high in 30 GHz, about 25%, there is still a huge improvement compared to 2021. We expect improvement in NET and mapping speed from both bands, with 40 GHz getting close to the proposed performance.

year	2021		2022	
band	30	40	30	40
Q_{CMB}	0.05	0.10	0.04	0.09
$Q_{CMB,dark}$	0.01	0.01	0.00	0.00
Q_{atm}	0.21	0.70	0.15	0.66
$Q_{atm,dark}$	0.12	0.10	0.05	0.05
Q_{inst}	0.95	1.11	0.27	0.52
$Q_{inst,dark}$	0.65	0.51	0.08	0.07
Q_{tot}	1.20	1.90	0.45	1.27
$Q_{tot,dark}$	0.78	0.62	0.13	0.12

Table 7.2: The estimation of the actual optical loading in 2021 and 2022 for common tiles between the two years. All numbers are in pW unit.

Chapter 8

BA1 DIAGNOSIS II: MAGNETIC PICKUP

8.1 Magnetic shielding in BA1

The SQUIDs in our readout system are sensitive magnetometers and should be operated in a magnetic-quiet environment. The BA receiver has multiple layers of magnetic shielding to protect the SQUIDs from the earth's magnetic field during CMB observations, as shown in Figure 8.1. We have a high-μ shield mounted at the outer surface of the 50 K cylinder. The SSA modules on the 4 K stage have Niobium cases and 10 layers of high-μ Metglas 2714A wraps. The Niobium IC plate and the spittoon become superconducting during observation providing shielding for the modules. The SQUIDs are sealed in a superconducting Nb box composed of the module case and the Nb back-short, with an additional layer of high-μ sheet. The pickup in the SQUIDs was measured in the lab and monitored by the empty SQUID channels and proved to be very small in BA1. The residual pickup, if there is any, will be cleaned by the ground subtraction step in our analysis pipeline because the magnetic field is ground-fixed.

The detectors are harder to be protected from the magnetic field, as they must be able to access photons. Magnetic field's effect on transition temperature T_c has been observed in certain types of TESs (Vavagiakis et al., 2018) but has never been an issue of our TES bolometers in the past BK experiments.

8.2 Bias-dependent magnetic pickup in TES

We discovered the magnetic susceptibility in our TESs during the first on-mount test of the BA receiver. A 40 GHz module was installed inside the receiver in the "dark mode", with a Cu plate covering the tile to block photons. The intention of the Cu plate was to isolate the influence of mount movement from the optical signal. However, we observed a strong current response synchronized with the mount movement in all TESs, as shown in Figure 8.2. The data was taken while the mount was scanning within a 120° angular range in the azimuth direction. The blue line is the measured time stream, while the orange line is a fit for the first two Fourier modes. Compared to the white noise level of the data, the scan-synchronized signal is huge. In-lab Helmholtz coil test confirmed that this is magnetic pickup.

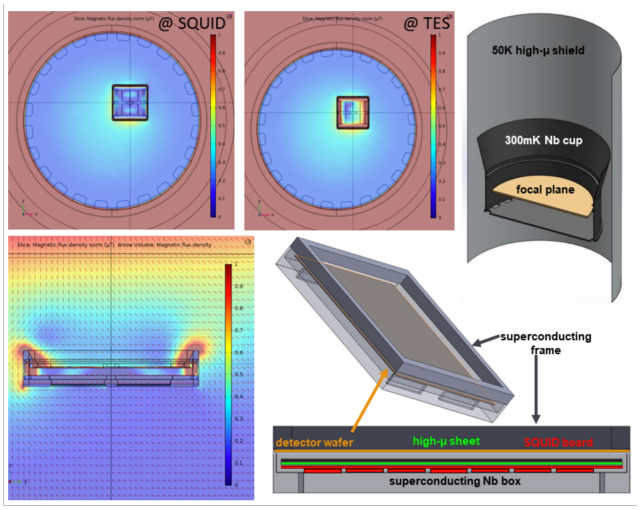

Figure 8.1: Magnetic shieldings in BA1. Plots are from (Schillaci et al., 2020) and Moncelsi et al., 2020.

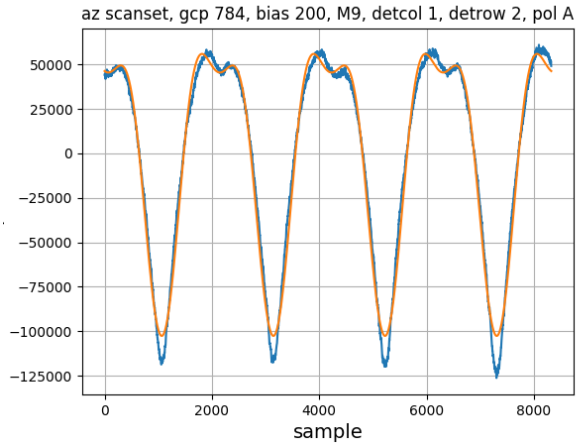

Figure 8.2: An example for the time-ordered response of a detector with magnetic susceptibility. The telescope did 4 times back-and-forth azimuth scans through a 120° angular range when this data was taken. The blue line is the detector time stream, which shows a slight nonlinear response to the mount movement. The orange line is a fit for the first two Fourier modes.

We set up Helmholtz coils for both BA1 and ShortKeck to perform magnetic tests. The coils in BA1 are mounted right outside the 300 K vacuum jacket, with 23 turns and an 800 mm diameter. We made two pairs of coils for BA1 as shown in the left plot of Figure 8.3, for both axial and transverse direction B-field. The axial coils were deployed to the South Pole with the receiver for on-mount magnetic testing. The ShortKeck coils are in the axial direction only, with 15 turns and an 800 mm diameter, as shown in the right plot of Figure 8.3. In both cases, the FPU is right at

the center of the two coils. The applied external B-field can be calculated as

$$B = \left(\frac{4}{5}\right)^{3/2} \frac{\mu_0 n I}{R} \,. \tag{8.1}$$

μ_0 is the permeability of free space. n is the number of turns. I is the coil current. R is the diameter of the coil. The B-field inside the cryostat is hard to figure out with the complexity of the multi-layer shielding. We connected the coil to a function generator to apply an oscillating B-field to the detector. The period was set to be long enough so the detector's response is "quasi-static".

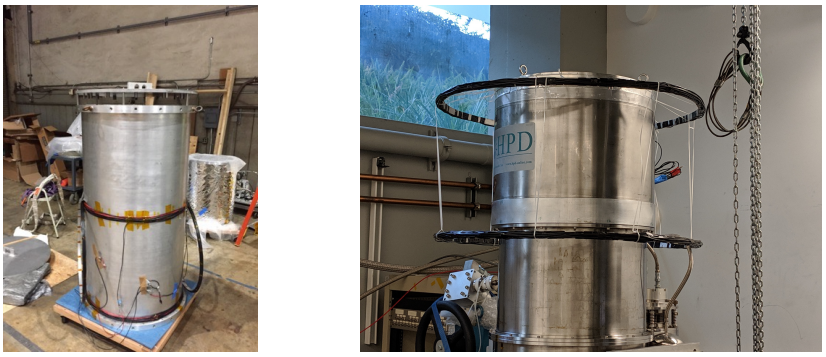

Figure 8.3: Coil setup in BA1 and ShortKeck.

For the on-mount coil test at Pole, we applied a 20 μT peak-to-peak sine wave B-field and measured current response at different detector biases. The amplitude of the response, as shown in Figure 8.4, has a strong dependence on the TES bias. The detector has no susceptibility to the B-field in superconducting or normal state. In transition, the pickup is strongest at low bias. More precisely, the pickup correlates with a non-flat part of the TES's P-R curve, as shown in the lower panel of Figure 8.4.

Non-flat P-R curve usually points to weak electrothermal feedback. Figure 8.5 shows the loop gain derived from the P-R curve with Eq. 5.13 together with the invert of the measure time constant $1/\tau \propto (\mathcal{L}+1)$. At low bias, where the P-R is not flat, the loop gain is low, and the detector is slow (large τ). Although a 50ms time constant is not terrible as our science band is $f \lesssim 2$Hz, it indicates some fundamental problem in our fabricated devices which changes their behavior in deep transition.

The non-flat P-R curve turns out to be caused by small cracks in the Ti TES layer. As shown in Figure 8.6, we cut the TES resistor with the Focused Ion Beam (FIB)

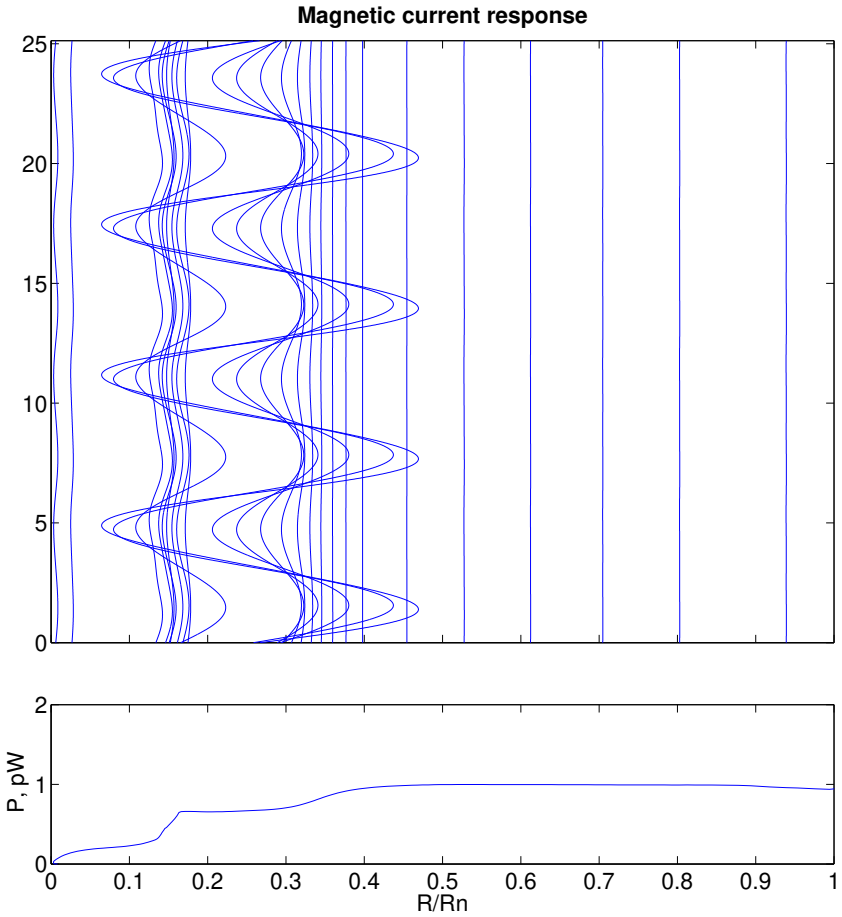

Figure 8.4: Current response to applied magnetic field versus detector bias. In the top panel, each curve is a detector time stream measured at a unique bias. The x location of the curve shows the R/R_n at which it was measured. The absolute x amplitudes of the curves are meaningless while the relative amplitude reflects the current responsivity to the field at a certain bias. The lower panel is the P-R curve of the same detector.

and examined the cross-section under the scanning electron microscope (SEM). We found small cracks in the Ti layer at "steps" where the underneath surface is uneven. The steps are there because we put down the Al TES first, and then bridge the Ti above, as shown in the top panel of Figure 8.10. The cracks are larger in the edge pixels than in the center ones. The non-flat shoulder in P-R curves also varies across the tile in a similar manner. We suspect that the cracks complicate the deep transition and make the TES behave more like a long Josephson Junction.

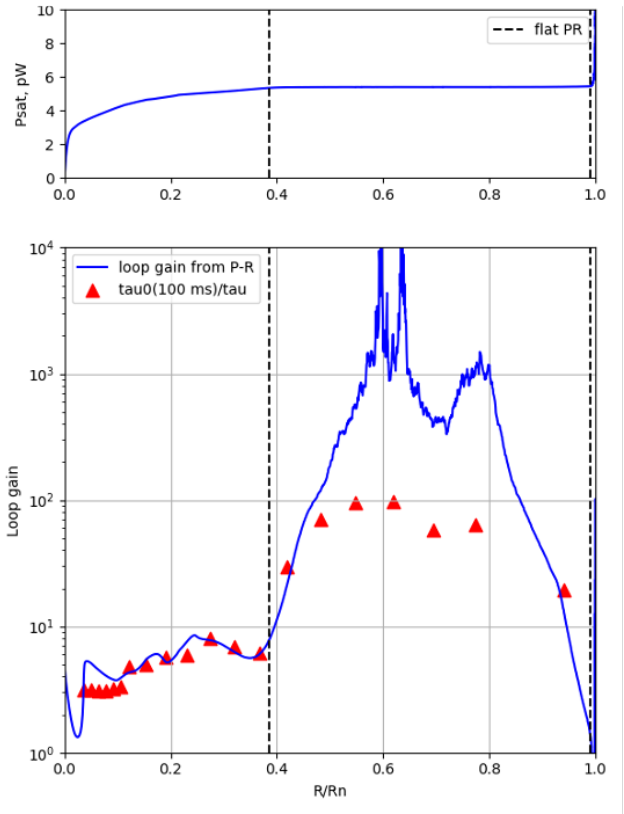

Figure 8.5: The P-R curve, loop gain, and measured time constant of one 40 GHz detector.

8.3 Comparison to 4-inch tiles in BICEP3

As we didn't change any step in TES fabrication for BA from the previous experiments, the observation above was a surprise. We were motivated to review some old 4-inch tiles to gain a better understanding of the problem.

In the lower row of Figure 8.7, we show loop gain versus resistance plots for one BA1 and two B3 tiles. Each row in a plot is a detector, and all detectors in one tile are sorted by their physical distance to the tile center. The bottom rows are TESs right around the tile center, while the top ones are those at edges/corners. Although the R_n gradient can be observed in all tiles, it is larger in the BA1 tile than in the others. As discussed in Section 8.2, low loop gain is related to the non-flat P-R curve. The low loop gain regions in the BA1 tile are much wider than in the B3 tiles, and even show up in the center pixels. The B3 tile in the center panel does have a relatively wide low loop gain region in the edge pixels. We checked the magnetic response of those detectors and show an example in the top panel. The black crosses are power responses to the azimuth mount movement with the aperture blocked by a blanking plate, which are indicators of magnetic susceptibility. We see that the

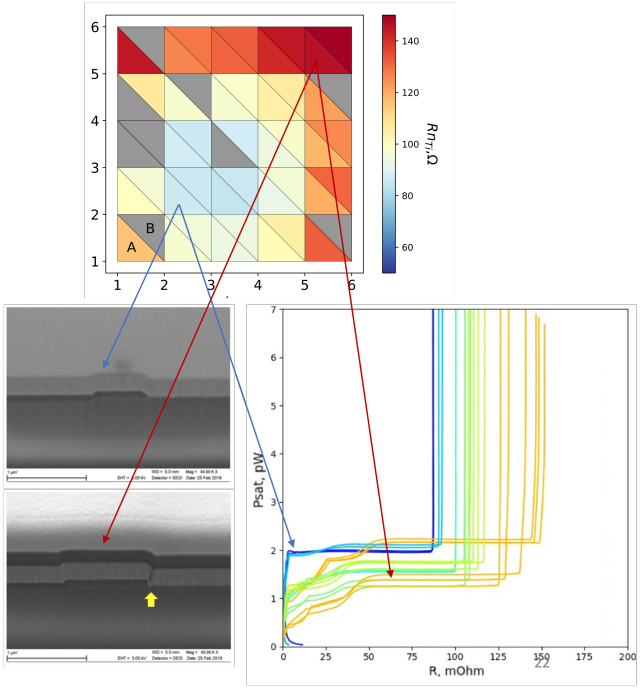

Figure 8.6: Top: R_n tile map. Lower left: SEM images of TES cross sections cut by FIB. Lower right: P-R curves color-coded by distances between TESs and the tile center. Blue means around the center. Yellow is for corner/edge pixels.

non-flat P-R, low loop gain, large time constant, and high magnetic susceptibility are all correlated with each other in the same way as in BA detectors.

We concluded that the low loopgain and high magnetic susceptibility problems also existed in the 4-inch B3 tiles. However, it is much worse in the 6-inch BA tiles. The worsening of the problem is likely to be caused by the Ti target becoming too small for 6-inch fabrication. In B3, because the averaged normal resistance was low, and the devices were well dominated by photon noise, there was no urge to push the bias low, thus the magnetic sensitive bias region was avoided. We had noticed scan-synchronized signals in a few detectors in B3 CMB data. They didn't raise much attention because they were only a very small fraction in the 2000+ detectors in B3. In BA1, the readout penalty does have a larger impact as the loading and photon noise are lower, so there is more interest to operate the detectors at a lower bias.

8.4 Detector bias

In each season, we perform NET vs. bias measurements to decide on detector biases during the first few months of the observation. The measurement is done by measuring the total responsivity and current noise at a series of bias points. The

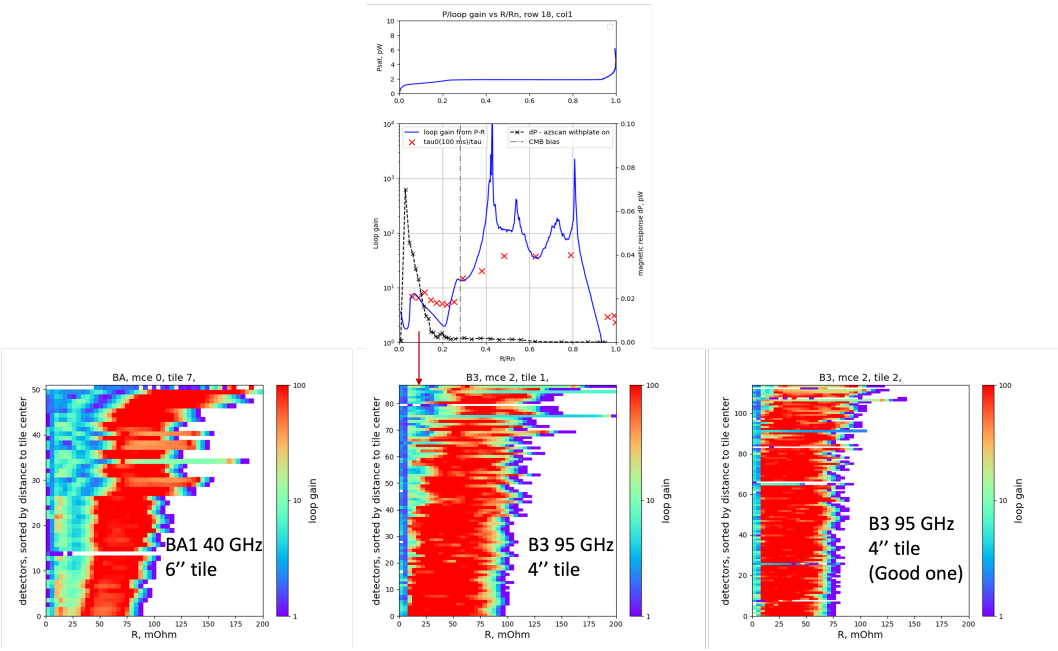

Figure 8.7: Comparison between BA and B3 tiles. Top: Load curve, loop gain, time constant, and magnetic response measured in one B3 detector. Bottom: Loop gain versus the resistance of one BA and two B3 tiles. Description see text.

responsivity is measured through elevation nods as described in Section 4.1. The current noise is converted into NET with the measured responsivity and a pre-set sky temperature. The measured NET will be artificially high if the actual sky temperature is lower than the assumption and artificially low if the actual sky is hot. However, the relative amplitude of the NETs between bias points is not affected by the real sky temperature. Because all detectors in the same MCE column need to share the same detector bias as constrained by the readout architecture, we calculate the weighted NET for each MCE column to find the optimized bias for the column. Figure 8.8 shows the column-weighted NET vs. bias curves for two MCE columns in one of the BA1 modules. The black stars mark out the bias points with minimized NETs.

For an ideal, photon noise-dominated TES, the NET should be close to a constant in transition. In BA1, however, the minimum NET points always appear around the low-bias edge of the NET bucket, just like the examples in Figure 8.8. We suspected that the magnetic susceptibility at low biases could have messed up the elevation nods. This raised concerns about impacts from the magnetic pickup on our gain calibration. Although we do not have a qualitative standard on how much gain-mismatch is acceptable, we want to keep it as small as possible, as it could

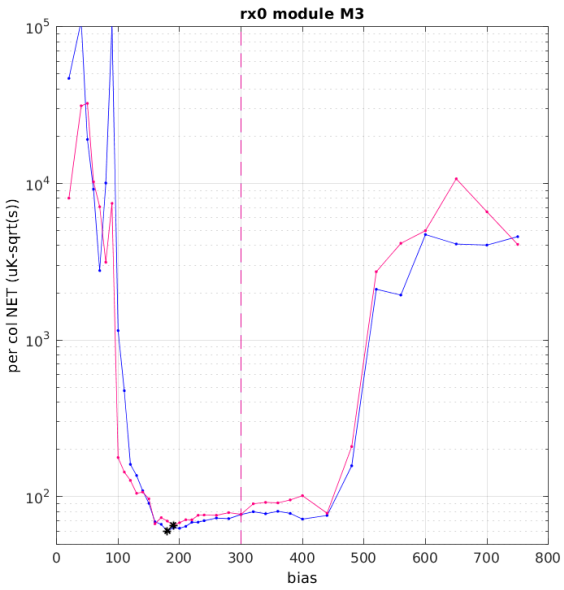

Figure 8.8: The column-weighted NET vs. bias curves of the two MCE columns in M3. The data was taken in Jan 2022. The actual sky temperature is likely to be hotter than the pre-set value in the code, resulting in an artificially low measured NET. The black stars are the bias points with minimized NETs, while the dash lines are the bias we ended up using. The final biases are the same for both columns in this very case.

potentially lead to large T-P leakage. The magnetic-sourced scan-synchronized response in wide azimuth direction scans is also potentially problematic, though it could in theory be handled by ground-fixed signal subtraction in data analysis.

We estimated the effect of the magnetic pickup in BA1 through a modified NET v.s. bias schedule. Elevation nods, azimuth scans, and static noise staring data were taken at a set of bias points. We repeated the same schedule with a blanking plate blocking the receiver window so that all responses were attributed to the magnetic pickup. We also took on mount Helmholtz coil measurements at the same set of bias points. Results of one BA1 column are shown in Figure 8.9. The blue curve is the column weighted NET. The black curve in Figure 8.9a is the ratio between elnod gain measured without and with the blanking plate mounted. The red curve in Figure 8.9b and the green curve in Figure 8.9c are the azimuth scan and coil response divided by the white noise level. Error bars in all three plots are for the variance of corresponding variables. The black vertical dash line marks the bias which gives the lowest weighted NET. At this minimized NET point, the elnod response is almost entirely magnetic, and the azimuth scan-synchronized response is enormous, more

than 100 times the white noise level. The solid black line shows the adjusted bias point which avoids most pickup effects.

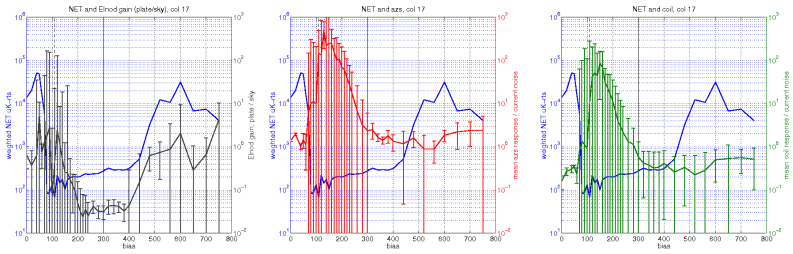

(a) Elevation nods (b) Azimuth scans (c) Coil

Figure 8.9: NET v.s. bias result for a column in BA1 overlaid with magnetic indicators. The kind of indicator is described in each sub-caption. The error bar show variance of the variable among all good detectors in the column.

The magnetic susceptibility pushed us to operate all BA1 detectors at a higher resistance, ~50 mΩ rather than the 30 mΩ assumed in proposal NET calculations. The high bias points provide low responsivity and increase the readout noise. For 40 GHz, biasing high worsens the bolometer NET by about 10%. The effect is larger at 30 GHz where the optical efficiency is low.

8.5 Inverted TES

"Inverted TES" is a modified TES fabrication process we developed to improve the reliability of the 6-inch process. Instead of putting down the Al detector first, we do the Ti layer first on the flat nitride surface. The Al is placed right next to the Ti, and the two are connected by some extra Al plugs. The bottom panel of Figure 8.10 shows the cross-section of an inverted TES. This modified process ensures the Ti TES is flat and minimizes the chance of cracking.

The inverted TES has been tested in BA2 150 GHz 6-inch wafers since the end of 2021. Figure 8.11 shows R_n v.s. distance to tile center for BA1 tiles, and the first 150 GHz tile using inverted TES. The latter has much lower R_ns and a much smaller gradient from center to edge. Load curves measured in the 150 GHz tile also show clean transitions across the whole wafer. The inverted TES is being used as the new standard TES fabrication process in BA.

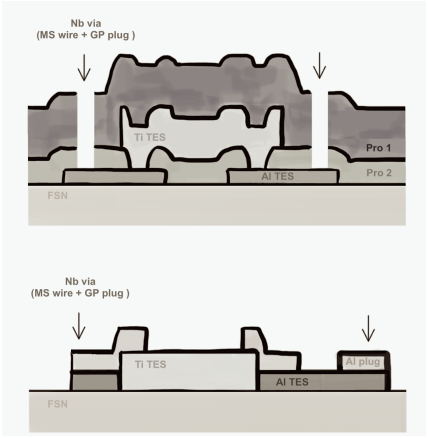

Figure 8.10: Cross sections of TES. The top panel shows the traditional TES fabrication in all BK experiments till BA1. The bottom one is the inverted TES.

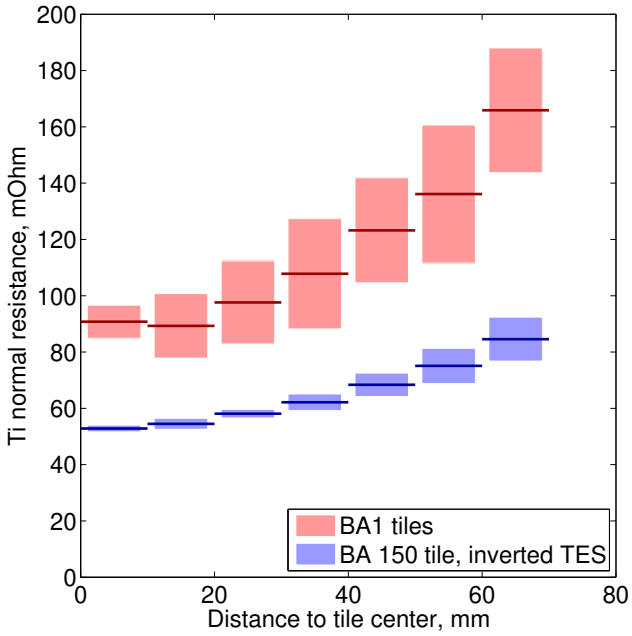

Figure 8.11: R_n versus distance to tile center. Lengths of the bars stand for RMS of the variable.

Chapter 9

CONCLUSIONS

BICEP Array (BA) is the latest generation of the BICEP/*Keck* (BK) degree-scale CMB polarization experiments. The final configuration of BA has four receivers spanning six frequency bands, aiming to achieve $\sigma(r) \lesssim 0.003$. The first BA receiver (BA1) was developed for observations at 30 and 40 GHz, targeting the synchrotron foreground (Chapter 4 and 5). BA1 was deployed at the end of 2019. The receiver has been fully characterized during its first few observing seasons (Chapter 6). However, the noise performance of the receiver after its initial deployment did not match the expectations in the proposal. We have gained great understandings of the problems with the new BA receiver and the 6-inch detector fabrication process with a series of receiver diagnosing studies (Chapter 7 and 8). We modified the filter configuration and improved the control on detector loading during the past 2021-2022 austral summer. A more reliable 6-inch fabrication process has been developed and will benefit the upcoming detector productions for the BICEP Array. The experience accumulated during the process will strongly benefit future experiments.

The BA1 data from its first year of operation has been processed through our standard analysis pipeline and has been reported in (Crumrine, 2022). The data at 30 and 40 GHz in 2020, despite its high noise level, significantly tightens the 95% CL upper limit of synchrotron amplitude from the $A^{l=80}_{sync,23\mathrm{GHz}} < 1.4\ \mu\mathrm{K}^2$ (P. A. R. Ade, Z. Ahmed, Amiri, et al., 2021) to $A^{l=80}_{sync,23\mathrm{GHz}} < 0.88\ \mu\mathrm{K}^2$. Noise levels and 40 GHz maps in 2020 are shown in Figure 9.1. The expected synchrotron level in the BK field from S-PASS data (Krachmalnicoff et al., 2018) is about 0.4 $\mu\mathrm{K}^2$ at 23 GHz $l = 80$. With the accumulation of data and the improvement in receiver performance, we expect to detect polarized synchrotron in our sky patch in the near future.

As a result of the very dim synchrotron level at the high galactic latitude, especially for the BK region, the low-frequency data's benefit on constraining r is delayed. The uncertainty on r will be increasingly depending on the delensing, as shown in the third panel of Figure 9.2. In our latest publication, we have already been in the regime where the sample variance of the lensing component dominates $\sigma(r)$ (P. A. R. Ade, Z. Ahmed, Amiri, et al., 2021). The benefit from the low-frequency data

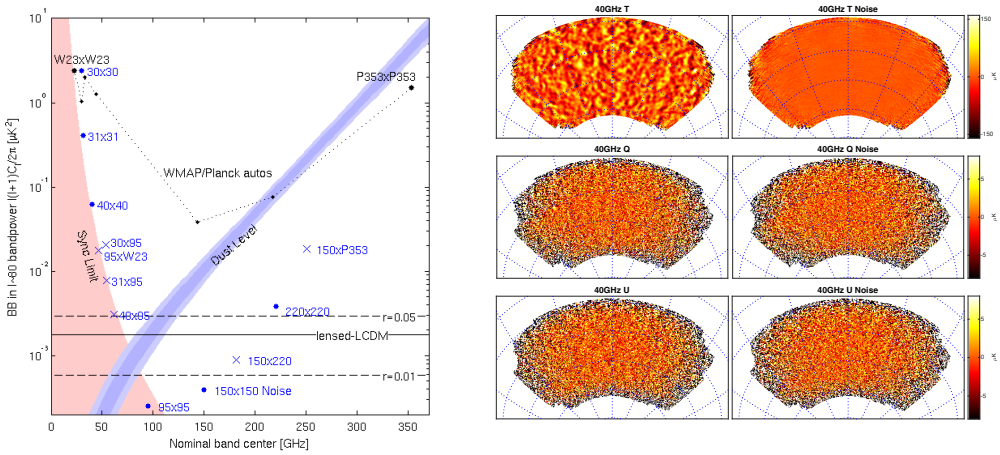

Figure 9.1: (Left) Noise uncertainties of the BICEP/*Keck* bands with respect to expectation values of BB signal in the l = 80 science bin. The expectation values and noise levels are the same as in Figure 2.1, besides that we added the noise levels of 30 and 40 GHz in 2020. 31 and 41 stand for the bands of the one dichroic tile in the same year. The addition of 2020 low frequency data improved the synchrotron constraint from $A^{l=80}_{sync,23\mathrm{GHz}} < 1.4\ \mu\mathrm{K}^2$ to $0.88\ \mu\mathrm{K}^2$. (Right) T,Q,U maps of 40 GHz in 2020. The second column shows the first noise realization. Plots made by Mike Crumrine. More details about BA2020 analysis see (Crumrine, 2022).

emerges as the delensing efforts become more successful or when more complicated foreground models are required. The availability of high-sensitivity multi-frequency polarization data can also benefit ISM studies, which may not be directly related to r but can enrich our understanding of the foregrounds and potentially inspire better foreground removal in the future CMB experiments. We demonstrated such studies in Chapter 3.

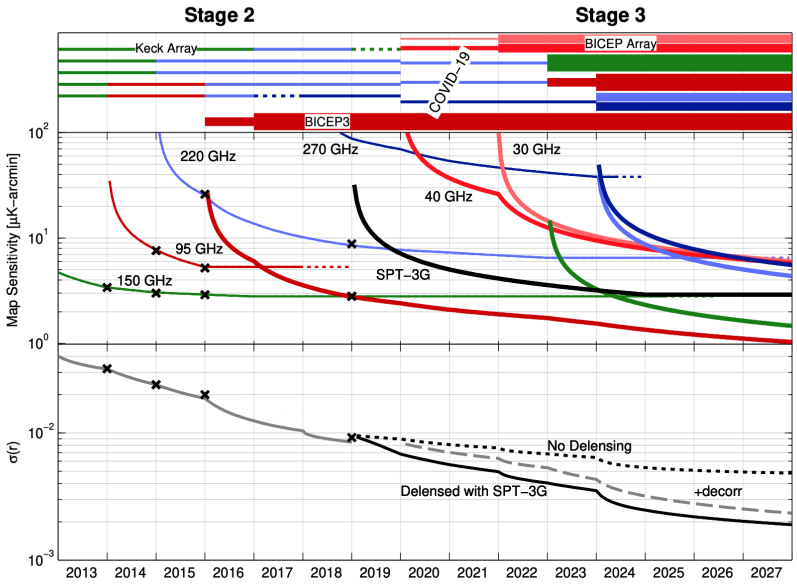

Figure 9.2: Projected sensitivity of the ongoing and planned BICEP/*Keck* observational program. The top panel represents the receiver throughput at the various frequencies by observing season. The middle panel shows map depth at each frequency as a function ofTassis time. The bottom panel is the sensitivity to r versus time. The lines are projected performance while the crosses are the achieved sensitivities reported in our publications.

BIBLIOGRAPHY

Ade, P. A. R., N. Aghanim, et al. (2016). "Planck 2015 results. XXV. Diffuse low-frequency Galactic foregrounds". In: *Astronomy Astrophysics* 594, A25. DOI: 10.1051/0004-6361/201526803.

Ade, P. A. R., Z. Ahmed, R. W. Aikin, et al. (2019). "BICEP2/Keck Array XI: Beam Characterization and Temperature-to-Polarization Leakage in the BK15 Data Set". In: *The Astrophysical Journal* 884.2, p. 114. DOI: 10.3847/1538-4357/ab391d.

Ade, P. A. R., Z. Ahmed, M. Amiri, et al. (2021). "Improved Constraints on Primordial Gravitational Waves using Planck , WMAP, and BICEP/ Keck Observations through the 2018 Observing Season". In: *Physical Review Letters* 127.15. DOI: 10.1103/physrevlett.127.151301.

Ade, P. A. R., R. W. Aikin, et al. (2015). "ANTENNA-COUPLED TES BOLOMETERS USED IN BICEP2,Keck Array, AND SPIDER". In: *The Astrophysical Journal* 812.2, p. 176. DOI: 10.1088/0004-637x/812/2/176.

Ade, Peter A. R. et al. (2006). "A review of metal mesh filters". In: *SPIE Proceedings*. DOI: 10.1117/12.673162.

Aghanim, N., Y. Akrami, M. I. R. Alves, et al. (2020). "Planck 2018 results. XII. Galactic astrophysics using polarized dust emission". In: *Astronomy Astrophysics* 641, A12. DOI: 10.1051/0004-6361/201833885.

Aghanim, N., Y. Akrami, M. Ashdown, et al. (2020). "Planck 2018 results. VI. Cosmological parameters". In: *Astronomy Astrophysics* 641, A6. DOI: 10.1051/0004-6361/201833910.

Akrami, Y. et al. (2020). "Planck 2018 results. X. Constraints on inflation". In: *Astronomy Astrophysics* 641, A10. DOI: 10.1051/0004-6361/201833887.

Alves, M. I. R. et al. (2018). "The Local Bubble: a magnetic veil to our Galaxy". In: 611, p. L5. DOI: 10.1051/0004-6361/201832637.

Andersson, B.-G., A. Lazarian, and J. E. Vaillancourt (2015). "Interstellar Dust Grain Alignment". In: 53, pp. 501–539. DOI: 10.1146/annurev-astro-082214-122414.

Belitsky, V. et al. (2006). "SUPERCONDUCTING MICROSTRIP LINE MODEL STUDIES AT MILLIMETRE AND SUB-MILLIMETRE WAVES". In: *International Journal of Infrared and Millimeter Waves* 27.6, pp. 809–834. DOI: 10.1007/s10762-006-9116-5.

Benoît, A. et al. (2004). "First detection of polarization of the submillimetre diffuse galactic dust emission by Archeops". In: 424, pp. 571–582. DOI: 10.1051/0004-6361:20040042.

BICEP/Keck Collaboration et al. (2018). "Constraints on Primordial Gravitational Waves Using Planck, WMAP, and New BICEP2/Keck Observations through the 2015 Season". In: 121.22, p. 221301. DOI: 10.1103/PhysRevLett.121.221301.

Chiang, Y.-K. and B. Ménard (2019). "Extragalactic Imprints in Galactic Dust Maps". In: 870, p. 120. DOI: 10.3847/1538-4357/aaf4f6.

Chuss, D. T. et al. (2019). "HAWC+/SOFIA Multiwavelength Polarimetric Observations of OMC-1". In: 872, p. 187. DOI: 10.3847/1538-4357/aafd37.

Clark, S. E. (2018). "A New Probe of Line-of-sight Magnetic Field Tangling". In: 857, p. L10. DOI: 10.3847/2041-8213/aabb54.

Clark, S. E. et al. (2015). "Neutral Hydrogen Structures Trace Dust Polarization Angle: Implications for Cosmic Microwave Background Foregrounds". In: *Physical Review Letters* 115.24, p. 241302. DOI: 10.1103/PhysRevLett.115.241302.

Clemens, D. P. et al. (2012). "The Galactic Plane Infrared Polarization Survey (GPIPS)". In: 200, p. 19. DOI: 10.1088/0067-0049/200/2/19.

Crumrine, Michael S. (2022). "BICEP Array: Searching for Signals of Inflation from the South Pole". PhD thesis. University of Minnesota.

Davis Jr., L. and J. L. Greenstein (1951). "The Polarization of Starlight by Aligned Dust Grains." In: 114, p. 206. DOI: 10.1086/145464.

Dodelson, Scott (2003a). "Coherent Phase Argument for Inflation". In: *AIP Conference Proceedings*. DOI: 10.1063/1.1627736.

– (2003b). *Modern Cosmology*. 1st ed. Academic Press.

Draine, B. T. and B. S. Hensley (2016). "Quantum Suppression of Alignment in Ultrasmall Grains: Microwave Emission from Spinning Dust will be Negligibly Polarized". In: 831, p. 59. DOI: 10.3847/0004-637X/831/1/59.

Dyck, H. M. and C. A. Beichman (1974). "Observations of Infrared Polarization in the Orion Nebula". In: 194, pp. 57–64. DOI: 10.1086/153223.

Falceta-Gonçalves, D., A. Lazarian, and G. Kowal (2008). "Studies of Regular and Random Magnetic Fields in the ISM: Statistics of Polarization Vectors and the Chandrasekhar-Fermi Technique". In: 679, pp. 537–551. DOI: 10.1086/587479.

Fissel, L. M. et al. (2016). "Balloon-Borne Submillimeter Polarimetry of the Vela C Molecular Cloud: Systematic Dependence of Polarization Fraction on Column Density and Local Polarization-Angle Dispersion". In: 824, p. 134. DOI: 10.3847/0004-637X/824/2/134.

Fixsen, D. J. (2009). "THE TEMPERATURE OF THE COSMIC MICROWAVE BACKGROUND". In: *The Astrophysical Journal* 707.2, pp. 916–920. DOI: 10.1088/0004-637x/707/2/916.

Fixsen, D. J. et al. (1996). "The Cosmic Microwave Background Spectrum from the FullCOBEFIRAS Data Set". In: *The Astrophysical Journal* 473.2, pp. 576–587. DOI: 10.1086/178173.

Foreman-Mackey, D. et al. (2013). "emcee: The MCMC Hammer". In: 125, p. 306. DOI: 10.1086/670067.

Gaia Collaboration et al. (2016). "The Gaia mission". In: 595, A1. DOI: 10.1051/0004-6361/201629272.

Galbraith, C.J. and G.M. Rebeiz (2008). "Higher Order Cochlea-Like Channelizing Filters". In: *IEEE Transactions on Microwave Theory and Techniques* 56.7, pp. 1675–1683. DOI: 10.1109/tmtt.2008.925574.

Galitzki, N. et al. (2014). "The Balloon-borne Large Aperture Submillimeter Telescope for Polarimetry-BLASTPol: performance and results from the 2012 Antarctic flight". In: *Ground-based and Airborne Telescopes V*. Vol. 9145. 91450R. DOI: 10.1117/12.2054759.

Gao, Jiansong et al. (2009). "Measurement of loss in superconducting microstrip at millimeter-wave frequencies". In: *AIP Conference Proceedings*. DOI: 10.1063/1.3292306.

Górski, K. M. et al. (2005). "HEALPix: A Framework for High-Resolution Discretization and Fast Analysis of Data Distributed on the Sphere". In: 622, pp. 759–771. DOI: 10.1086/427976. eprint: astro-ph/0409513.

Grayson, James A. (2016). "The BICEP3 Millimeter-Wave Polarimeter: Measuring the Cosmic Microwave Background from the South Pole". PhD thesis. Stanford University.

Greenberg, J. M. (1968). "Interstellar Grains". In: *Nebulae and Interstellar Matter*. Ed. by B. M. Middlehurst and L. H. Aller. the University of Chicago Press, p. 221.

Hall, J. S. (1949). "Observations of the Polarized Light from Stars". In: *Science* 109, pp. 166–167. DOI: 10.1126/science.109.2825.166.

Hammerstad, E. and O. Jensen (1980). "Accurate Models for Microstrip Computer-Aided Design". In: *MTT-S International Microwave Symposium Digest*. DOI: 10.1109/mwsym.1980.1124303.

Hanany, S. et al. (2019). "PICO: Probe of Inflation and Cosmic Origins". In: *arXiv e-prints*. arXiv: 1902.10541.

Harrison, E. R. (1970). "Fluctuations at the Threshold of Classical Cosmology". In: *Physical Review D* 1.10, pp. 2726–2730. DOI: 10.1103/physrevd.1.2726.

Herman, D. C. (2019). "Thermal Dust Emission in the Microwave Frequency Range". Master's Thesis. University of Oslo.

HI4PI Collaboration et al. (2016). "HI4PI: A full-sky H I survey based on EBHIS and GASS". In: 594, A116. DOI: 10.1051/0004-6361/201629178.

Hildebrand, R. H. et al. (2009). "Dispersion of Magnetic Fields in Molecular Clouds. I". In: 696, pp. 567–573. DOI: 10.1088/0004-637X/696/1/567.

Hiltner, W. A. (1949). "Polarization of Light from Distant Stars by Interstellar Medium". In: *Science* 109, p. 165. DOI: 10.1126/science.109.2825.165.

– (1951). "Polarization of Stellar Radiation. III. The Polarization of 841 Stars." In: 114, p. 241. DOI: 10.1086/145465.

Houde, M. et al. (2009). "Dispersion of Magnetic Fields in Molecular Clouds. II." In: 706, pp. 1504–1516. DOI: 10.1088/0004-637X/706/2/1504.

Hu, Wayne and Scott Dodelson (2002). "Cosmic Microwave Background Anisotropies". In: *Annual Review of Astronomy and Astrophysics* 40.1, pp. 171–216. DOI: 10.1146/annurev.astro.40.060401.093926.

Hubble, Edwin (1929). "A relation between distance and radial velocity among extra-galactic nebulae". In: *Proceedings of the National Academy of Sciences* 15.3, pp. 168–173. DOI: 10.1073/pnas.15.3.168.

Hui, Howard (2018). "Measuring the Polarization of the Cosmic Microwave Background with BICEP3". PhD thesis. California Institute of Technology.

Hui, Howard et al. (2018). "BICEP Array: a multi-frequency degree-scale CMB polarimeter". In: *Millimeter, Submillimeter, and Far-Infrared Detectors and Instrumentation for Astronomy IX*. Vol. 10708. International Society for Optics and Photonics, p. 1070807.

Irwin, K.D. and G.C. Hilton (2005). "Transition-Edge Sensors". In: *Topics in Applied Physics*, pp. 63–150. DOI: 10.1007/10933596_3.

Jaffe, T. R. (2019). "Practical Modeling of Large-Scale Galactic Magnetic Fields: Status and Prospects". In: *Galaxies* 7, p. 52. DOI: 10.3390/galaxies7020052.

Kamionkowski, Marc, Arthur Kosowsky, and Albert Stebbins (1997). "Statistics of cosmic microwave background polarization". In: *Physical Review D* 55.12, pp. 7368–7388. DOI: 10.1103/physrevd.55.7368.

Kamionkowski, Marc and Ely D. Kovetz (2016). "The Quest for B Modes from Inflationary Gravitational Waves". In: *Annual Review of Astronomy and Astrophysics* 54.1, pp. 227–269. DOI: 10.1146/annurev-astro-081915-023433.

Kang, Jae Hwan (2020). "Measurement of the Polarization of the Cosmic Microwave Background with the BICEP3 and Keck Array Telescopes". PhD thesis. Stanford University.

Karkare, Kirit S. (2017). "Multifrequency Beam Systematics and Measurements of B-Mode Polarization with the BICEP/Keck Array Cosmic Microwave Background Experiments". PhD thesis. Harvard University.

Kerp, J. et al. (2011). "The Effelsberg Bonn H I Survey (EBHIS)". In: *Astronomische Nachrichten* 332.6, p. 637. DOI: 10.1002/asna.201011548.

King, P. K. et al. (2018). “Modelling dust polarization observations of molecular clouds through MHD simulations”. In: 474, pp. 5122–5142. DOI: 10.1093/mnras/stx3096.

Krachmalnicoff, N. et al. (2018). “S–PASS view of polarized Galactic synchrotron at 2.3 GHz as a contaminant to CMB observations”. In: *Astronomy Astrophysics* 618, A166. DOI: 10.1051/0004-6361/201832768.

Lane, Adair P (1998). “Submillimeter Transmission at South Pole”. In: *Astrophysics From Antarctica*. Vol. 141, pp. 289–295.

Lee, H. M. and B. T. Draine (1985). “Infrared extinction and polarization due to partially aligned spheroidal grains : models for the dust toward the BN object.” In: 290, pp. 211–228. DOI: 10.1086/162974.

Lenz, D., O. Doré, and G. Lagache (2019). “Large-scale CIB maps from Planck”. In: *arXiv e-prints*. arXiv: 1905.00426.

Lenz, D., B. S. Hensley, and O. Doré (2017). “A New, Large-scale Map of Interstellar Reddening Derived from H I Emission”. In: 846, p. 38. DOI: 10.3847/1538-4357/aa84af.

Lesurf, J.C.G (2019). *Millimetre-Wave Optics, Devices and Systems*. 1st ed. Routledge.

Lewis, Antony, Anthony Challinor, and Anthony Lasenby (2000). “Efficient Computation of Cosmic Microwave Background Anisotropies in Closed Friedmann-Robertson-Walker Models”. In: *The Astrophysical Journal* 538.2, pp. 473–476. DOI: 10.1086/309179.

Martin, D.H. and E. Puplett (1970). “Polarised interferometric spectrometry for the millimetre and submillimetre spectrum”. In: *Infrared Physics* 10.2, pp. 105–109. DOI: 10.1016/0020-0891(70)90006-0.

Mather, J. C. et al. (1994). “Measurement of the cosmic microwave background spectrum by the COBE FIRAS instrument”. In: *The Astrophysical Journal* 420, p. 439. DOI: 10.1086/173574.

McClure-Griffiths, N. M. et al. (2009). “Gass: The Parkes Galactic All-Sky Survey. I. Survey Description, Goals, and Initial Data Release”. In: 181, pp. 398–412. DOI: 10.1088/0067-0049/181/2/398.

Miville-Deschênes, M.-A. and G. Lagache (2005). “IRIS: A New Generation of IRAS Maps”. In: 157, pp. 302–323. DOI: 10.1086/427938.

Moncelsi, Lorenzo et al. (2020). “Receiver development for BICEP Array, a next-generation CMB polarimeter at the South Pole”. In: *Millimeter, Submillimeter, and Far-Infrared Detectors and Instrumentation for Astronomy X*. DOI: 10.1117/12.2561995.

Palladino, Steven M. (2021). "Constraining Primordial Gravitational Waves with BICEP/Keck Array Telescopes and Developing the BICEP Array Housekeeping System". PhD thesis. University of Cincinnati.

Panopoulou, G. V. et al. (2019). "Demonstration of Magnetic Field Tomography with Starlight Polarization toward a Diffuse Sightline of the ISM". In: 872, p. 56. DOI: 10.3847/1538-4357/aafdb2.

Peebles, P. J. E. and J. T. Yu (1970). "Primeval Adiabatic Perturbation in an Expanding Universe". In: *The Astrophysical Journal* 162, p. 815. DOI: 10.1086/150713.

Pelgrims, V. and J. F. Macıas-Pérez (2018). "Galactic Magnetic Field Reconstruction II. Constraints from polarized thermal dust sky as seen by *Planck*". In: *arXiv e-prints*. arXiv: 1807.10516.

Penzias, A. A. and R. W. Wilson (1965). "A Measurement of Excess Antenna Temperature at 4080 Mc/s." In: *The Astrophysical Journal* 142, p. 419. DOI: 10.1086/148307.

Planck Collaboration III (2018). "Planck 2018 results. III. High Frequency Instrument data processing and frequency maps". In: *arXiv e-prints*. arXiv: 1807.06207.

Planck Collaboration Int. XIX (2015). "Planck intermediate results. XIX. An overview of the polarized thermal emission from Galactic dust". In: 576, A104. DOI: 10.1051/0004-6361/201424082.

Planck Collaboration Int. XLII (2016). "Planck intermediate results. XLII. Large-scale Galactic magnetic fields". In: 596, A103. DOI: 10.1051/0004-6361/201528033.

Planck Collaboration Int. XLVIII (2016). "Planck intermediate results. XLVIII. Disentangling Galactic dust emission and cosmic infrared background anisotropies". In: 596, A109. DOI: 10.1051/0004-6361/201629022.

Planck Collaboration Int. XX (2015). "Planck intermediate results. XX. Comparison of polarized thermal emission from Galactic dust with simulations of MHD turbulence". In: 576, A105. DOI: 10.1051/0004-6361/201424086.

Planck Collaboration Int. XXI (2015). "Planck intermediate results. XXI. Comparison of polarized thermal emission from Galactic dust at 353 GHz with interstellar polarization in the visible". In: 576, A106. DOI: 10.1051/0004-6361/201424087.

Planck Collaboration IV (2018). "Planck 2018 results. IV. Diffuse component separation". In: *arXiv e-prints*. arXiv: 1807.06208.

Planck Collaboration X (2016). "Planck 2015 results. X. Diffuse component separation: Foreground maps". In: 594, A10. DOI: 10.1051/0004-6361/201525967.

Planck Collaboration XII (2018). "Planck 2018 results. XII. Galactic astrophysics using polarized dust emission". In: *ArXiv e-prints*. arXiv: 1807.06212.

Planck Collaboration XXX (2014). "Planck 2013 results. XXX. Cosmic infrared background measurements and implications for star formation". In: 571, A30. DOI: 10.1051/0004-6361/201322093.

Poidevin, F. et al. (2013). "Magnetic Field Components Analysis of the SCUPOL 850 μm Polarization Data Catalog". In: 777, p. 112. DOI: 10.1088/0004-637X/777/2/112.

Remazeilles, M., J. Delabrouille, and J.-F. Cardoso (2011). "Foreground component separation with generalized Internal Linear Combination". In: 418, pp. 467–476. DOI: 10.1111/j.1365-2966.2011.19497.x.

Schillaci, A. et al. (2020). "Design and Performance of the First BICEP Array Receiver". In: *Journal of Low Temperature Physics* 199.3-4, pp. 976–984. DOI: 10.1007/s10909-020-02394-6.

Skalidis, R. and V. Pelgrims (2019). "Local Bubble contribution to the 353-GHz dust polarized emission". In: *arXiv e-prints*. arXiv: 1908.08706.

Smoot, G. F. et al. (1992). "Structure in the COBE differential microwave radiometer first-year maps". In: *The Astrophysical Journal* 396, p. L1. DOI: 10.1086/186504.

Soliman, Ahmed et al. (2018). "Design and performance of wide-band corrugated walls for the BICEP Array detector modules at 30/40 GHz". In: *Millimeter, Submillimeter, and Far-Infrared Detectors and Instrumentation for Astronomy IX*. DOI: 10.1117/12.2312942.

Spitzer Jr., L. and J. W. Tukey (1951). "A Theory of Interstellar Polarization." In: 114, p. 187. DOI: 10.1086/145463.

St. Germaine, M. Tyler (2021). "Beam Systematics and Primordial Gravitational Wave Constraints from the BICEP/Keck Array CMB Experiments". PhD thesis. Harvard University.

Stein, W. (1966). "Infrared Radiation from Interstellar Grains". In: 144, p. 318. DOI: 10.1086/148606.

Stephens, I. W. et al. (2014). "Spatially resolved magnetic field structure in the disk of a T Tauri star". In: 514, pp. 597–599. DOI: 10.1038/nature13850.

Story, K. et al. (2012). "South Pole Telescope software systems: control, monitoring, and data acquisition". In: *SPIE Proceedings*. DOI: 10.1117/12.925808.

Sunyaev, R. A. (1978). "Fluctuations of the Microwave Background Radiation". In: *Symposium - International Astronomical Union* 79, pp. 393–404. DOI: 10.1017/s0074180900144857.

Tassis, Konstantinos et al. (2018). "PASIPHAE: A high-Galactic-latitude, high-accuracy optopolarimetric survey". In: *arXiv e-prints*. arXiv: 1810.05652.

Teply, Grant P. (2015). "Measurement of the Polarization of the Cosmic Microwave Background with the BICEP2 and Keck Array Telescopes". PhD thesis. California Institute of Technology.

Tolan, Jamie E. (2014). "Testing Inflationary Cosmology with BICEP2 and the Keck Array". PhD thesis. Stanford University.

Tucker, Carole E. and Peter A. R. Ade (2006). "Thermal filtering for large aperture cryogenic detector arrays". In: *SPIE Proceedings*. DOI: 10.1117/12.673159.

Vavagiakis, E. M. et al. (2018). "Magnetic Sensitivity of AlMn TESes and Shielding Considerations for Next-Generation CMB Surveys". In: *Journal of Low Temperature Physics* 193.3-4, pp. 288–297. DOI: 10.1007/s10909-018-1920-5.

Ward-Thompson, D. et al. (2017). "First Results from BISTRO: A SCUBA-2 Polarimeter Survey of the Gould Belt". In: 842, p. 66. DOI: 10.3847/1538-4357/aa70a0.

Westfold, K. C. (1959). "The Polarization of Synchrotron Radiation." In: *The Astrophysical Journal* 130, p. 241. DOI: 10.1086/146713.

Wheelock, S. L. et al. (1994). "IRAS sky survey atlas: Explanatory supplement". In: *NASA STI/Recon Technical Report N* 95.

Willmert, Justin (2019). "Constraining Inflationary B-Modes with the BICEP/Keck Array Telescopes". PhD thesis. University of Minnesota.

Wu, W.L. Kimmy (2015). "BICEP3 and CMB-S4: Current and Future CMB Polarization Experiments to Probe Fundamental Physics". PhD thesis. Stanford University.

Yang, Hung-I E. (2021). "Constraining Primordial Gravitational Waves and Characterizing B-Modes with the Keck Array and BICEP3 CMB Experiments". PhD thesis. Stanford University.

Zaldarriaga, Matias and Uroš Seljak (1997). "All-sky analysis of polarization in the microwave background". In: *Physical Review D* 55.4, pp. 1830–1840. DOI: 10.1103/physrevd.55.1830.

Zeldovich, Y. B. (1972). "A Hypothesis, Unifying the Structure and the Entropy of the Universe". In: *Monthly Notices of the Royal Astronomical Society* 160.1, 1P–3P. DOI: 10.1093/mnras/160.1.1p.

Zhang, G. et al. (2019). "Predicting CMB dust foreground using galactic 21 cm data". In: *arXiv e-prints*. arXiv: 1904.13265.